



UNIVERSIDAD NACIONAL AUTÓNOMA DE MÉXICO
PROGRAMA DE MAESTRÍA Y DOCTORADO EN INGENIERÍA
ELÉCTRICA – INSTRUMENTACIÓN

**MODELLING AND MEASUREMENT OF WAVEFRONT ABERRATION USING
ZERNIKE POLYNOMIALS FOR ITS APPLICATION TO THE FOCUSING OF
FEMTOSECOND LASER PULSES**

TESIS
QUE PARA OPTAR POR EL GRADO DE:
DOCTOR EN INGENIERÍA

PRESENTA:
M. EN. I. JOSÉ AGUSTÍN MORENO LARIOS

TUTORA PRINCIPAL
DRA. MARTHA ROSETE AGUILAR, ICAT - UNAM
COMITÉ TUTOR
DR. JESÚS GARDUÑO MEJÍA, ICAT - UNAM
DR. OSCAR GABRIEL RODRÍGUEZ HERRERA
PROGRAMA DE MAESTRÍA Y DOCTORADO EN INGENIERÍA
DR. OLEG V. KOLOKOLSTEV, ICAT - UNAM

CIUDAD UNIVERSITARIA, CDMX. ENERO 2021



Universidad Nacional
Autónoma de México

Dirección General de Bibliotecas de la UNAM

Biblioteca Central



UNAM – Dirección General de Bibliotecas
Tesis Digitales
Restricciones de uso

DERECHOS RESERVADOS ©
PROHIBIDA SU REPRODUCCIÓN TOTAL O PARCIAL

Todo el material contenido en esta tesis esta protegido por la Ley Federal del Derecho de Autor (LFDA) de los Estados Unidos Mexicanos (México).

El uso de imágenes, fragmentos de videos, y demás material que sea objeto de protección de los derechos de autor, será exclusivamente para fines educativos e informativos y deberá citar la fuente donde la obtuvo mencionando el autor o autores. Cualquier uso distinto como el lucro, reproducción, edición o modificación, será perseguido y sancionado por el respectivo titular de los Derechos de Autor.

JURADO ASIGNADO:

Presidente: Dr. Oleg V. Kolokoltsev Flatov
Secretario: Dr. Ramón Gutiérrez Castrejón
1 er. Vocal: Dra. Martha Rosete Aguilar
2 do. Vocal: Dr. Jesús Garduño Mejía
3 er. Vocal: Dr. Oscar G. Rodríguez Herrera

Lugar o lugares donde se realizó la tesis: Instituto de Ciencias Aplicadas y Tecnología,
UNAM

TUTOR DE TESIS:

Roseta Aguilar Martha

FIRMA

Acknowledgements

I dedicate this work to my parents, Agustín and Alejandra; to my sisters Alejandra and Sofia. It is been a long, long, path and without your love, council and wholehearted support, this endeavour would not be possible.

I also dedicate this work to Diana, my lovely wife. We are beginning a new chapter together and I'm proud to be at your side.

I thank the UNAM SPIE and OSA Student Chapters for creating a space where I could meet many friends and colleagues, and for the opportunity they granted me to grow and share with the student community.

I thank my advisor, Dr. Martha Rosete Aguilar, for the dedicated support and encouragement during these years full of interesting work; to Dr. Catalina García Ramírez and Dr. Ramiro Contreras Martínez for their aid in developing a spectral intensity filtering algorithm and to Alejandra Ramírez Ramírez for taking the experimental interferograms shown in this work.

I am grateful with the mental health professionals I've met during my PhD. They were pivotal on my overall health and allowed me to thrive.

I gratefully acknowledge the generous funding of *Dirección General de Asuntos del Personal Académico* (DGAPA) for projects IN107018, IN111818 and TA100219 and *Consejo Nacional de Ciencia y Tecnología* (CONACYT) for a grant that supported this work.

I also acknowledge *Instituto de Ciencias Aplicadas y Tecnología* and the *Programa de Maestría y Doctorado en Ingeniería de la Universidad Nacional Autónoma de México* for the opportunity they granted me to pursue my dreams.

Abstract

In this work we study the effect of optical aberrations on the spatial and temporal femtosecond pulse intensity distributions around the focal region for several optical systems without neglecting the pulse bandwidth and assuming dispersive effects like Group Velocity Dispersion and Propagation Time Difference are pre-compensated before propagation. We calculate the optical aberrations of a given system for each pulse constituent frequencies via finite raytracing, obtaining the Optical Path Difference surface and its Zernike polynomial coefficients, which can determine how the emerging wavefront deviates from an ideal spherical wavefront, and use this information to calculate the intensity distributions using the scalar diffraction theory. We measure the resulting intensity distributions to find the position of the shortest pulse duration and the smallest spot diameter along the focal region of a given system, and simulated two common experimental techniques for pulse characterization: the knife-edge test and the intensity autocorrelation for space and time measurement, respectively. We use two measurement criteria, the Full-Width Half-Maximum and the standard deviation, to compare the results obtained from the diffraction patterns and the indirect measurement techniques, finding that the standard deviation provides consistent results when applied to the theoretical intensity distributions and the experimental simulation results. We also implemented interferometric wavefront techniques based on Phase Shifting interferometry and developed a femtosecond pulse spectral intensity filtering algorithm using the research done in this work.

Resumen

En este trabajo estudiamos el efecto de las aberraciones ópticas en las distribuciones espaciales y temporales de intensidad de pulsos de femtosegundos alrededor de la región focal para varios sistemas ópticos, esto sin descartar el ancho de banda del pulso y asumiendo que efectos dispersivos como la Dispersión de Velocidad de Grupo y la Diferencia de Tiempo de Propagación son compensados antes de la propagación. Calculamos las aberraciones de un sistema óptico para cada frecuencia que conforma a un pulso de femtosegundos por medio de trazo de rayos finito, obteniendo la superficie de Diferencia de Camino Óptico y los coeficientes de los polinomios de Zernike correspondientes, los cuales indican en que medida se desvía el frente de onda emergente con respecto a un frente de onda esférico ideal, y usamos esta información para calcular las distribuciones de intensidad por medio de la teoría de difracción escalar. Medimos las distribuciones de intensidad resultantes para encontrar la posición en la región focal de un sistema óptico dado del spot más pequeño y la duración de pulso más corta, y simulamos dos técnicas experimentales para la caracterización de pulsos: la prueba de la navaja y la autocorrelación de intensidad para las mediciones en espacio y en tiempo, respectivamente. Usamos dos criterios de medición, la anchura a media altura y la desviación estándar, para comparar las mediciones obtenidas a partir de los patrones de difracción y las técnicas de medición indirectas, encontrando que la desviación estándar provee resultados consistentes cuando se utiliza para medir en las distribuciones de intensidad teóricas así como en los resultados de las simulaciones de experimentos. Además implementamos técnicas de medición interferométricas derivadas de la Interferometría por Corrimiento de Fase y desarrollamos un algoritmo para filtrar la intensidad espectral de un pulso de femtosegundos usando la investigación realizada en este trabajo.

Contents

Acknowledgements	i
Abstract	iii
Resumen	v
Contents	vii
List of Figures	xi
List of Tables	xv
Introduction	1
1 Finite raytracing	3
1.1 Quadric surfaces and the rectangular coordinate system	3
1.2 Ray representation in a three-dimensional rectangular space . . .	5
1.3 Intersection of a ray with an optical surface	5
1.3.1 Foot of the perpendicular from the origin to the line calculation	6
1.3.2 Search for the intersection of the ray and the optical surface	7
1.4 Ray refraction and reflection	9
1.5 Summary	12
2 Optical Path Difference	13
2.1 Wave Aberrations and Optical Path	13
2.2 Hopkins' <i>OPD</i> Equation and Tatian's <i>OPD</i> Caboose term . . .	14
2.3 Raytracing and Optical Path Difference calculations	17
2.4 Summary	18
3 Zernike Polynomials and the Wavefront Numerical Analysis	21
3.1 Infinite series expansion	21
3.2 Zernike polynomial indices and concise notation for discrete data	22
3.3 Least Squares fitting of Zernike polynomial coefficients	25
3.4 Aberration content calculation for an achromatic doublet	27

3.5	Summary	28
4	Phase Shifting Interferometry	29
4.1	PSI principle of operation	29
4.2	Sample interferograms	30
4.3	PSI linear least-squares fitting	31
4.4	SSPCA	32
4.4.1	Principal Component Analysis	33
4.4.2	Self-adaptive selection of interferogram subblocks and PCA (SSPCA)	34
4.5	PSI simulations	34
4.6	Experimental measurements	40
4.7	Summary	45
5	Impact of frequency-dependent spherical aberrations in the focusing of ultrashort pulses	47
5.1	Theory	48
5.1.1	Scalar diffraction theory	48
5.1.2	Ultrashort pulse modelling	50
5.1.3	Propagation of a femtosecond pulse through a non-dispersive system.	53
5.1.4	Intensity profile measurement	55
5.2	Simulations	56
5.2.1	Spatial and temporal intensity distributions for a 20 [fs] pulse	58
5.2.2	FWHM and standard deviation measurement comparison	62
5.2.3	Normalized standard deviation of the spatial intensity distributions around the paraxial focal point	63
5.2.4	Normalized standard deviation of the temporal intensity distributions around the paraxial focal point	65
5.2.5	Normalized intensity autocorrelation magnitude distributions around the paraxial focal point	66
5.3	Summary	67
6	Algorithm to filter the noise in the spectral intensity of ultrashort laser pulses	71
6.1	Measured spectrum properties and processing	72
6.1.1	Spectral intensity modelling and Signal-to-Noise Ratio	72
6.1.2	Spectrum expressions in function of wavelength and frequency	73
6.2	Digital Signal Processing	75
6.2.1	Savitzky-Golay smoothing	75
6.2.2	Baseline removal	76
6.2.3	Super-Gauss as truncating window	76
6.3	Proposed processing algorithm and testing	78
6.4	Summary	82

7 Conclusions	85
Bibliography	93
Articles & certificates	95

List of Figures

1.1	Sphere constructed with Equation (1.1). We use a right-handed rectangular coordinate and the vertex of the sphere coincides with the origin of the coordinate system.	4
1.2	Separation between two collinear orthogonal reference systems.	5
1.3	Moving from known point P to the point of the foot of the perpendicular from the origin P_{\perp} , seen from the y, z plane.	6
1.4	Graphic ray refraction process in two-dimensional presentation. Two concentric circles of radii proportional to refractive indices n_1 and n_2 . The blue line is the incident and refracted ray; the magenta line, the reflected ray.	10
2.1	An ideal optical system. Light emitted from a point source P propagates through the optical system and is focused at the image point P' [35].	14
2.2	Aberrated wavefront at the system exit pupil [35].	15
2.3	N-LAK22 / N-SF6 achromatic doublet. The diameter D is 12.0 [mm]; the curvatures C_1, C_2 and C_3 are 17.77, -16.46 and -136.80 [mm], respectively. The axial separation d_1 is 4.50 [mm] and the axial separation d_2 is 2.50 [mm]. Its design range is between 750 and 1550 [nm]. Its back focal length BFL for $\lambda = 810$ [nm] is 25.82 [mm].	17
3.1	Algorithm to generate Zernike circle polynomial indices. The generated data is stored in a structure, which is used to evaluate the corresponding circle polynomial when using the sequential numbering [41].	24
4.1	Test OPD surface for a unitary pupil of diameter $D = 2\rho$ with even 3rd order coma $Z_6(\rho, \theta) = -0.30[\lambda]$, 3rd order spherical aberration $Z_8(\rho, \theta) = 0.50[\lambda]$ and 5th order odd astigmatism $Z_{12}(\rho, \theta) = 1[\lambda]$	35

4.2	First four simulated interferogram frames for a normalized pupil of diameter $D = 2\rho$ using the OPD shown in Figure 4.1. The following parameters were used into Equation (4.14): $d = 10$ [μm], 10 interferograms, $\lambda = 632.8$ [nm], 128-by-128 pupil samples, $\delta(n) = \frac{2\pi dn}{\lambda}$, $I'(x, y) = 2 + \sin[20\pi(x + y)]$, $I''(x, y) = 1$, $\alpha(n) = \frac{2\pi n}{\lambda} * 50 \times 10^{-9}$, and $\beta(n) = \frac{-2\pi n}{\lambda} * 25 \times 10^{-9}$	36
4.3	Recovered and reconstructed OPD maps using the least-squares and SSPCA algorithms for a normalized pupil. Row 1) is the least-squares result; rows 2), 3), 4) depict the recovered OPD maps using the SSPCA algorithm with subblocks of size 16-by-16, 8-by-8 and 4-by-4. Column a) represents the recovered OPD map from every algorithm; column b) is the OPD surface generated by the fitted Zernike polynomial coefficients and column c) is the generated OPD surface when omitting piston, tilt and defocus terms.	39
4.4	First four frames from the measured sequences a) and b). The optical component analysed was a reflective spherical surface. We appreciate that there are fringes that seems to be independent of the phase-shift between snapshots.	42
4.5	Recovered and reconstructed OPD maps using the least-squares PSI algorithm on test a) and b). Row 1) is the recovered OPD surface from the PSI algorithm; row 2) is the reconstructed OPD surface from the fitted Zernike polynomial coefficients and row 3) is the reconstructed OPD surface when we omit the first four Zernike polynomial coefficients. We notice that there are visual differences between the OPD surfaces from both tests. The pupil dimensions where normalized against $\rho = 64$ [pixels].	43
4.6	Recovered and reconstructed OPD maps using the SSPCA PSI algorithm with a 8-by-8 subblock size on test a) and b). Row 1) is the recovered OPD surface from the PSI algorithm; row 2) is the reconstructed OPD surface from the fitted Zernike polynomial coefficients and row 3) is the reconstructed OPD surface when we omit the first four Zernike polynomial coefficients. We notice that the OPD maps on row 3) are quite similar, in agreement with Table 4.3. The pupil dimensions where normalized against $\rho = 64$ [pixels].	44
5.1	Monochromatic light propagation from the source plane of area A to the observation plane.	49
5.2	Spectral intensity $S(\omega)$ for a) 100 [fs], b) 50 [fs], and c) 5 [fs] pulses with a carrier wavelength $\lambda_0 = 810$ [nm].	52
5.3	Optical system coordinates used for the exit pupil and the observation plane located around the system focal point.	54

5.4	Fringe patterns calculated with Equation (5.25) for the systems presented in Table 5.1. a) concave spherical mirror; b) achromatic doublet; and c) single lens. All the systems have a numerical aperture of $NA=0.2$. The wavelength is $\lambda_0 = 810$ [nm] and a diameter $D = 12.0$ [mm]. The pupil was normalized against the system radius $\rho = D/2$	57
5.5	Normalized spatial and temporal intensity distributions with for several positions around the BFL of a concave mirror of $D = 12.0$ [mm] and $EFL = 30.0$ [mm] for a 20 [fs] pulse with a carrier wavelength $\lambda_0 = 810$ [nm].	59
5.6	Normalized spatial and temporal intensity distributions with for several positions around the BFL of an achromatic doublet $D = 12.0$ [mm] and $EFL = 30.0$ [mm], described in Table 5.1 for a 20 [fs] pulse with a carrier wavelength $\lambda_0 = 810$ [nm].	60
5.7	Normalized spatial and temporal intensity distributions with for several positions around the BFL of a double-convex lens with $D = 12.0$ [mm] and $EFL = 30.0$ [mm], described in Table 5.1 for a 20 [fs] pulse with a carrier wavelength $\lambda_0 = 810$ [nm].	61
5.8	Normalized full-width at half-maximum measurements of intensity distributions for the achromatic doublet in Table 5.1 for the complete-aberration case for different input pulse durations ranging from 5 to 100 [fs] (horizontal axis) in the range between [-500, 500] [μm] around the focal point $\Delta z = 0$ (vertical axis).	63
5.9	Normalized standard deviation measurements of intensity distributions for the achromatic doublet in Table 5.1 for the complete-aberration case for different input pulse durations ranging from 5 to 100 [fs] (horizontal axis) in the range between [-500, 500] [μm] around the focal point $\Delta z = 0$ (vertical axis).	64
5.10	Normalized standard deviation $\sigma_x = \sigma_{KE}$ of the spatial intensity distributions obtained from Equations (5.15) and (5.23) for $\tau_0 = [5, 100]$ [fs] around the paraxial focal point for the concave mirror, the achromatic doublet and the double-convex lens described in Table 5.1 for $\Theta(x_1, y_1, \omega) = 0$, $\Theta(x_1, y_1, \omega) = 2\pi ck_0/\omega_0 OPD(x_1, y_1, \omega_0)$ and $\Theta(x_1, y_1, \omega) = 2\pi ck/\omega OPD(x_1, y_1, \omega)$	65
5.11	Normalized standard deviation $\sigma_x = \sigma_{A^2}$ of the temporal intensity distributions obtained from Equations (5.16) and (5.24) for $\tau_0 = [5, 100]$ [fs] around the paraxial focal point for the concave mirror, the achromatic doublet and the double-convex lens described in Table 5.1 for $\Theta(x_1, y_1, \omega) = 0$, $\Theta(x_1, y_1, \omega) = 2\pi ck_0/\omega_0 OPD(x_1, y_1, \omega_0)$ and $\Theta(x_1, y_1, \omega) = 2\pi ck/\omega OPD(x_1, y_1, \omega)$	67

5.12	Normalized intensity autocorrelation $A^{(2)}(\tau)$ magnitudes in $\sigma_x = \sigma_{A^2}$ of the temporal intensity distributions obtained from Equations (5.16) and (5.24) for $\tau_0 = [5, 100]$ [fs] around the paraxial focal point for the concave mirror, the achromatic doublet and the double-convex lens described in Table 5.1 for $\Theta(x_1, y_1, \omega) = 0$, $\Theta(x_1, y_1, \omega) = 2\pi ck_0/\omega_0 OPD(x_1, y_1, \omega_0)$ and $\Theta(x_1, y_1, \omega) = 2\pi ck/\omega OPD(x_1, y_1, \omega)$	68
6.1	Spectral intensity of a BL Gaussian-modulated in frequency 20 [fs] pulse: a) represents $S_d(\lambda) + b(\lambda)$, b) is $S_m(\lambda) = S_d(\lambda) + b(\lambda) + \nu(\lambda)$ with a SNR = 20 [dB] and c) we show the converted spectrum to the frequency domain using Equation (6.5). Care must be taken when deciding the wavelength range for the spectrum conversion since an automatic FWHM measuring algorithm may provide an erroneous measurement.	75
6.2	Comparison of different combinations for P and σ for a given α	77
6.3	Spectra with offset and SNR = 20 [dB] and the recovered $I(t)$ for the discussed filtering techniques after the offset removal. Initial pulse durations are 100, 50, 20, 10 and 5 [fs]. Column a) shows the noisy spectra $S_m(\lambda)$; column b), the recovered $I(t)$ after removing the offset and applying a truncating window; column c), the recovered $I(t)$ after applying Algorithm 3. The spectral bandwidth is comprised from 365 to 2325 [nm].	83
6.4	Spectra with offset and SNR = 20 [dB] and the recovered $I(t)$ for the different filtering techniques, while restricting the spectral bandwidth to [365, 1300] [nm]. Initial pulse durations are 100, 50, 20, 10 and 5 [fs]. Column a) shows the noisy spectra $S_m(\lambda)$; column b), the recovered $I(t)$ after removing the offset and applying a truncating window; column c), the recovered $I(t)$ after applying Algorithm 3.	84

List of Tables

- 2.1 Raytracing and OPD calculations made with our in-house software. We use the z axis as the optical axis. (*) The OPD shown at the image plane was calculated with Equation (2.5). 18
- 2.2 Raytracing and *OPD* calculations obtained from Eikonal Optical Design Software. Eikonal uses the x axis as the optical axis. (*) Eikonal does report ΔW and W' but does not report δW as shown in Equations (2.4) and (2.5), so it must be calculated from the reported total which is truncated to the first three decimal places. 18
- 3.1 Zernike polynomials using the double and single index notation [35, 40, 41]. 25
- 3.2 Comparison of the renormalized aberration coefficients obtained from Eikonal and from our least-squares Zernike polynomial fit using the first 25 elements for the propagation of a collimated beam through an achromatic doublet . The obtained values were rounded to the second most-significant figure. All omitted coefficients in this table are considered to be zero. 27
- 3.3 Comparison of the renormalized aberration coefficients obtained from Eikonal and from our least-squares Zernike polynomial fit using the first 25 elements for the propagation of a beam incident on the achromatic doublet with a 2-degree angle with respect to the optical axis. The obtained values were rounded to the second most-significant figure. All omitted coefficients in this table are considered to be zero. 28
- 4.1 Zernike polynomial coefficients recovered from a series of simulated interferograms using different PSI algorithms. We notice that the SSPCA algorithm does not always retrieves the correct phase sign due the arbitrary assignment of sine and cosine properties to its principal components and that a subblock size that yields the least error must be determined. Please refer to Table 3.1 for aberration descriptions. 37

4.2	RMS error between our test OPD and the recovered and reconstructed OPD. the SSPCA algorithm can yield recovered OPD surfaces with an RMS error against the original surface less than 0.01 [λ] if we disregard the first four terms of the Zernike polynomial coefficients and select a suitable subblock size.	38
4.3	RMS error between the measured OPD surfaces of the two tests under different comparison conditions. When removing the piston, tilt and defocus terms from the fitted Zernike polynomial we find out that the SSPCA algorithm yields a variation of 0.0005 [λ] after analysing two sets of interferograms of the same test surface.	41
4.4	Experimental measurement Zernike coefficient comparison using the least-squares and the SSPCA approach with a 8-by-8 subblock size. When discarding the first four Zernike polynomial coefficients the largest differences found are in the 3rd order astigmatism $Z_4(\rho, \theta)$ and $Z_5(\rho, \theta)$ when using the least-squares PSI algorithm. This is not the case for the SSPCA algorithm. Please refer to Table 3.1 for aberration descriptions.	46
5.1	Optical system parameters used in the simulations. All components have a diameter $D = 12.0$ [mm] and effective focal length $EFL = 30.0$ [mm]	57
6.1	Comparison of obtained carrier wavelength and pulse duration from $S(\omega)$ when using Equation (6.5) or $S(\lambda) = S(\omega)$ from ideal pulses with a carrier wavelength $\lambda_0 = 810$ [nm]. For shorter ideal pulses, the conversion equation does preserve the carrier wavelength.	74
6.2	Comparison of obtained carrier wavelength and pulse duration from $S(\lambda)$ when using Equation (6.5) or $S(\lambda) = S(\omega)$ from ideal pulses with a carrier wavelength $\lambda_0 = 810$ [nm]. For shorter ideal pulses, the conversion equation does preserve the carrier wavelength.	74
6.3	Evaluation of Equation (6.8) for different values of P for $\sigma = 0.3$ and $\alpha = 4$	78
6.4	Average measurement results for 20 noisy 100 [fs] pulses spectra degraded with different SNR. τ_{TW} is the FWHM pulse duration measured from $I(t)$ obtained from removing the offset and applying a truncating window. τ_C is the FWHM pulse duration measured from $I(t)$ obtained from filtering the spectrum with Algorithm 3. This analysis considers that our bandwidth is comprised from 365 to 2325 [nm].	81

6.5	Average measurement results for 20 noisy pulses with offset and a SNR = 20 [dB]. The initial pulse durations τ_P are 100, 50, 20, 10 and 5 [fs]. τ_{TW} is the FWHM pulse duration measured from $I(t)$ obtained from removing the offset and applying a truncating window. τ_C is the FWHM pulse duration measured from $I(t)$ obtained from filtering the spectrum with Algorithm 3. This analysis considers that our bandwidth is comprised from 365 to 2325 [nm].	81
6.6	Average measurement results for 20 noisy pulses with offset and a SNR = 20 [dB]. The initial pulse durations τ_P are 100, 50, 20, 10 and 5 [fs]. τ_{TW} is the FWHM pulse duration measured from $I(t)$ obtained from removing the offset and applying a truncating window. τ_C is the FWHM pulse duration measured from $I(t)$ obtained from filtering the spectrum with Algorithm 3. This analysis considers that our bandwidth is comprised from 365 to 1300 [nm].	82

Introduction

Ultrashort laser pulses are electromagnetic wave packets that last several femtoseconds, 1×10^{-15} [s], and when focused, are able to deliver extreme peak power [1]. Some applications for ultrashort laser pulses are nonlinear microscopy [2–4], micromachining [5], medicine [6] and fundamental science [7–9].

The focusing of femtosecond pulses has been extensively studied theoretically and experimentally [10–22]. Techniques have been developed to measure the spatio-temporal coupling of ultrashort pulses around the focal region of optical systems [1, 23–29].

The effect of aberrations in the spatio-temporal coupling of femtosecond pulses around the focal plane has also been studied by calculating the aberration for the carrier-frequency and neglecting its variation with the frequencies of the pulse [13–15, 17–20]. In the present thesis, this approximation has been removed and the model takes into account that the aberration changes for different frequencies of the pulse.

A tool for the simulation of ultrashort pulse propagation through an optical system based on a combination of ray-tracing and wave optical propagation methods, including the variation of the aberration with pulse frequencies, was published by Fuchs, et.al. [16]. In the simulation in reference [16], the dispersive effects, namely: *Group Velocity Dispersion* [13, 14] and *Propagation Time Difference* [10–14] were also added to calculate the pulse front distortion in the focal region of different lenses.

The dispersion of the lens material is the major responsible for temporal pulse broadening, which limits the performance of the pulse once it is focused by an optical system. In a laboratory setting the group velocity can be pre-compensated by using a pulse compressor and the propagation time difference can be reduced by using achromatic optics. We neglect these two dispersion effects, while preserving the chromatic spherical aberration found in a given optical system in order to study the impact of the frequency-dependent aberration on the spatial and temporal intensity distributions around the focal plane.

To achieve this, on Chapter 1 we study the propagation of light through optical systems using geometrical optics without the paraxial approximation in order to evaluate the exact wavefront at the exit pupil of the optical system. We present the needed equations for ray translation and refraction or reflection on an optical surface. We follow Chapter 1 by discussing what are wave aberrations and a useful concept named *Optical Path Difference*, OPD, on Chapter 2, which

will allow us to determine the optical aberrations of a given system, while on Chapter 3 we study and apply Zernike polynomials to generate and measure the *Optical Path Difference* surfaces we obtain from the presented raytracing algorithms.

We present an application of Zernike polynomial fitting in Chapter 4 where we discuss how to retrieve the optical aberrations of a given system through the *Phase Shifting Interferometry* algorithm family. A Fizeau interferometer is being constructed at the *Laboratorio Universitario de Fabricación de Equipo Óptico - LUFABEO* (University Laboratory for Optical Equipment Fabrication) in the Institute of Applied Science and Technology at UNAM to obtain interferograms for measuring the shape of a surface. So, the algorithms described in this chapter will be tested with real interferograms.

On Chapter 5 we study femtosecond pulse propagation using a combination of geometrical optics and the scalar diffraction theory. We do not include the effects of *Group Velocity Dispersion* and *Propagation Time Difference* but consider frequency-dependent spherical aberration on the simulation in order to study its impact on the focusing of femtosecond pulses. We analyse three optical components: a concave spherical mirror, an achromatic doublet and a double-convex lens for different input pulse durations. We discuss two different criteria to measure the temporal and spatial intensity pulse profiles and the differences between approximating the aberration content to the aberration of the carrier or by taking into account that the aberration changes with the frequencies of the pulse.

And, lastly, on Chapter 6 we present an algorithm to filter noise in the spectral intensity for ultrashort laser pulses that requires little user intervention.

The research presented in this work resulted in two peer-reviewed publications [30, 31].

Chapter 1

Finite raytracing

We assume an optical system formed by rotationally symmetric surfaces. The optical system is described by the radius of curvature of the surfaces, the separation along the optical axis between each surface and the refractive indices of the media before and after each surface. Geometrical optics is used to describe the propagation of light through the optical system where the rays indicate the direction of the energy propagation. The paraxial geometrical theory, albeit useful to determinate how a given system forms an image, is only valid when the rays propagate close to the optical axis, and the angle of incidence is very small, so $\sin[\theta] \approx \theta$, where θ is the angle between a ray and the optical axis. In the paraxial approximation, the image of an object point is a point, i.e., all the rays that diverge from (or converge to) an object point will converge to (or diverge from) an image point. For rays that do not satisfy the paraxial approximation, the image will not be a point anymore, but a blur which will produce an aberrated image. [32]

To analyse light propagating through the system for non-paraxial rays and to assess the system aberration content, the optical designer traces the rays by using the Snell's law with no approximation of the sin function, i.e. it is an exact raytrace and it is called *finite raytracing*.

A finite raytracing requires two basic steps: ray transfer and ray refraction. Both processes are discussed in this chapter based on a raytracing method developed by J.L. Rayces [33].

1.1 Quadric surfaces and the rectangular coordinate system

Quadric surfaces are commonly used to describe the surfaces of lenses. Examples of such surfaces are spheres, paraboloids and ellipsoids, among others.

Any quadric can be expressed in a three-dimensional rectangular space by Equation (1.1):

1.1. QUADRIC SURFACES AND THE RECTANGULAR COORDINATE SYSTEM

$$Ax^2 + By^2 + Cz^2 + Dxy + Exz + Fyz + Gx + Hy + Iz + J = 0. \quad (1.1)$$

Although it is possible to describe a complete optical system using a single spatial reference system, the use of quadric surfaces is simplified greatly if each surface has its own local spatial reference system. For this work we use a right-handed rectangular coordinate system where the z axis is the optical axis, i. e., the reference axis for light propagation, and the origin of each coordinate system are coincident with the vertex of its associated quadric surface. A diagram is shown in Figure 1.1.

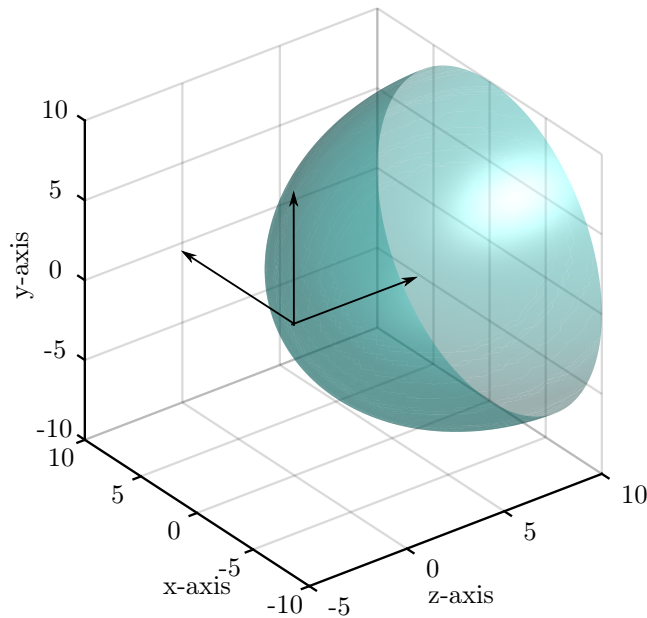


Figure 1.1: Sphere constructed with Equation (1.1). We use a right-handed rectangular coordinate and the vertex of the sphere coincides with the origin of the coordinate system.

Finally, suppose two orthogonal systems $(x_{i-1}, y_{i-1}, z_{i-1})$ and (x_i, y_i, z_i) as shown in Figure 1.2, that are separated by a distance d . These systems are related by Equations (1.2a), (1.2b) and (1.2c):

$$x_i = x_{i-1}, \quad (1.2a)$$

$$y_i = y_{i-1}, \quad (1.2b)$$

$$z_i = z_{i-1} + d. \quad (1.2c)$$

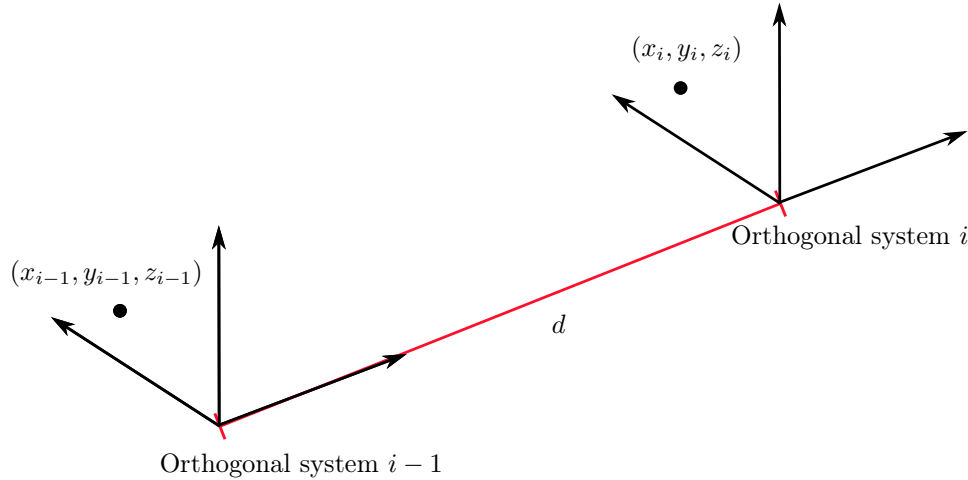


Figure 1.2: Separation between two collinear orthogonal reference systems.

1.2 Ray representation in a three-dimensional rectangular space

In Geometrical Optics, a ray represents the direction of the energy flow. A ray is generated by tracing a line perpendicular to the wavefront, which direction matches the direction of energy propagation in dielectric isotropic materials. The ray is described by a known point in the line and by its direction cosines, as shown in Equations (1.3a), (1.3b) and (1.3c):

$$x = X + t \cos \alpha, \quad (1.3a)$$

$$y = Y + t \cos \beta, \quad (1.3b)$$

$$z = Z + t \cos \gamma, \quad (1.3c)$$

where

x, y, z are the coordinates of any point in the line;

X, Y, Z are the coordinates of the known point in the line;

α, β, γ are the line direction angles, and

t is the distance between the known point to a new point.

1.3 Intersection of a ray with an optical surface

To model the ray propagation from one surface to another, it is needed to find the incidence point of the ray upon the surface. It is required to know a point

1.3. INTERSECTION OF A RAY WITH AN OPTICAL SURFACE

in the ray referred to the optical surface coordinate system and search the point where the ray and the surface intersect.

The foot of the perpendicular from the local reference system origin O to the ray is chosen as known point. Traditionally, the plane that contains point O and its perpendicular to the optical axis- z is used as the surface for ray intersection, however, if a ray makes 90 deg with the optical axis, this ray will not intersect this plane, thus, it will be undefined. This is an issue for wide angle field systems. The foot of the perpendicular prevents this situation.

1.3.1 Foot of the perpendicular from the origin to the line calculation

Given a known point P in the ray, of coordinates X, Y, Z . It is desired to locate the point P_{\perp} of the foot of the perpendicular from the origin O of the reference system to the ray, of coordinates $X_{\perp}, Y_{\perp}, Z_{\perp}$, as presented in Figure 1.3 [34].

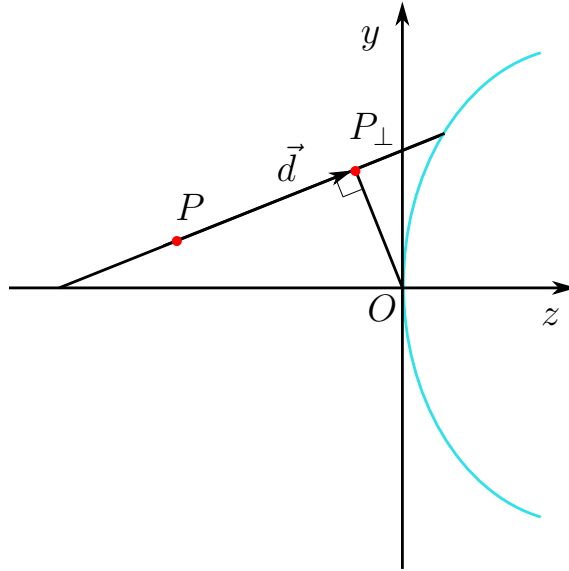


Figure 1.3: Moving from known point P to the point of the foot of the perpendicular from the origin P_{\perp} , seen from the y, z plane.

A vector $\vec{d} = \vec{P}_{\perp} - \vec{P}$ is defined, where

$$\vec{P}_{\perp} = \vec{P} + t'(\cos \alpha + \cos \beta + \cos \gamma) \quad (1.4)$$

Since the desired point is at the foot of the perpendicular, \vec{P}_{\perp} is perpendicular to \vec{d} , hence

$$\vec{P}_{\perp} \cdot \vec{d} = 0. \quad (1.5)$$

Substituting (1.4) in (1.5), and isolating t' :

$$t' = X \cos \alpha + Y \cos \beta + Z \cos \gamma. \quad (1.6)$$

The coordinates of the foot of the perpendicular from the origin to the ray are

$$X_{\perp} = X + t' \cos \alpha, \quad (1.7a)$$

$$Y_{\perp} = Y + t' \cos \beta, \quad (1.7b)$$

$$Z_{\perp} = Z + t' \cos \gamma; \quad (1.7c)$$

thus, the new ray parametric equations are

$$x = X_{\perp} + t \cos \alpha, \quad (1.8a)$$

$$y = Y_{\perp} + t \cos \beta, \quad (1.8b)$$

$$z = Z_{\perp} + t \cos \gamma. \quad (1.8c)$$

1.3.2 Search for the intersection of the ray and the optical surface

The optical surface is described by Equation (1.1). The quadric equation origin must be displaced in a way such that the surface vertex is coincident with origin of the reference system.

$$Ax^2 + By^2 + Cz^2 + Dxy + Exz + Fyz + Gx + Hy + Iz + J = 0. \quad (1.1)$$

An implicit equation that depends on t is obtained by substituting Equations (1.8a), (1.8b) and (1.8c) in Equation (1.1):

$$\Omega(t) = 0 \quad (1.9)$$

Spherical surface

If the optical surface to be described is an sphere of radius R , centered in $(0, 0, h)$ then the plane (x, y) is tangent to the sphere, the Equation (1.1) is

$$\frac{1}{R^2}x^2 + \frac{1}{R^2}y^2 + \frac{1}{R^2}z^2 + \frac{2h}{R^2}z + \frac{h^2}{R^2} - 1 = 0. \quad (1.10)$$

Equation (1.11) is obtained by substituting Equations (1.8a), (1.8b) and (1.8c) in Equation (1.10), and factorizing for t :

$$\begin{aligned} \frac{t^2}{R^2} [\cos^2 \alpha + \cos^2 \beta + \cos^2 \gamma] + \\ + \frac{2t}{R^2} [(1+h) \cos \alpha + \cos \beta + \cos \gamma] + \\ + \frac{1}{R^2} [x^2 + y^2 + z^2 + 2hz + h^2 - R^2], \end{aligned} \quad (1.11)$$

which is an equation in the form $at_i^2 + bt_i + c = 0$, where the smallest absolute value for t_i will be used to find the ray intersection point with the sphere.

Any quadric surface

To find the intersection point without knowing the optical surface equation beforehand a successive approximation method based on Newton-Raphson algorithm is used. The algorithm is described in the following steps:

- The coordinates are computed with Equations (1.8a), (1.8b) and (1.8c) using a initial t value. In this work the computation uses $t = 0$.
- Equations (1.9) and (1.12) are evaluated with the previously computed coordinates.

$$\begin{aligned} \frac{d\Omega}{dt} = \frac{dx}{dt} (2Ax + Dy + Ez + G) + \\ + \frac{dy}{dt} (2By + Dx + Fz + H) + \\ + \frac{dz}{dt} (2Cz + Ex + Fy + I). \end{aligned} \quad (1.12)$$

Differentiating Equations (1.8a), (1.8b) and (1.8c) with respect to t reveals that the derivatives are equal to the direction cosines of the incident ray.

- The new value for t is calculated by Equation (1.13):

$$t_i = t_{i-1} - \frac{\Omega}{\frac{d\Omega}{dt}}. \quad (1.13)$$

The iterative process stops when Ω is negligible or when a maximum number of iterations is done. If the maximum number of allowed iterations is reached without Ω being small enough, it is considered that the ray does not intersect the surface.

Evaluation of the line equation

Being t_i the solution obtained from the search methods previously described, the coordinates X_i, Y_i, Z_i that belong to the point where the ray intersects the

optical surface are:

$$X_i = X_{\perp} + t_i \cos \alpha, \quad (1.14a)$$

$$Y_i = Y_{\perp} + t_i \cos \beta, \quad (1.14b)$$

$$Z_i = Z_{\perp} + t_i \cos \gamma. \quad (1.14c)$$

1.4 Ray refraction and reflection

Once the point where the ray intersects the optical surface is found, it is required to calculate the normal line to the surface. The direction cosines of the normal line can be found by normalizing the partial derivatives of Equation (1.9):

$$\cos \lambda = \frac{1}{k} \frac{\partial \Omega}{\partial x}, \quad \cos \mu = \frac{1}{k} \frac{\partial \Omega}{\partial y}, \quad \cos \nu = \frac{1}{k} \frac{\partial \Omega}{\partial z}; \quad (1.15a)$$

$$k = \sqrt{\frac{\partial \Omega^2}{\partial x^2} + \frac{\partial \Omega^2}{\partial y^2} + \frac{\partial \Omega^2}{\partial z^2}} \quad (1.15b)$$

In order to refract or reflect a ray in a three-dimensional space, two concentric spheres of radii n_1 and n_2 are considered. The former corresponds to the object space and the latter to the image space. The coordinate system to be used is independent and parallel to the reference system used by the surface where the ray intersects.

A parallel line to the incident ray is traced from the center of the spheres, crossing the sphere of radius n_1 in a point N . From this point, a parallel line to the surface normal line is traced. This line crosses the sphere of radius n_2 at two points, \bar{N}_1 and \bar{N}_2 . The direction of the refracted ray is obtained by tracing a line from one either \bar{N}_1 or \bar{N}_2 , whichever is closer to N , to the local coordinate system origin. The process is displayed in Figure 1.4

Let $\cos \alpha, \cos \beta, \cos \gamma$ be the direction cosines of a line parallel to the incident ray. This line contains the origin of the coordinate reference system and intersects the sphere of radius n_1 at the point N of coordinates

$$\bar{X} = n_1 \cos \alpha, \quad (1.16a)$$

$$\bar{Y} = n_1 \cos \beta, \quad (1.16b)$$

$$\bar{Z} = n_1 \cos \gamma. \quad (1.16c)$$

From N a line normal to the surface is traced from the ray incidence point. The parametric line equations are:

$$x = X + \tau \cos \lambda, \quad (1.17a)$$

$$y = Y + \tau \cos \mu, \quad (1.17b)$$

$$z = Z + \tau \cos \nu, \quad (1.17c)$$

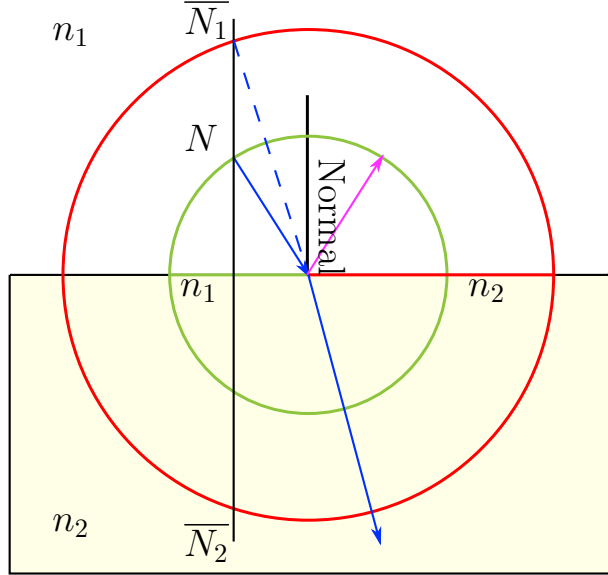


Figure 1.4: Graphic ray refraction process in two-dimensional presentation. Two concentric circles of radii proportional to refractive indices n_1 and n_2 . The blue line is the incident and refracted ray; the magenta line, the reflected ray.

where τ is the distance parameter from point N to any point within the line. Said line will cross the sphere of radius n_2 at the points \overline{N}_1 and \overline{N}_2 . The coordinates x, y, z of these points are given by Equation (1.17). The equation of the sphere of radius n_2 is

$$n_2^2 = x^2 + y^2 + z^2. \quad (1.18)$$

Substituting Equations (1.17a), (1.17b) and (1.17c) in Equation (1.18), Equation (1.19) is obtained by grouping terms:

$$\tau^2 + 2n_1\tau(\cos \alpha \cos \lambda + \cos \beta \cos \mu + \cos \gamma \cos \nu) + (n_1^2 - n_2^2) = 0, \quad (1.19)$$

where $(\cos \alpha \cos \lambda + \cos \beta \cos \mu + \cos \gamma \cos \nu)$ belongs to the cosine of the angle formed between the line normal to the surface and the incident ray,

$$\cos I = \cos \alpha \cos \lambda + \cos \beta \cos \mu + \cos \gamma \cos \nu, \quad (1.20)$$

which allows to compact the quadric Equation (1.19) even further:

$$\tau^2 + 2n_1 \cos I + (n_1^2 - n_2^2) = 0, \quad (1.21)$$

which roots are:

$$\tau_1 = -n_1 \cos I + \sqrt{n_1^2 \cos^2 I + (n_2^2 - n_1^2)}, \quad (1.22a)$$

$$\tau_2 = -n_1 \cos I - \sqrt{n_1^2 \cos^2 I + (n_2^2 - n_1^2)}. \quad (1.22b)$$

As previously discussed, the line described by Equation (1.17) crosses the point N located in the sphere of radius n_1 , and by the points \overline{N}_1 and \overline{N}_2 ; from the last two points, the closest one to the first point is chosen to perform the ray refraction; the farthest for the ray reflection.

By using a proper τ , the coordinates \overline{X} , \overline{Y} , \overline{Z} are found:

$$\overline{X} = n_2 \cos \alpha' = X + \tau_j \cos \lambda, \quad (1.23a)$$

$$\overline{Y} = n_2 \cos \beta' = Y + \tau_j \cos \mu, \quad (1.23b)$$

$$\overline{Z} = n_2 \cos \gamma' = Z + \tau_j \cos \nu, \quad (1.23c)$$

where j represents any of the possible values of τ . The emerging ray direction cosines are calculated from Equations (1.23):

$$\cos \alpha' = (X + \tau_j \cos \lambda)/n_2, \quad (1.24a)$$

$$\cos \beta' = (Y + \tau_j \cos \mu)/n_2, \quad (1.24b)$$

$$\cos \gamma' = (Z + \tau_j \cos \nu)/n_2, \quad (1.24c)$$

The emerging ray parametric equations, which known point is the point of intersection of the ray with the optical surface are presented in Equations (1.25a), (1.25b) y (1.25c):

$$x = X_i + \tau' \cos \alpha', \quad (1.25a)$$

$$y = Y_i + \tau' \cos \beta', \quad (1.25b)$$

$$z = Z_i + \tau' \cos \gamma', \quad (1.25c)$$

Ray reflection considerations

In order to reflect the ray using the method previously described it is required to:

- n_2 to have the same absolute value than n_1 , but of opposite sign.
- Preserve n_2 sign for refracting the ray in the following surfaces and using negative axial separation distances until another reflection is performed.

1.5 Summary

In this chapter we laid down the fundamentals for finite raytracing as well as the reference system for this work.

We studied how a ray of light is represented in a three-dimensional space and how to transfer a ray from one surface to the next one and how to refract the rays.

Chapter 2

Optical Path Difference

The capacity of an optical system to form images as predicted by the paraxial approximation is used to assess the system performance. The concepts related to optical path and the equations used for its calculation from finite ray tracing results are presented in this chapter.

2.1 Wave Aberrations and Optical Path

Consider the following optical system, as presented in Figure 2.1. The system forms an image of the object P into the point P' . It is said that there is perfect imaging if the diverging spherical wave arriving to the system is transformed into a converging spherical wave. In a real system, however, the exit wave, in general, is not spherical [35].

The *optical path length* is defined as the geometrical path length the ray travels within a medium, times said medium refractive index n . In an ideal optical imaging system the optical path length is the same for any ray that enters the system. Consider an object point emitting rays that pass through the optical system until they reach the exit pupil in such a way they have travel the same optical path. The ray that crosses the center of the pupil is called the *chief or principal ray* which all rays are compared against. A *wavefront* is defined as the surface that joins all the points that have the same phase and have travelled the same time or the same optical path. If the exit wavefront is a sphere with its center in the paraxial image plane, it is said that the system is perfect [35].

For real systems, the wavefront at the exit pupil is not spherical anymore, and the *optical path difference*, or *OPD*, between the real wavefront and the ideal spherical wavefront is given by Equation (2.1)

$$OPD = [R] - [C], \quad (2.1)$$

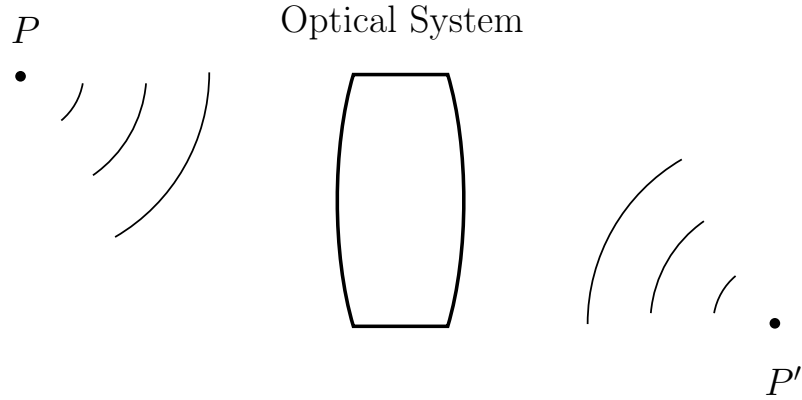


Figure 2.1: An ideal optical system. Light emitted from a point source P propagates through the optical system and is focused at the image point P' [35].

where $[C]$ is the optical path length along the chief ray, and $[R]$ is the optical path length along a typical ray.

The *OPD* is negative if the ray needs to travel additional optical length to reach the reference Gaussian sphere, positive otherwise [36]. In Figure 2.2, the real wavefront is W , the reference Gaussian sphere is G , the Gaussian image is formed at P' . For a real, aberrated wavefront, there is no single point where the rays will converge in the image plane. Following Equation (2.1), the optical path difference is $[\bar{Q}Q]$ and it is a function of the coordinates in the exit pupil.

It is a common practice to express the *OPD* in wavelength units. This is achieved by dividing the *OPD* by the ray's wavelength. If a designer desires to analyse a system using multiple wavelengths, then *OPD* must be calculated as a function of wavelength.

2.2 Hopkins' *OPD* Equation and Tatian's *OPD* Caboose term

Each surface of an optical system contributes with a change in the *OPD* between a common ray and the principal ray. The aberration caused by an interface of two isotropic media is then defined in Equation (2.2):

$$\Delta(W) = W' - W, \tag{2.2}$$

where W and W' are the aberrations of a given ray compared to a reference

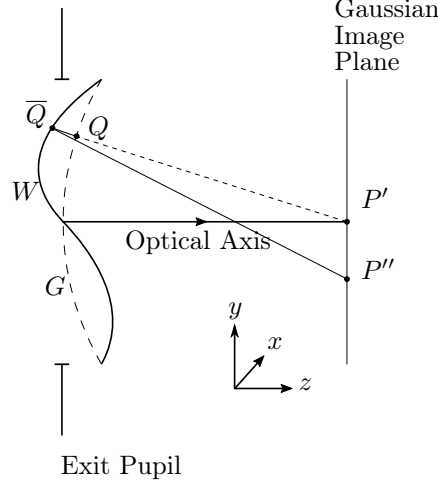


Figure 2.2: Aberrated wavefront at the system exit pupil [35].

ray, of the incident and emitted wave.

H. H. Hopkins [37] developed an equation that calculates the value of Equation (2.2) for each surface in the optical system, as presented in Equation (2.3) in a convenient manner:

$$\Delta(W_j) = n_2 \frac{(P - \bar{P}) \cdot (U' + \bar{U}')}{1 + (U' \cdot \bar{U}')} - n_1 \frac{(P - \bar{P}) \cdot (U + \bar{U})}{1 + (U \cdot \bar{U})}, \quad (2.3)$$

where

j is the j th interface being evaluated,

n_1, n_2 are the refractive indices of the media before and after refraction,

P, \bar{P} are position vectors of the incidence rectangular coordinates of the common and principal ray on the interface,

U, \bar{U} are vectors containing the direction cosines of the common and principal ray before refraction or reflection.

U', \bar{U}' are vectors containing the direction cosines of the common and principal ray after refraction or reflection.

Hopkins names *invariant focus of two skew rays* any point between these rays where the aberration content of the wavefront remains unchanged as the wavefront propagates in space [37]. Remember that the aberration content W is compared against a spherical wavefront. The system total *OPD* is the sum of each surface *OPD* contribution computed with Equation (2.3). This number

2.2. HOPKINS' *OPD* EQUATION AND TATIAN'S *OPD* CABOOSE TERM

is the wavefront deviation from a spherical wave centered in the last invariant focii.

Usually the desired image plane is located in a different position than the invariant focii so a focal shift, or caboose term, is introduced. The total *OPD* change caused by the system and the focal shift is given by Equation (2.4),

$$W' = \sum_{j=1}^k \Delta W_j + \delta W_k \quad (2.4)$$

B. Tatian developed a caboose equation for finite image distances [38], shown in Equation (2.5):

$$\delta W_k = n_i \left\{ I \cdot (\bar{U} - U) + \frac{(U \cdot \bar{U}) \cdot [U \cdot P - \bar{U} \cdot \bar{P}] + (U \cdot \bar{P}) - (\bar{U} \cdot P)}{1 + U \cdot \bar{U}} \right\} \quad (2.5)$$

where

n_i is the image medium refractive index,

I is the position vector of the desired image point,

P, \bar{P} are position vectors of points belonging to the common and principal rays at the image space; and

U, \bar{U} are vectors of direction cosines of the common and principal rays in the image space.

If one is to trace rays up to the image plane, then $I = \vec{0}$.

To handle infinite image distances, Rayces [39] modified Tatian's caboose equation by introducing some new quantities.

1. The distance between the interception of the common and principal rays with the exit pupil plane and the image plane. These quantities are given by Equations (2.6a) and (2.6b), where U_I are the direction cosines of the line orthogonal to the image plane:

$$T = P \cdot U_I, \quad (2.6a)$$

$$\bar{T} = \bar{P} \cdot U_I \quad (2.6b)$$

2. A vector defined by the intersection of the principal and common rays with a plane perpendicular to the principal ray:

$$R_x = (T \cos \alpha - \bar{T} \cos \bar{\alpha}) + (X - \bar{X}), \quad (2.7a)$$

$$R_y = (T \cos \beta - \bar{T} \cos \bar{\beta}) + (Y - \bar{Y}), \quad (2.7b)$$

$$R_z = (T \cos \gamma - \bar{T} \cos \bar{\gamma}) + (Z - \bar{Z}). \quad (2.7c)$$

3. The difference of the unit vectors in the direction of the common ray and principal ray:

$$Q_x = \cos \alpha - \cos \bar{\alpha}, \quad (2.8a)$$

$$Q_y = \cos \beta - \cos \bar{\beta}, \quad (2.8b)$$

$$Q_z = \cos \gamma - \cos \bar{\gamma}. \quad (2.8c)$$

The caboose term for infinite image distance is presented in Equation (2.9):

$$\delta W = -\frac{R_x Q_x + R_y Q_y + R_z Q_z}{1 + \cos \alpha \cos \bar{\alpha} + \cos \beta \cos \bar{\beta} + \cos \gamma \cos \bar{\gamma}} \quad (2.9)$$

2.3 Raytracing and Optical Path Difference calculations

Raytracing and optical path calculation computer programs were developed based on Chapters 1 and Section 2.2. We modelled an Edmund Optics N-LAK22 / N-SF6 achromatic doublet like the one presented in Figure 2.3. This doublet has a diameter D of 12.0 [mm]; the curvatures C_1 , C_2 and C_3 are 17.77, -16.46 and -136.80 [mm], respectively. The axial separation d_1 is 4.50 [mm] and the axial separation d_2 is 2.50 [mm]. Its design range is between 750 and 1550 [nm].

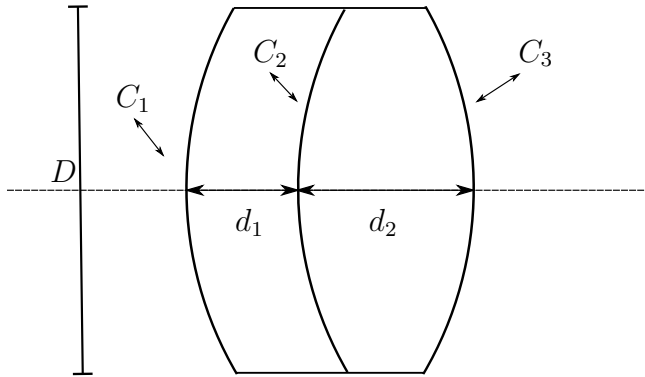


Figure 2.3: N-LAK22 / N-SF6 achromatic doublet. The diameter D is 12.0 [mm]; the curvatures C_1 , C_2 and C_3 are 17.77, -16.46 and -136.80 [mm], respectively. The axial separation d_1 is 4.50 [mm] and the axial separation d_2 is 2.50 [mm]. Its design range is between 750 and 1550 [nm]. Its back focal length BFL for $\lambda = 810$ [nm] is 25.82 [mm].

2.4. SUMMARY

For the raytracing test we chose a designed wavelength of $\lambda = 810$ [nm], hence, the refractive index for N-LAK22 is $n_1 = 1.642440$ and for N-SF6 refractive index $n_2 = 1.783737$. We decided to propagate two rays emanating from a point object located at infinity, so the image plane will be located at the back focal length $BFL = 25.82$ [mm]. The first one will be contained in the optical axis, thus it will be referred as *principal ray*; the second will intersect the first surface at $y = 6$ [mm].

We then compared our results with those provided by the Eikonal computer program by Juan Rayces [40].

The principal difference between our program and Eikonal's is that Eikonal uses the x axis as the optical axis while our software uses the z axis, as previously discussed in Chapter 1. The same ray was traced in both programs, the results are displayed in Tables 2.1 and 2.2.

Surface	x [mm]	y [mm]	z [mm]	$\cos \alpha$	$\cos \beta$	$\cos \gamma$	OPD [λ]
Object Plane	0.000000	6.000000	0.000000	0.000000	0.000000	1.000000	0.000000
1	0.000000	6.000000	1.043587	0.000000	-0.136932	0.990580	-9.208228
2	0.000000	5.661008	-1.004108	0.000000	-0.095571	0.995423	17.393330
3	0.000000	5.334566	-0.104051	0.000000	-0.201541	0.979480	-7.218082
Image Plane	0.000000	0.009426	0.000000	0.000000	-0.201541	0.979480	-0.076010*

Table 2.1: Raytracing and OPD calculations made with our in-house software. We use the z axis as the optical axis. (*) The OPD shown at the image plane was calculated with Equation (2.5).

Surface	x [mm]	y [mm]	z [mm]	$\cos \alpha$	$\cos \beta$	$\cos \gamma$	OPD [λ]
Object Plane	0.000000	6.000000	0.000000	1.000000	0.000000	0.000000	0.000000
1	1.043587	6.000000	0.000000	0.990580	-0.136932	0.000000	-9.208228
2	-1.004108	5.661008	0.000000	0.995423	-0.095571	0.000000	17.393328
3	-0.104051	5.334566	0.000000	0.979480	-0.201541	0.000000	-7.218082
Image Plane	0.000000	0.009426	0.000000	0.979480	-0.201541	0.000000	-0.076018*

Table 2.2: Raytracing and *OPD* calculations obtained from Eikonal Optical Design Software. Eikonal uses the x axis as the optical axis. (*) Eikonal does report ΔW and W' but does not report δW as shown in Equations (2.4) and (2.5), so it must be calculated from the reported total which is truncated to the first three decimal places.

From Tables 2.1 and 2.2 we appreciate that the raytracing and *OPD* calculations are correct.

2.4 Summary

In this chapter we discussed the *Optical Path Difference* concept and how it can help us to determine the performance of an optical system such as the one depicted in Figure 2.3. We reviewed the *OPD* equations used by Hopkins, Tatian and Rayces and tested them in a simulation. We compared our simulation re-

sults against a professional optical design software verifying that our raytracing software works correctly.

2.4. SUMMARY

Chapter 3

Zernike Polynomials and the Wavefront Numerical Analysis

To analyse the aberration content of an optical system Seidel terms or Zernike polynomials are fitted to an *OPD* data set sampled in different parts of the entrance pupil. The aberration content is described by a pupil function obtained by tracing a grid of rays in the entrance pupil and calculating the associated optical path difference for each ray that emerges from the exit pupil.

3.1 Infinite series expansion

The expression for Zernike circle polynomials as an infinite series expansion is given by Equation (3.1),

$$W(\rho, \theta) = A_{00} + \sum_{n=2}^{\infty} A_{n0} R_n^0(\rho) + \sum_{n=1}^{\infty} \sum_{m=1}^n A_{nm} R_n^m(\rho) \cos m\theta \quad (3.1)$$

where R_n^m are the *radial polynomials*, described by Equation (3.2):

$$R_n^m(\rho) = \sum_{s=0}^{\frac{n-m}{2}} (-1)^s \frac{(n-s)!}{s! \left(\frac{n+m}{2} - s\right)! \left(\frac{n-m}{2} - s\right)!} \rho^{n-2s}. \quad (3.2)$$

If the optical system contains tilts, decenters or optical defects while maintaining a circular aperture, the polynomial undergoes a relative rotation expressed by the phase angle ϕ_{nm} which is subtracted from $m\theta$, yielding Equation (3.3),

3.2. ZERNIKE POLYNOMIAL INDICES AND CONCISE NOTATION FOR DISCRETE DATA

$$W(\rho, \theta) = A_{00} + \sum_{n=2}^{\infty} A_{n0} R_n^0(\rho) + \sum_{n=1}^{\infty} \sum_{m=1}^n A_{nm} R_n^m(\rho) (\cos [m\theta - \phi_{nm}]), \quad (3.3)$$

which can be rewritten as Equation (3.4),

$$W(\rho, \theta) = A_{00} + \sum_{n=2}^{\infty} A_{n0} R_n^0(\rho) + \sum_{n=1}^{\infty} \sum_{m=1}^n R_n^m(\rho) (a_{nm} \cos m\theta - b_{nm} \sin m\theta), \quad (3.4)$$

where

$$a_{nm} = A_{nm} \cos \phi_{nm}, b_{nm} = A_{nm} \sin \phi_{nm}.$$

Zernike circle polynomials form an *orthogonal set* [35]. This implies that the expansion coefficients can be calculated separated one from another by using an integral and fulfilling the least squares principle and that the wavefront aberration variance is given by

$$\text{var}(W) = \sum_{n=2}^{\infty} \frac{A_{n0}^2}{n+1} + \sum_{n=1}^{\infty} \sum_{m=1}^n \frac{A_{nm}^2}{2(n+1)}. \quad (3.5)$$

To simplify Equation (3.5) the renormalized coefficients \hat{A}_{nm} proposed by Chimera and Hufnagel are presented in the work of Rayces [41]:

$$\hat{A}_{nm} = \frac{A_{mn}}{\sqrt{n+1}} \text{ for } m = 0, \quad (3.6a)$$

$$\hat{A}_{nm} = \frac{A_{mn}}{\sqrt{2(n+1)}} \text{ for } m > 0, \quad (3.6b)$$

simplifying Equation (3.5) to

$$\text{var}(W) = \sum_{n=1}^{\infty} \sum_{m=0}^n \hat{A}_{nm}^2, \quad (3.7)$$

which allows all the coefficients A_{nm} to be interpreted as peak wave values and all the coefficients \hat{A}_{nm} as wavefront RMS errors.

In Eikonal the renormalized coefficients are used to describe the aberration content of an optical system and they were adopted for this work for comparison purposes.

3.2 Zernike polynomial indices and concise notation for discrete data

Since the Zernike circle polynomials form an orthogonal set [35], one can define Equation (3.8)

$$C_n^m(\rho, \theta) = R_n^m(\rho) \cos m\theta \quad (3.8)$$

as the even term and Equation (3.9)

$$S_n^m(\rho, \theta) = R_n^m(\rho) \sin m\theta \quad (3.9)$$

as the odd term from Equation (3.4). An important property of orthogonal sets of functions, such as the Zernike circle polynomials, is that the coefficients can be computed independently from one another [41].

Although the radial polynomials use the notation $R_n^m(\rho)$, when writing a computer program it may be convenient to represent them using a single index notation. Given that a finite number of terms are used for the wavefront aberration expansion, in Figure 3.1 the algorithm to generate Z_ℓ data is presented. This algorithm is used to determine the order of Zernike polynomials as described by Rayces [41].

Let

$$Z_\ell(\rho, \theta) \text{ denote either } C_n^m(\rho, \theta) \text{ or } S_n^m(\rho, \theta) \text{ and} \quad (3.10a)$$

$$e_\ell \text{ denote either } a_{nm} \text{ or } b_{nm} \quad (3.10b)$$

Then the Zernike polynomial can be written as

$$W(\rho, \theta) = \sum_{\ell=0}^L e_\ell Z_\ell(\rho, \theta) \quad (3.11)$$

On Table 3.1 we present the first 25 elements of Equation (3.4) using the double and single index notation. Implementing this analytical form of the Zernike polynomials allows for faster computer simulations since the numerical evaluation of Equation (3.2) is an expensive operation.

3.2. ZERNIKE POLYNOMIAL INDICES AND CONCISE NOTATION FOR DISCRETE DATA

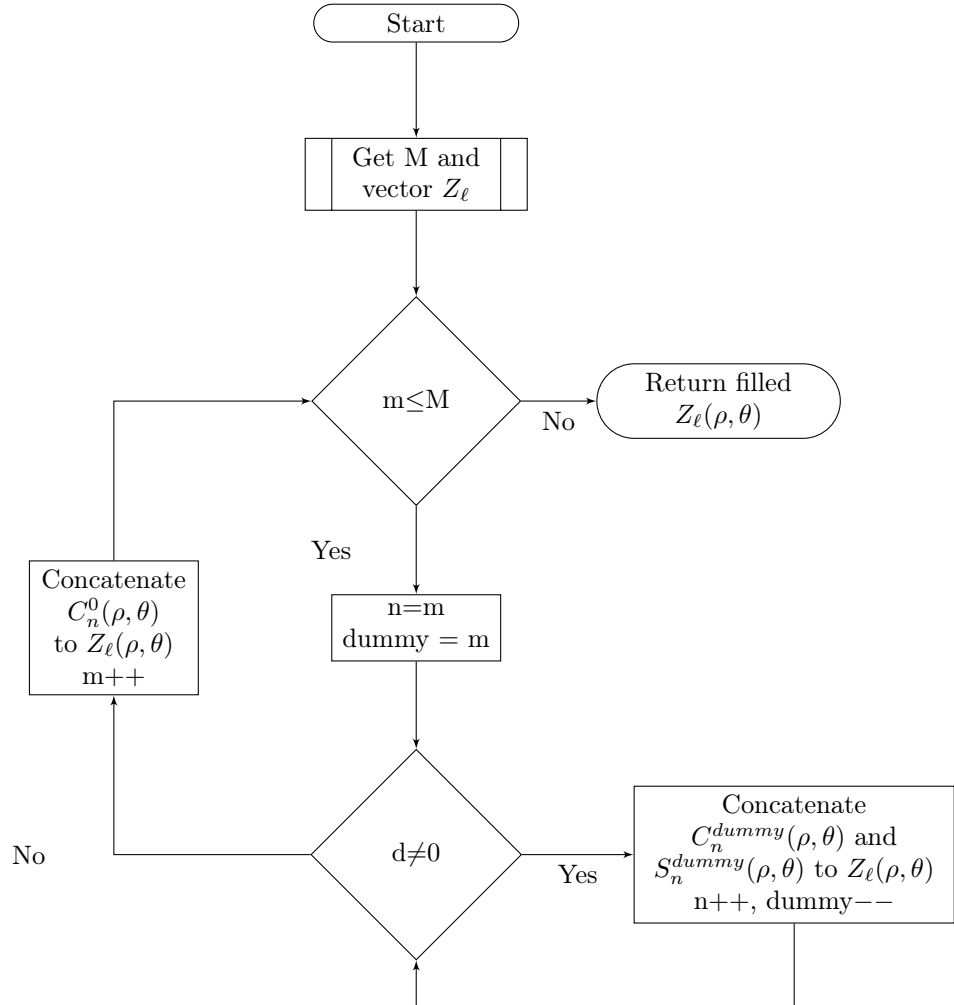


Figure 3.1: Algorithm to generate Zernike circle polynomial indices. The generated data is stored in a structure, which is used to evaluate the corresponding circle polynomial when using the sequential numbering [41].

3.3. LEAST SQUARES FITTING OF ZERNIKE POLYNOMIAL COEFFICIENTS

Aberration name	Double index	Single index	Expression
Piston	$C_0^0(\rho, \theta)$	$Z_0(\rho, \theta)$	1
Vertical axis tilt	$C_1^1(\rho, \theta)$	$Z_1(\rho, \theta)$	$\rho \cos \theta$
Horizontal axis tilt	$S_1^1(\rho, \theta)$	$Z_2(\rho, \theta)$	$\rho \sin \theta$
Defocus	$C_2^0(\rho, \theta)$	$Z_3(\rho, \theta)$	$(2\rho^2 - 1)$
Astigmatism, even, 3rd order	$C_2^2(\rho, \theta)$	$Z_4(\rho, \theta)$	$\rho^2 \cos 2\theta$
Astigmatism, odd, 3rd order	$S_2^2(\rho, \theta)$	$Z_5(\rho, \theta)$	$\rho^2 \sin 2\theta$
Coma, even, 3rd order	$C_3^1(\rho, \theta)$	$Z_6(\rho, \theta)$	$(3\rho^3 - 2\rho) \cos \theta$
Coma, odd, 3rd order	$S_3^1(\rho, \theta)$	$Z_7(\rho, \theta)$	$(3\rho^3 - 2\rho) \sin \theta$
Spherical aberration, 3rd order	$C_4^0(\rho, \theta)$	$Z_8(\rho, \theta)$	$(6\rho^4 - 6\rho^2 + 1)$
Clover leaf, even, 5th order	$C_3^3(\rho, \theta)$	$Z_9(\rho, \theta)$	$\rho^3 \cos 3\theta$
Clover leaf, odd, 5th order	$S_3^3(\rho, \theta)$	$Z_{10}(\rho, \theta)$	$\rho^3 \sin 3\theta$
Astigmatism, even, 5th order	$C_4^2(\rho, \theta)$	$Z_{11}(\rho, \theta)$	$(4\rho^4 - 3\rho^2) \cos 2\theta$
Astigmatism, odd, 5th order	$S_4^2(\rho, \theta)$	$Z_{12}(\rho, \theta)$	$(4\rho^4 - 3\rho^2) \sin 2\theta$
Coma, even, 5th order	$C_5^1(\rho, \theta)$	$Z_{13}(\rho, \theta)$	$(10\rho^5 - 12\rho^3 + 3\rho) \cos \theta$
Coma, odd, 5th order	$S_5^1(\rho, \theta)$	$Z_{14}(\rho, \theta)$	$(10\rho^5 - 12\rho^3 + 3\rho) \sin \theta$
Spherical aberration, 5th order	$C_6^0(\rho, \theta)$	$Z_{15}(\rho, \theta)$	$(20\rho^6 - 30\rho^4 + 12\rho^2 - 1)$
Ashtray, even, 7th order	$C_4^4(\rho, \theta)$	$Z_{16}(\rho, \theta)$	$\rho^4 \cos 4\theta$
Ashtray, odd, 7th order	$S_4^4(\rho, \theta)$	$Z_{17}(\rho, \theta)$	$\rho^4 \sin 4\theta$
Clover leaf, even, 7th order	$C_5^3(\rho, \theta)$	$Z_{18}(\rho, \theta)$	$(5\rho^5 - 4\rho^3) \cos 3\theta$
Clover leaf, odd, 7th order	$S_5^3(\rho, \theta)$	$Z_{19}(\rho, \theta)$	$(5\rho^5 - 4\rho^3) \sin 3\theta$
Astigmatism, even, 7th order	$C_6^2(\rho, \theta)$	$Z_{20}(\rho, \theta)$	$(15\rho^6 - 20\rho^4 + 6\rho^2) \cos 2\theta$
Astigmatism, odd, 7th order	$S_6^2(\rho, \theta)$	$Z_{21}(\rho, \theta)$	$(15\rho^6 - 20\rho^4 + 6\rho^2) \sin 2\theta$
Coma, even, 7th order	$C_7^1(\rho, \theta)$	$Z_{22}(\rho, \theta)$	$(35\rho^7 - 60\rho^5 + 30\rho^3 - 4\rho) \cos \theta$
Coma, odd, 7th order	$S_7^1(\rho, \theta)$	$Z_{23}(\rho, \theta)$	$(35\rho^7 - 60\rho^5 + 30\rho^3 - 4\rho) \sin \theta$
Spherical aberration, 7th order	$C_8^0(\rho, \theta)$	$Z_{24}(\rho, \theta)$	$(70\rho^8 - 140\rho^6 + 90\rho^4 - 20\rho^2 + 1)$

Table 3.1: Zernike polynomials using the double and single index notation [35, 40, 41].

3.3 Least Squares fitting of Zernike polynomial coefficients

Equation (3.11) represents the wave aberration function in a given position. The ω wavefront aberration samples can be stored in a vector \mathbf{w} ; there are L expansion coefficients e_ℓ stored in a vector \mathbf{e} and finally, a matrix of size $L \times \omega$ \mathbf{Z} can be formed with the circle polynomials Z_ℓ . Thus, Equation (3.11) can be written in matrix notation:

$$\mathbf{w} = \mathbf{Z}\mathbf{e}, \quad (3.12)$$

where \mathbf{e} is the variable to be found using a least squares fit.

3.3. LEAST SQUARES FITTING OF ZERNIKE POLYNOMIAL COEFFICIENTS

Since it is a least squares fit, it is desired to determine a vector $\hat{\mathbf{e}}$ such that the error is minimum, as shown in Equation (3.13):

$$\|\mathbf{w} - \mathbf{Z}\hat{\mathbf{e}}\| = \text{minimum}. \quad (3.13)$$

Following the process to compute the least squares fit of data to a polynomial [42], it is known that $\hat{\mathbf{e}}$ satisfies Equation (3.14)

$$\mathbf{Z}^T \mathbf{Z} \hat{\mathbf{e}} = \mathbf{Z}^T \mathbf{w}, \quad (3.14)$$

where $\mathbf{Z}^T \mathbf{Z}$ and $\mathbf{Z}^T \mathbf{w}$ can be computed directly by Equations (3.15) and (3.16):

$$\mathbf{Z}^T \mathbf{Z} = \begin{bmatrix} \sum_{t=0}^{\omega} Z_0^2(t) & \sum_{t=0}^{\omega} Z_1(t)Z_0(t) & \cdots & \sum_{t=0}^{\omega} Z_{\ell}(t)Z_0(t) & \cdots & \sum_{t=0}^{\omega} Z_L(t)Z_0(t) \\ \sum_{t=0}^{\omega} Z_0(t)Z_1(t) & \sum_{t=0}^{\omega} Z_1^2(t) & \cdots & \sum_{t=0}^{\omega} Z_{\ell}(t)Z_1(t) & \cdots & \sum_{t=0}^{\omega} Z_L(t)Z_1(t) \\ \vdots & \vdots & \ddots & \vdots & \vdots & \vdots \\ \sum_{t=0}^{\omega} Z_0(t)Z_{\ell}(t) & \sum_{t=0}^{\omega} Z_1(t)Z_{\ell}(t) & \cdots & \sum_{t=0}^{\omega} Z_{\ell}^2(t) & \cdots & \sum_{t=0}^{\omega} Z_L(t)Z_{\ell}(t) \\ \vdots & \vdots & \vdots & \vdots & \ddots & \vdots \\ \sum_{t=0}^{\omega} Z_0(t)Z_L(t) & \sum_{t=0}^{\omega} Z_1(t)Z_L(t) & \cdots & \sum_{t=0}^{\omega} Z_{\ell}(t)Z_L(t) & \cdots & \sum_{t=0}^{\omega} Z_L^2(t) \end{bmatrix} \quad (3.15)$$

and

$$\mathbf{Z}^T \mathbf{w} = \begin{bmatrix} \sum_{t=0}^{\omega} Z_0(t)W(t) \\ \sum_{t=0}^{\omega} Z_1(t)W(t) \\ \vdots \\ \sum_{t=0}^{\omega} Z_{\ell}(t)W(t) \\ \vdots \\ \sum_{t=0}^{\omega} Z_L(t)W(t) \end{bmatrix}, \quad (3.16)$$

where t is used as a shorthand for (ρ, θ) .

The solution for Equation (3.12) is denoted by Equation (3.17):

$$\hat{\mathbf{e}} = (\mathbf{Z}^T \mathbf{Z})^{-1} \mathbf{Z}^T \mathbf{w}. \quad (3.17)$$

Equation (3.12) can be solved as a system of linear equations. However, a common issue of linear least squares problems are that they involve large quantities of data, and they are ill-conditioned for numerical solution. Golub [43]

proposed a matrix decomposition based on orthogonal Householder transformations [44].

3.4 Aberration content calculation for an achromatic doublet

The aberration content calculation for the achromatic doublet lens used as an example in Section 2.3.

As presented in Figure 2.3, The diameter D is 12.0 [mm]; the curvatures C_1 , C_2 and C_3 are 17.77, -16.46 and -136.80 [mm], respectively; the axial separation d_1 is 4.50 [mm] and the axial separation d_2 is 2.50 [mm]. Its back focal length BFL for $\lambda = 810$ [nm] is 25.818655 [mm].

In this example we draw a square grid of size of $N \times N$ nodes with $N = 128$ over the first surface, tracing collimated rays that are inside the lens diameter.

In Table 3.2 we present the renormalized coefficients obtained from our in-house least-squares Zernike polynomial fit and Eikonol's results. After rounding to the second decimal place we conclude that our implementation works properly.

Aberration name	Renormalized coefficients	Eikonol [λ]	In-house [λ]
Piston	\hat{e}_0	Not reported	-0.44
Defocus	\hat{e}_3	-0.31	-0.31
Spherical aberration, 3rd order	\hat{e}_8	-0.01	-0.01
Spherical aberration, 5th order	\hat{e}_{15}	0.04	0.04

Table 3.2: Comparison of the renormalized aberration coefficients obtained from Eikonol and from our least-squares Zernike polynomial fit using the first 25 elements for the propagation of a collimated beam through an achromatic doublet . The obtained values were rounded to the second most-significant figure. All omitted coefficients in this table are considered to be zero.

To further test our in-house software, we propagated a collimated beam from an off-axis point source located at infinity in a way that the principal ray forms a 2-degree angle with the optical axis through the previously discussed achromatic doublet. In other words, the director cosines of the principal ray are $\cos \alpha = 0.999391$, $\cos \beta = -0.034899$ and $\cos \gamma = 0.000000$. We show the renormalized Zernike coefficients obtained from our in-house software and Eikonol on Table 3.3. There is a slight difference on the values of the recovered coefficients and it is attributed to differences on the Zernike polynomial fitting algorithms used by Eikonol.

3.5. SUMMARY

Aberration name	Renormalized coefficients	Eikonal [λ]	In-house [λ]
Piston	\hat{e}_0	Not reported	-0.44
Vertical axis tilt	\hat{e}_1	Not reported	0.66
Defocus	\hat{e}_3	-0.75	-0.72
Astigmatism, even, 3rd order	\hat{e}_4	-0.26	-0.23
Coma, even, 3rd order	\hat{e}_6	0.24	0.22
Spherical aberration, 3rd order	\hat{e}_8	-0.01	-0.01
Coma, even, 5th order	\hat{e}_{13}	-0.02	-0.01
Spherical aberration, 5th order	\hat{e}_{15}	0.04	0.04

Table 3.3: Comparison of the renormalized aberration coefficients obtained from Eikonal and from our least-squares Zernike polynomial fit using the first 25 elements for the propagation of a beam incident on the achromatic doublet with a 2-degree angle with respect to the optical axis. The obtained values were rounded to the second most-significant figure. All omitted coefficients in this table are considered to be zero.

3.5 Summary

In this chapter we reviewed the Zernike polynomials and their use to assess the aberration content in a given optical system. The first 25 elements of the Zernike polynomials expansion are presented in Table 3.1. We also studied how to perform a linear least-squares fit to the Zernike polynomials and tested our implementation with the achromatic doublet presented in Section 2.3, comparing against the Eikonal Optical Design software achieving the same results up to the second decimal place as shown in Table 3.2 for a collimated beam and with slight variations for an off-axis beam as shown in Table 3.3.

Chapter 4

Phase Shifting Interferometry

A direct application of this work is measuring aberrations in optical components manufactured at the *Laboratorio Universitario de Fabricación de Equipo Óptico - LUFABEO* (University Laboratory for Optical Equipment Fabrication) on the Institute of Applied Science and Technology at UNAM.

In order to manufacture any mirror or lens at *LUFABEO* we require to assess how the emerging wavefront deviates from a given reference. We can achieve this by building an interferometer, a device that allows us to superimpose a known wave and a wave affected by our test component, and by the phenomenon of interference we can find useful information.

At the time this work was written (second half of 2020), a Fizeau interferometer is being built at the *LUFABEO*. To extract information from interferometric measurements, we decided to use the *Phase Shifting Interferometry* family of algorithms. We will discuss some algorithms and their performance using experimental interferograms.

4.1 PSI principle of operation

Phase Shifting Interferometry (PSI) calculates the phase difference between a test beam and a reference beam via the variations of intensity in the generated interference pattern. This condition is fulfilled by the Fizeau interferometer.

This technique records a series of interferograms while the reference phase of the interferometer is modified. The test wavefront is encoded within the intensity pattern of the interferogram and for its recovery, point-to-point calculations are required [45].

A phase shift is introduced between the reference and test wavefronts. A time-varying signal is produced, where the phase difference is encoded in each point where the interference was measured.

The phase shift introduced between the reference and test wavefronts is known, so the phase can be determined with no ambiguity.

4.2. SAMPLE INTERFEROGRAMS

The general expressions for the reference and test wavefronts in the interferometer are

$$w_R(x, y, t) = a_R(x, y) \exp[i(\Theta_R(x, y) - \delta(t))] \quad (4.1a)$$

$$w_T(x, y) = a_T(x, y) \exp[i\Theta_T(x, y)] \quad (4.1b)$$

The final intensity pattern is

$$I(x, y, t) = |w_R(x, y, t) + w_T(x, y)|^2,$$

which can be rewritten as

$$I(x, y, t) = I'(x, y) + I''(x, y) \cos(\Theta(x, y) - \delta(t)), \quad (4.2)$$

having

$$I'(x, y) = a_R^2(x, y) + a_T^2(x, y), \quad (4.3a)$$

$$I''(x, y) = 2a_R^2(x, y)a_T^2(x, y), \quad (4.3b)$$

$$\Theta(x, y) = \Theta_R - \Theta_T, \quad (4.3c)$$

where $\Theta(x, y)$ is the phase difference between the reference and test wavefronts, $I'(x, y)$ is the average interferometer intensity, $I''(x, y)$ is the half of the peak-valley intensity modulation and δ is a variable phase displacement between the interfering beams [46].

4.2 Sample interferograms

To implement PSI we require to capture a series of interferograms with different phase shifts. These phase shifts can linearly vary in a range of T during the imaging sensor integration time so that the sample interferogram at the phase shift $\delta(n)$ is the integral of the interference pattern from $(\delta(n) - T/2)$ to $(\delta(n) + T/2)$ as shown in Equation (4.4) [47]:

$$I(x, y, n) = \frac{1}{T} \int_{(\delta(n)-T/2)}^{(\delta(n)+T/2)} I(x, y, \delta(n)) d(\delta(n)). \quad (4.4)$$

Integrating Equation (4.4) we obtain

$$\begin{aligned} I(x, y, n) = & I'(x, y) - \\ & \frac{1}{T} I''(x, y) \{ \sin[\Theta(x, y) - \delta(n) - T/2] - \\ & \sin[\Theta(x, y) - \delta(n) + T/2] \}, \end{aligned} \quad (4.5)$$

which can be simplified to

$$I(x, y, n) = I'(x, y) + I''(x, y) \operatorname{sinc}(T/2) \cos[\Theta(x, y) - \delta(n)]. \quad (4.6)$$

If the T term in Equation (4.6) tends to zero, means that the detected phase does not change during the interference pattern acquisition, so Equation (4.6) can further be reduced to

$$I(x, y, n) = I'(x, y) + I''(x, y) \cos[\Theta(x, y) - \delta(n)]. \quad (4.7)$$

4.3 PSI linear least-squares fitting

To measure phase by PSI we require to acquire a series of sample interferograms $I(x, y, n)$ taken at different phase shifts $\delta(n)$. The intensity on an interferogram point (x, y) will vary in a sinusoidal fashion with $\delta(n)$, hence, the phase $\Theta(x, y)$ can be obtained by fitting the data from each (x, y) point to a sine curve of a known period and unknown phase and amplitude [47].

A number N of sample interferograms using the same integration window T is taken. The value of each interferogram is given by Equation (4.6), which can be rewritten to be used in linear least-squares fitting:

$$\begin{aligned} I(x, y, n) = & I'(x, y) + \\ & I''(x, y) \operatorname{sinc}(T/2) \cos[\Theta(x, y)] \cos(\delta(n)) + \\ & I''(x, y) \operatorname{sinc}(T/2) \sin[\Theta(x, y)] \sin(\delta(n)), \end{aligned} \quad (4.8)$$

which is of the form of

$$I(x, y, n) = a_0(x, y) + a_1(x, y)f_1(\delta(n)) + a_2(x, y)f_2(\delta(n)), \quad (4.9)$$

where

- $a_0(x, y) = I'(x, y)$,
- $a_1(x, y) = I''(x, y) \operatorname{sinc}(T/2) \cos[\Theta(x, y)] \cos(\delta(n))$,
- $f_1(\delta(n)) = \cos(\delta(n))$,
- $a_2(x, y) = I''(x, y) \operatorname{sinc}(T/2) \sin[\Theta(x, y)] \sin(\delta(n))$, y
- $f_2(\delta(n)) = \sin(\delta(n))$,

The $a(x, y)$ terms are the unknown terms on this equation system, depicted in matrix form in Equation (4.10) were we dropped the $\delta(n)$ dependency found in $f_1(\delta(n))$ and $f_2(\delta(n))$ for the sake of clarity,

$$\begin{bmatrix} N & \sum f_1 & \sum f_2 \\ \sum f_1 & \sum f_1^2 & \sum f_1 f_2 \\ \sum f_2 & \sum f_1 f_2 & \sum f_2^2 \end{bmatrix} \begin{bmatrix} a_0(x, y) \\ a_1(x, y) \\ a_2(x, y) \end{bmatrix} = \begin{bmatrix} \sum I_i(x, y) \\ \sum I_i(x, y) f_1 \\ \sum I_i(x, y) f_2 \end{bmatrix}, \quad (4.10)$$

which is solved by Equation (4.11):

$$\begin{bmatrix} a_0(x, y) \\ a_1(x, y) \\ a_2(x, y) \end{bmatrix} = \begin{bmatrix} N & \sum f_1 & \sum f_2 \\ \sum f_1 & \sum f_1^2 & \sum f_1 f_2 \\ \sum f_2 & \sum f_1 f_2 & \sum f_2^2 \end{bmatrix}^{-1} \begin{bmatrix} \sum I_i(x, y) \\ \sum I_i(x, y) f_i \\ \sum I_i(x, y) f_2 \end{bmatrix}. \quad (4.11)$$

Equation (4.10) is solved for every interferogram point (x, y) in order to obtain $a_1(x, y)$ and $a_2(x, y)$ terms. The phase map is given by

$$\Theta(x, y) = \arctan \left[\frac{a_2(x, y)}{a_1(x, y)} \right], \quad (4.12)$$

and the interferogram fringe contrast is obtained by

$$\gamma(x, y) = \frac{I''(x, y)}{I'(x, y)} = \frac{\sqrt{a_1(x, y)^2 + a_2(x, y)^2}}{a_0(x, y) \operatorname{sinc}(T/2)}. \quad (4.13)$$

Since the phase calculated by Equation (4.12) is a phase map bounded between two values depending on the algorithm used, $[-\pi, \pi]$ for MATLAB's *atan2* function [48], we require to add and subtract 2π at each discontinuity on the map. This process is called *phase unwrapping*. 2-D phase unwrapping algorithms are available such as Goldstein's algorithm [49] which were used to process the retrieved phase.

4.4 SSPCA

An important limitation of Equation (4.7) is that it assumes that the phase shift is constant across every interferogram (x, y) position. This means Equation (4.7) does not consider tilts on the vertical and horizontal axis caused by vibrations, uneven displacements, device calibration errors and other sources.

Equation (4.7) was modified to include vertical and horizontal tilts as seen in Equation (4.14) [50],

$$I(x, y, n) = I'(x, y) + I''(x, y) \cos [\Theta(x, y) - \Delta(x, y, n)], \quad (4.14)$$

where $\Delta(x, y, n)$ represents the phase shift plane and its described by Equation (4.15),

$$\Delta(x, y, n) = \alpha(n)x + \beta(n)y + \delta(n) \quad (4.15)$$

where $\alpha(n)$ and $\beta(n)$ are the vertical and horizontal tilt coefficients for a given interferogram n on the PSI sequence.

Rewriting Equation (4.14) we find that

$$I(x, y, n) - I'(x, y) = \cos [\Delta(x, y, n)]I_c + \sin [\Delta(x, y, n)]I_s \quad (4.16)$$

where

$$I_c = I''(x, y) \cos \Theta(x, y), \quad (4.17a)$$

$$I_s = I''(x, y) \sin \Theta(x, y) \quad (4.17b)$$

From the previous analysis we can deduce that methods like the one described on Section 4.3 may not be accurate for the situation modelled by Equation (4.16).

We implemented an algorithm that applies a statistical tool called *Principal Component Analysis (PCA)* and linear least-squares regression to PSI to calculate the different phase planes $\Delta(x, y, n)$ [50].

We will first discuss what is the Principal Component Analysis, then how it is used to retrieve the phase from the PSI measurement.

4.4.1 Principal Component Analysis

The objective of *Principal Component Analysis* is to reduce the dimensionality of a set of data which is comprised of a large number of interrelated variables, while preserving most of their variability as possible. This is achieved by transforming the original variables into a new system, the principal components system which are not correlated to each other and they are ordered that the first few principal components retain most of the variability of the original variables [51].

Vargas et al. developed the application of this technique in PSI [52] and it comprises three steps. For this part, we assume that the interference fringes are modelled by Equation (4.7), that is, with no tilted phase shift.

We start with N interferograms of N_x by N_y pixels and these pixels can be arranged as

$$\mathbf{x} = [x_1, x_2, \dots, x_n]^T, \quad (4.18)$$

where x_n is a column vector made up with the pixels of an interferogram distributed based on the interferogram column order. Each column of \mathbf{x} represents a whole interferogram.

The first step on the PCA PSI process is to obtain the covariance matrix \mathbf{C} from \mathbf{x} via Equation (4.19):

$$\mathbf{C} = (\mathbf{x} - \mathbf{m}_x)(\mathbf{x} - \mathbf{m}_x)^T, \quad (4.19)$$

where \mathbf{m}_x has the same size than \mathbf{x} and its members are the average value of each \mathbf{x} column. This can be understood as a background-suppressing operation.

The second step is to diagonalize the covariance matrix \mathbf{C} to find its eigenvalues and eigenvectors, as seen in Equation (4.20):

$$\mathbf{D} = \mathbf{A}\mathbf{C}\mathbf{A}^T, \quad (4.20)$$

where \mathbf{D} is a diagonal matrix and \mathbf{A} is a transformation matrix.

The third step is to calculate the principal components using the Hotelling transform:

$$\mathbf{y} = \mathbf{A}(\mathbf{x} - \mathbf{m}_x), \quad (4.21)$$

We choose the first two columns of \mathbf{y} with the biggest eigenvalues, whose vectors we will associate with I_c and I_s described in Equations (4.17a) and (4.17b). The phase is recovered with Equation (4.22):

$$\Theta(x, y) = \arctan(-I_s/I_c). \quad (4.22)$$

The assignment of the first two principal components to I_c and I_s is arbitrary [52], however, in an experimental setting we have control of the piston phase shift δ , so we can use that information to set the true sign of the measured phase.

4.4.2 Self-adaptive selection of interferogram subblocks and PCA (SSPCA)

The *self-adaptive selection of interferogram subblocks and principal component analysis*, SSPCA algorithm is a method that promises to remove the tilt error found in laboratory measurements [50].

This algorithm can be summarized in the following steps:

- Divide each interferogram frame in m subblocks and calculate the local phase $\Theta_m(x, y)$ for every subblock using the PCA PSI algorithm. We assume that there is an uniform phase shift δ_m for each subblock and we calculate this quantity using $\Theta_m(x, y)$ and a linear least-squares fit.
- For each subblock we obtain a curve of $\delta_m(n)$ values bounded between $[-\pi, \pi]$. Once unwrapped we check if the processed curve was unwrapped properly by calculating the correlation coefficients between the processed curve and the rest. If the correlation coefficients are above a user-set threshold we consider the subblock to be valid. We correct the sign for $\delta_m(n)$ using the known piston phase shift sign from the experimental setup.
- The $\delta_m(n)$ values of every valid subblock are used to calculate each $\Delta(x, y, n)$ plane using a linear least-squares fit.
- The fitted $\Delta(x, y, n)$ are plugged as known values into Equation (4.16) for another linear least-squares fit where we calculate $\Theta(x, y)$.

4.5 PSI simulations

To test the performance of the PSI algorithms previously discussed we generated a test OPD surface using the Zernike polynomials, as shown as in Figure 4.1, with even 3rd order coma $Z_6(\rho, \theta) = -0.30[\lambda]$, 3rd order spherical aberration

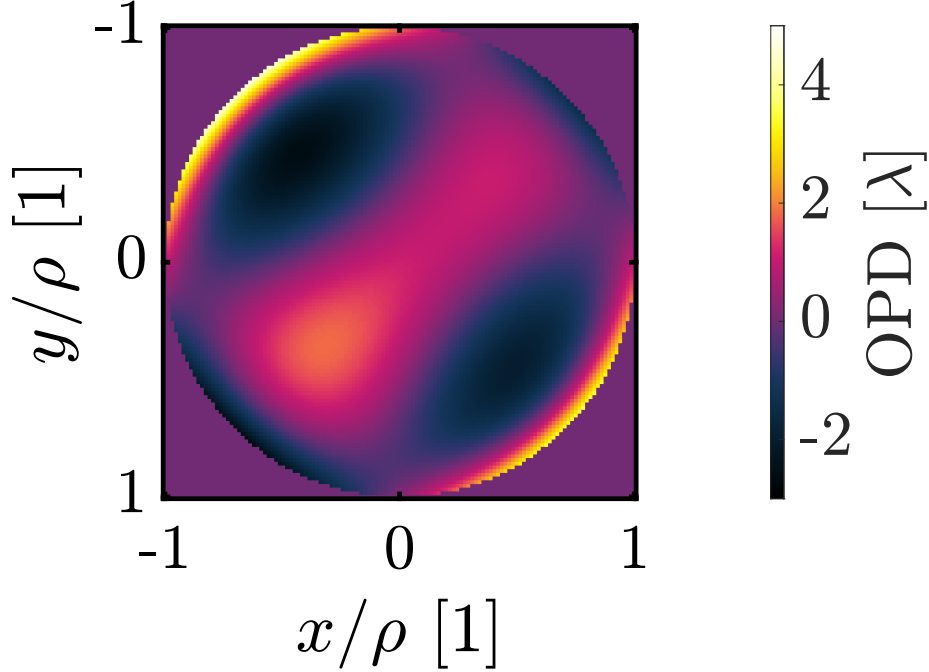


Figure 4.1: Test OPD surface for a unitary pupil of diameter $D = 2\rho$ with even 3rd order coma $Z_6(\rho, \theta) = -0.30[\lambda]$, 3rd order spherical aberration $Z_8(\rho, \theta) = 0.50[\lambda]$ and 5th order odd astigmatism $Z_{12}(\rho, \theta) = 1[\lambda]$.

$Z_8(\rho, \theta) = 0.50[\lambda]$ and 5th order odd astigmatism $Z_{12}(\rho, \theta) = 1[\lambda]$. Keep in mind that the OPD surface units are $[\lambda]$.

For our simulated interference patterns we will encode our OPD using Equation (4.14) with the following parameters:

- Step size between interferograms $d = 10 [\mu\text{m}]$ taking 10 interferograms numbered from $n = 0$ to $n = 9$,
- carrier wavelength $\lambda = 632.8 [\text{nm}]$,
- unit pupil sampled with a 128-by-128 grid,
- linear phase shift $\delta(n) = \frac{2\pi dn}{\lambda}$
- background intensity $I'(x, y) = 2 + \sin[20\pi(x + y)]$,
- modulation intensity $I''(x, y) = 1$,
- horizontal phase tilt coefficient $\alpha(n) = \frac{2\pi n}{\lambda} * 50 \times 10^{-9}$, and
- vertical phase tilt coefficient $\beta(n) = \frac{-2\pi n}{\lambda} * 25 \times 10^{-9}$.

4.5. PSI SIMULATIONS

The first four simulated interferograms are displayed on Figure 4.2. The 10 interferogram frames were used as inputs for the least-squares and the SSPCA algorithms discussed previously. For the SSPCA algorithm we used subblock sizes of 16-by-16, 8-by-8 and 4-by-4 pixels in order to study their impact on the retrieved phase results. We present the recovered and reconstructed OPD maps using the least-squares and SSPCA algorithms on Figure 4.3 where row 1) is the least-squares result; 2), 3), 4) depict the recovered OPD maps using the SSPCA algorithm with subblocks of size 16-by-16, 8-by-8 and 4-by-4. Column a) represents the recovered OPD map from every algorithm; column b) is the OPD surface generated by the fitted Zernike polynomial coefficients and column c) is the generated OPD surface when omitting piston, tilt and defocus coefficients.

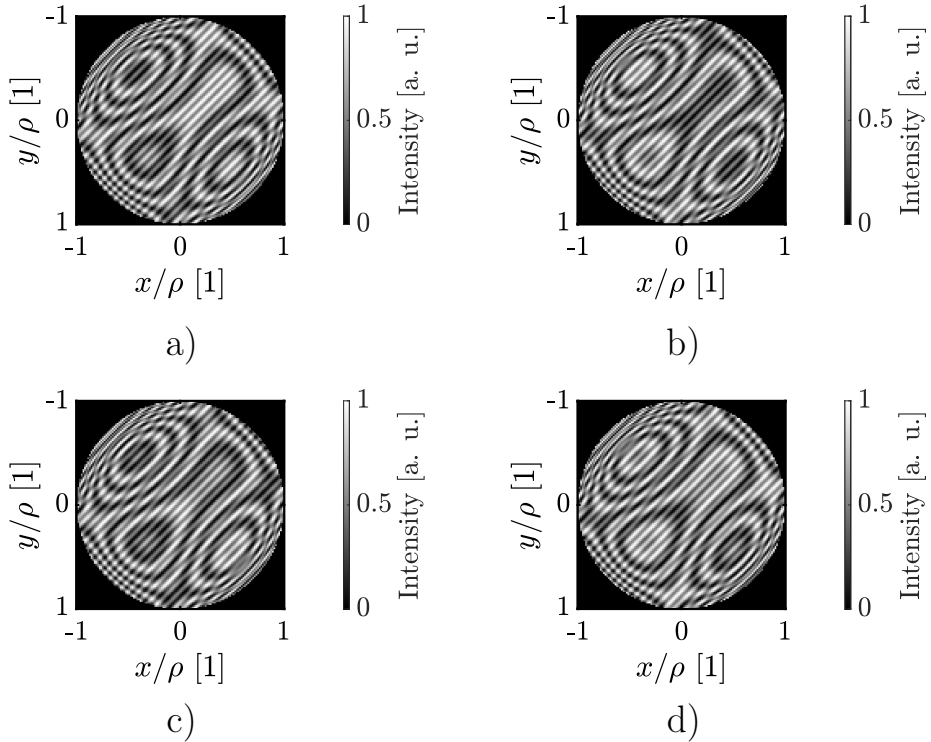


Figure 4.2: First four simulated interferogram frames for a normalized pupil of diameter $D = 2\rho$ using the OPD shown in Figure 4.1. The following parameters were used into Equation (4.14): $d = 10$ [μm], 10 interferograms, $\lambda = 632.8$ [nm], 128-by-128 pupil samples, $\delta(n) = \frac{2\pi dn}{\lambda}$, $I'(x, y) = 2 + \sin[20\pi(x + y)]$, $I''(x, y) = 1$, $\alpha(n) = \frac{2\pi n}{\lambda} * 50 \times 10^{-9}$, and $\beta(n) = \frac{-2\pi n}{\lambda} * 25 \times 10^{-9}$.

We confirm that the subblock size does affect the accuracy of the OPD map. This is also seen in Table 4.1 where the fitted Zernike polynomials coefficients for each algorithm are presented.

Aberration name	Least-squares [λ]	SSPCA		
		16-by-16 [λ]	8-by-8 [λ]	4-by-4 [λ]
$Z_0(\rho, \theta)$	-0.23	-0.20	-0.20	-0.16
$Z_1(\rho, \theta)$	0.17	0.09	0.01	0.32
$Z_2(\rho, \theta)$	-0.15	0.03	-0.02	-0.70
$Z_3(\rho, \theta)$	0.01	-0.01	-0.01	0.02
$Z_4(\rho, \theta)$	0.02	-0.01	-0.01	0.18
$Z_5(\rho, \theta)$	-0.09	-0.06	-0.06	-0.28
$Z_6(\rho, \theta)$	-0.27	-0.28	-0.28	-0.24
$Z_7(\rho, \theta)$	-0.01	0.01	0.01	-0.19
$Z_8(\rho, \theta)$	0.50	0.48	0.48	0.46
$Z_9(\rho, \theta)$	0.03	0.04	0.05	-0.05
$Z_{10}(\rho, \theta)$	-0.05	-0.02	-0.02	-0.26
$Z_{11}(\rho, \theta)$	-0.02	0.00	0.00	-0.06
$Z_{12}(\rho, \theta)$	0.95	0.98	0.98	0.55
$Z_{13}(\rho, \theta)$	0.03	0.02	0.02	-0.02
$Z_{14}(\rho, \theta)$	-0.01	0.01	0.01	-0.04
$Z_{15}(\rho, \theta)$	0.00	-0.02	-0.02	-0.08
$Z_{16}(\rho, \theta)$	-0.06	-0.04	-0.04	-0.07
$Z_{17}(\rho, \theta)$	-0.01	0.00	0.00	0.04
$Z_{18}(\rho, \theta)$	-0.04	-0.01	-0.01	-0.14
$Z_{19}(\rho, \theta)$	0.01	0.02	0.02	-0.26
$Z_{20}(\rho, \theta)$	-0.02	0.00	0.00	-0.05
$Z_{21}(\rho, \theta)$	-0.04	-0.02	-0.02	-0.15
$Z_{22}(\rho, \theta)$	0.03	0.02	0.02	-0.02
$Z_{23}(\rho, \theta)$	0.00	0.01	0.01	0.04
$Z_{24}(\rho, \theta)$	0.00	-0.02	-0.02	-0.04

Table 4.1: Zernike polynomial coefficients recovered from a series of simulated interferograms using different PSI algorithms. We notice that the SSPCA algorithm does not always retrieves the correct phase sign due the arbitrary assignment of sine and cosine properties to its principal components and that a subblock size that yields the least error must be determined. Please refer to Table 3.1 for aberration descriptions.

4.5. PSI SIMULATIONS

Test name	Least-squares [λ]	SSPCA		
		16-by-16 [λ]	8-by-8 [λ]	4-by-4 [λ]
Recovered OPD RMS error	0.1108	0.0513	0.0453	0.9713
Reconstructed OPD RMS error	0.1000	0.0453	0.0384	0.9036
Recovered OPD without first 4 Zernike coef- ficients RMS error	0.0190	0.0082	0.0083	0.4253

Table 4.2: RMS error between our test OPD and the recovered and reconstructed OPD. the SSPCA algorithm can yield recovered OPD surfaces with an RMS error against the original surface less than 0.01 [λ] if we disregard the first four terms of the Zernike polynomial coefficients and select a suitable subblock size.

From Table 4.1 we appreciate that there are non-zero horizontal and vertical tilt coefficient values when fitting Zernike polynomial coefficients to the recovered OPD maps using both algorithms; that a proper selection of subblock size must be done to avoid under and oversampling of the interferogram frames in order to reduce errors like the ones seen in the 4-by-4 subblock SSPCA test and that there are slight deviations from our expected Zernike coefficient values and the ones recovered from the PSI algorithms, no larger than 0.05 [λ]. The recovered and reconstructed OPD maps are shown in Figure 4.3.

To analyse how well the least-squares and SSPCA algorithms perform we calculated the Root Mean Square error between the retrieved OPD surfaces and our original OPD surface. We calculate the Root Mean Square error between the values of the original and retrieved OPD surfaces. We will refer as "recovered" to the retrieved OPD surface from any of the algorithms and as "reconstructed" the OPD surface generated from the fitted Zernike polynomials coefficients. The results are presented in Table 4.2, from where we conclude that the SSPCA algorithm can yield recovered OPD surfaces with an RMS error against the original surface less than 0.01 [λ] if we disregard the first four terms of the Zernike polynomial coefficients and select a suitable subblock size. The subblock size should be calibrated for the usual operation conditions in the laboratory.

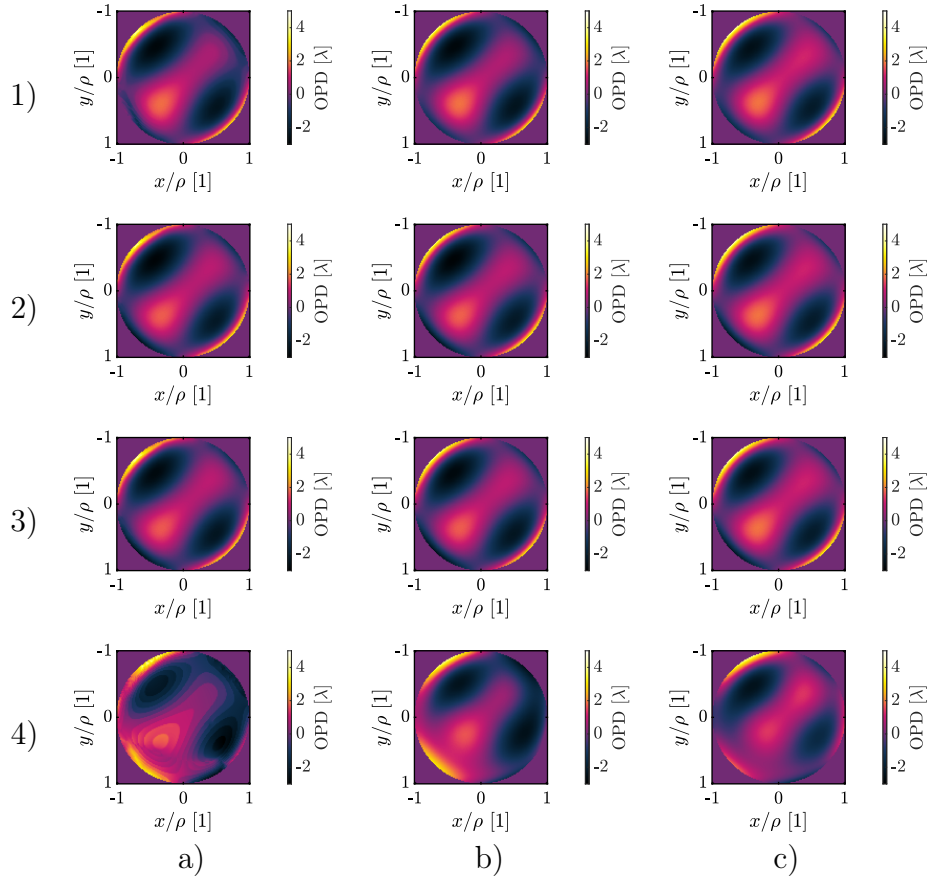


Figure 4.3: Recovered and reconstructed OPD maps using the least-squares and SSPCA algorithms for a normalized pupil. Row 1) is the least-squares result; rows 2), 3), 4) depict the recovered OPD maps using the SSPCA algorithm with subblocks of size 16-by-16, 8-by-8 and 4-by-4. Column a) represents the recovered OPD map from every algorithm; column b) is the OPD surface generated by the fitted Zernike polynomial coefficients and column c) is the generated OPD surface when omitting piston, tilt and defocus terms.

4.6 Experimental measurements

Two interferogram series were obtained from the in-house Fizeau interferometer located at the *LUFABEO* on the Institute of Applied Science and Technology and we tested the phase retrieval repeatability of the linear least-squares and the SSPCA algorithms. The analysed optical component was a spherical reflective surface under the following test conditions:

- CW laser centered at $\lambda_0 = 632.8$ [nm];
- 10 interferograms with 10.0 [μm] displacement between each interferogram, 2 sequences, since the Fizeau interferometer reference surface is moving towards the fixed test surface, we will consider the steps to have a negative sign, i. e, [0.0, -10.0, -20.0, ..., -100.0] [μm]; and
- photography size of 1280-by-1024 pixels, downsampled to 128-by-128 pixels.

On Figure 4.4 we show the first four frames of both sequences. We notice that there are fringes that are independent on the phase shift between each frame. We applied the least-squares and SSPCA PSI algorithms to both sequences to retrieve their phase $\Theta(x, y)$, fit a Zernike polynomial and rebuild their respective OPD surfaces with and without the first four terms of the Zernike polynomial expansion.

We calculated the RMS error between the recovered and reconstructed OPD maps from Test a) and Test b) and these values are displayed on Table 4.3 were we appreciate that the SSPCA algorithm provides a RMS error less than 500×10^{-6} [λ] when we disregard the piston, tilt and defocus terms from the fitted Zernike polynomial expansion; while the least-squares PSI algorithm has an RMS error greater than 100×10^{-3} [λ] between tests. We conclude that the SSPCA algorithm allows us to perform repeatable measurements.

On Figures 4.5 and 4.6 we show the recovered and reconstructed OPD surfaces using the least-squares and the SSPCA with 8-by-8 pixel subblocks algorithms respectively.

Test name	Least-squares [λ]	SSPCA		
		16-by-16 [λ]	8-by-8 [λ]	4-by-4 [λ]
Recovered experimental OPD RMS error	0.4103	0.0219	0.0173	0.0093
Reconstructed experimental OPD RMS error	0.3887	0.0210	0.0164	0.0084
Recovered experimental OPD without first 4 Zernike coefficients RMS error	0.0133	0.0003	0.0003	0.0005

Table 4.3: RMS error between the measured OPD surfaces of the two tests under different comparison conditions. When removing the piston, tilt and defocus terms from the fitted Zernike polynomial we find out that the SSPCA algorithm yields a variation of 0.0005 [λ] after analysing two sets of interferograms of the same test surface.

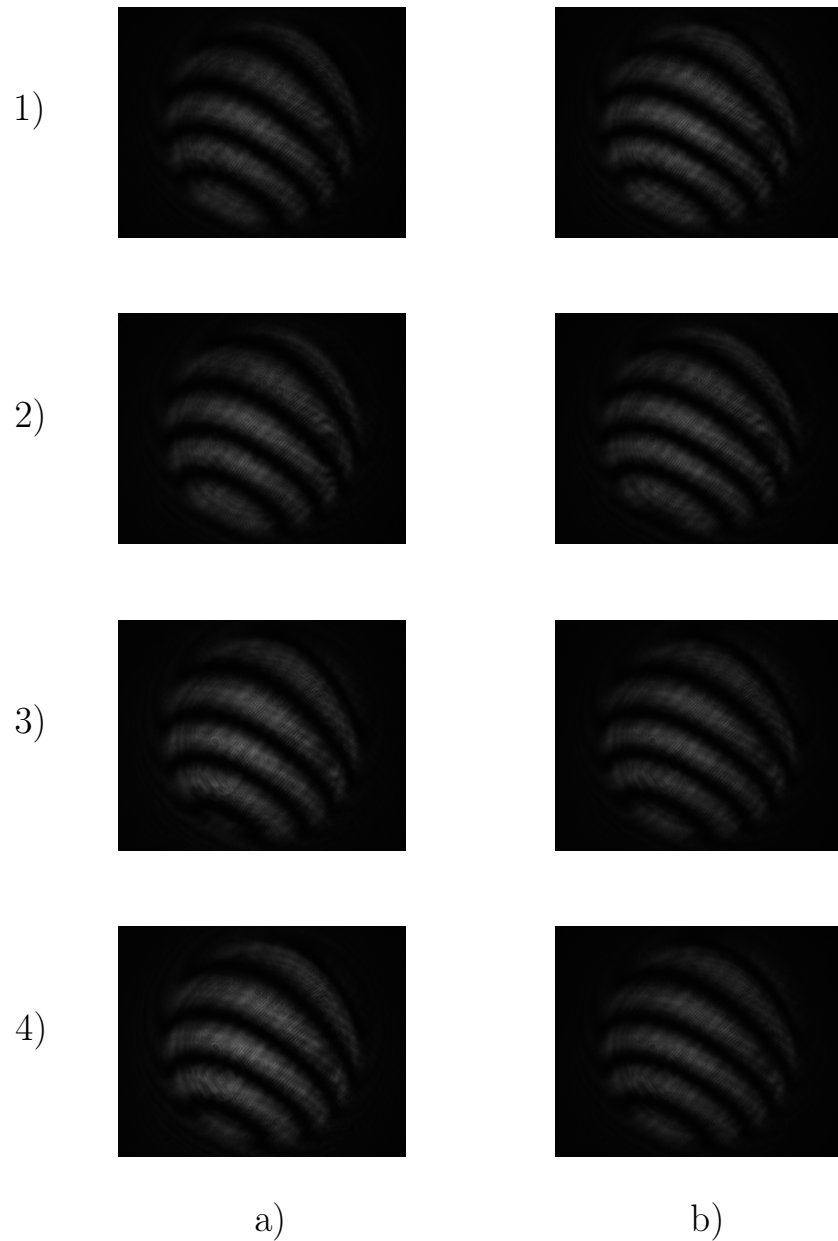


Figure 4.4: First four frames from the measured sequences a) and b). The optical component analysed was a reflective spherical surface. We appreciate that there are fringes that seems to be independent of the phase-shift between snapshots.

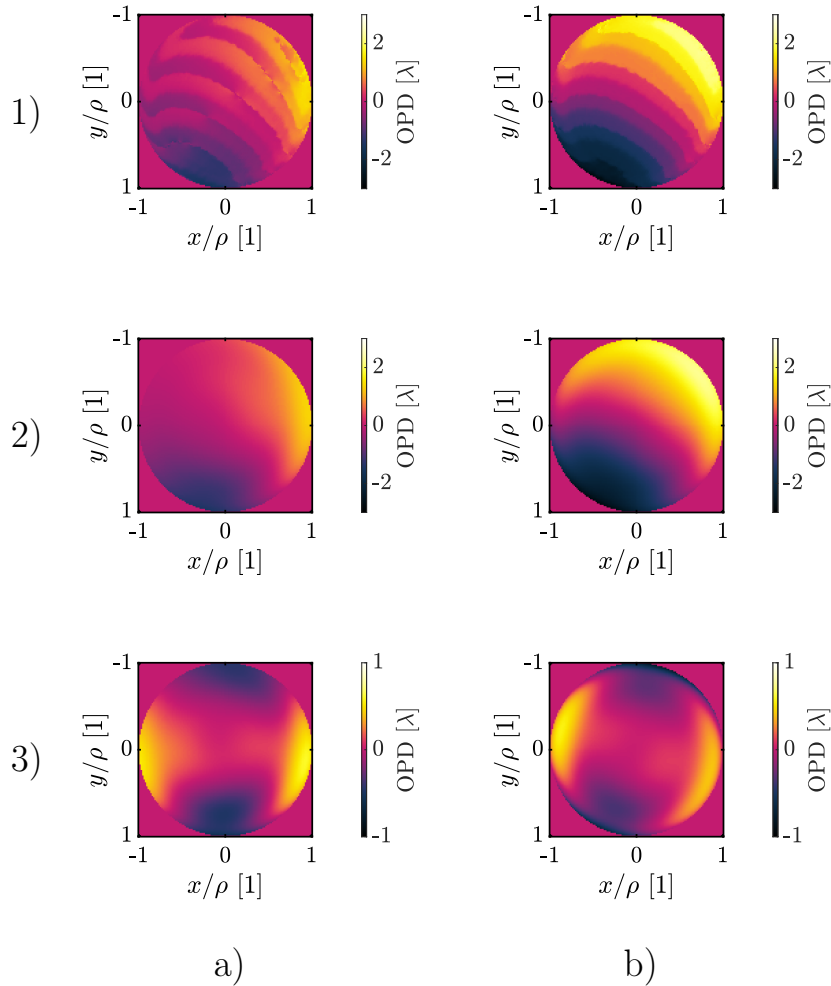


Figure 4.5: Recovered and reconstructed OPD maps using the least-squares PSI algorithm on test a) and b). Row 1) is the recovered OPD surface from the PSI algorithm; row 2) is the reconstructed OPD surface from the fitted Zernike polynomial coefficients and row 3) is the reconstructed OPD surface when we omit the first four Zernike polynomial coefficients. We notice that there are visual differences between the OPD surfaces from both tests. The pupil dimensions were normalized against $\rho = 64$ [pixels].

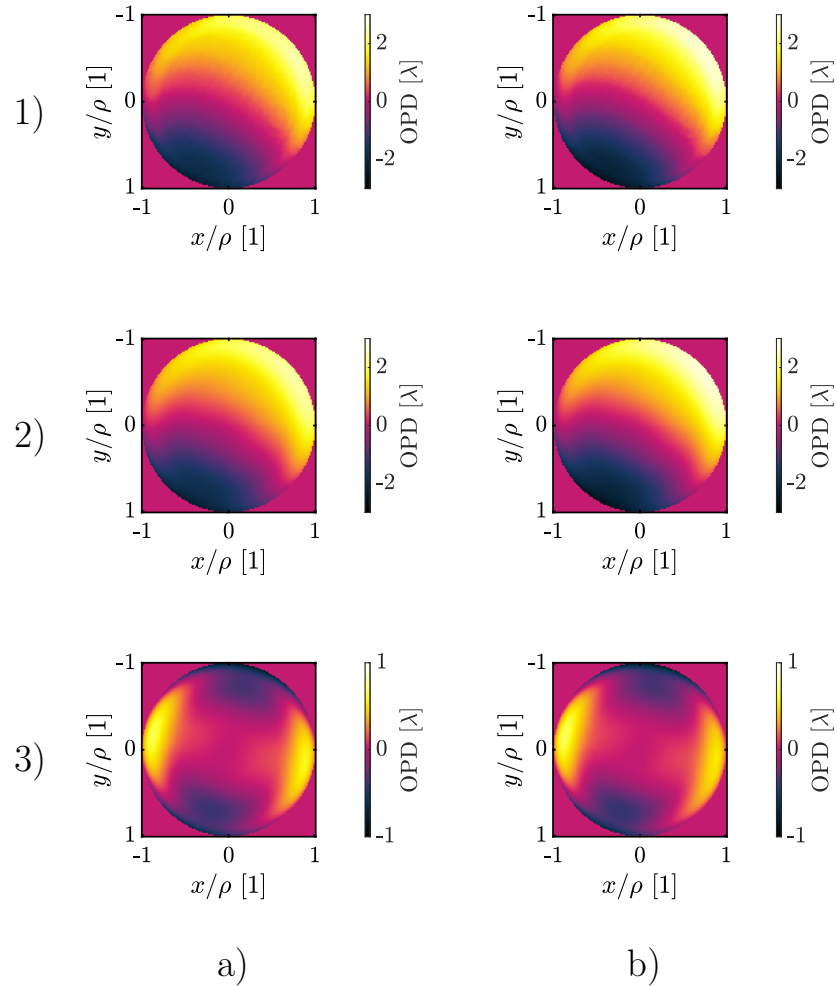


Figure 4.6: Recovered and reconstructed OPD maps using the SSPCA PSI algorithm with a 8-by-8 subblock size on test a) and b). Row 1) is the recovered OPD surface from the PSI algorithm; row 2) is the reconstructed OPD surface from the fitted Zernike polynomial coefficients and row 3) is the reconstructed OPD surface when we omit the first four Zernike polynomial coefficients. We notice that the OPD maps on row 3) are quite similar, in agreement with Table 4.3. The pupil dimensions were normalized against $\rho = 64$ [pixels].

To study how the results from test a) and test b) deviate from each other, we present the fitted Zernike polynomial coefficients in Table 4.4, where we can appreciate that the least-squares PSI algorithm has a large difference on the third-order astigmatism coefficients which explains the visual difference on Figure 4.5's 3a) and 3b) images, which are the reconstructed OPD surfaces from the fitted Zernike polynomial coefficients when discarding the non-aberration terms. This difference is not present when employing the SSPCA algorithm, hence, the author recommends using this method for further experimental measurements.

4.7 Summary

We presented the principles of operation of *Phase Shifting Interferometry*, we discussed the least-squares and the SSPCA algorithms and we studied their performance with simulated and experimental interferograms.

We conclude that the SSPCA algorithm is best suitable for experimental measurements given its ability to provide repeatable measurements, however its main limitation is determining the true phase sign of the measurement.

4.7. SUMMARY

Aberration name	Least-squares [λ]		SSPCA 8-by-8 [λ]	
	Test a)	Test b)	Test a)	Test b)
$Z_0(\rho, \theta)$	-0.01	0.04	0.33	0.33
$Z_1(\rho, \theta)$	-0.40	-1.04	-1.00	-1.11
$Z_2(\rho, \theta)$	0.39	0.60	0.53	0.62
$Z_3(\rho, \theta)$	0.01	0.14	0.14	0.14
$Z_4(\rho, \theta)$	-0.23	-0.17	-0.22	-0.22
$Z_5(\rho, \theta)$	0.02	0.12	0.11	0.11
$Z_6(\rho, \theta)$	0.03	0.02	0.02	0.02
$Z_7(\rho, \theta)$	0.02	-0.01	0.00	0.00
$Z_8(\rho, \theta)$	0.03	-0.01	-0.01	-0.01
$Z_9(\rho, \theta)$	-0.04	0.02	0.01	0.02
$Z_{10}(\rho, \theta)$	-0.01	0.03	0.01	0.02
$Z_{11}(\rho, \theta)$	0.02	0.01	0.02	0.02
$Z_{12}(\rho, \theta)$	0.00	0.00	-0.01	-0.02
$Z_{13}(\rho, \theta)$	0.00	0.01	0.01	0.01
$Z_{14}(\rho, \theta)$	0.00	0.00	0.01	0.01
$Z_{15}(\rho, \theta)$	-0.01	-0.05	-0.06	-0.06
$Z_{16}(\rho, \theta)$	0.00	0.00	0.01	0.01
$Z_{17}(\rho, \theta)$	0.01	0.01	0.00	0.01
$Z_{18}(\rho, \theta)$	0.01	-0.01	0.00	0.00
$Z_{19}(\rho, \theta)$	0.01	0.00	0.00	0.00
$Z_{20}(\rho, \theta)$	0.00	0.01	0.02	0.02
$Z_{21}(\rho, \theta)$	-0.01	0.01	0.00	0.00
$Z_{22}(\rho, \theta)$	-0.02	0.00	0.00	0.00
$Z_{23}(\rho, \theta)$	-0.01	0.00	0.00	0.00
$Z_{24}(\rho, \theta)$	-0.02	-0.03	-0.04	-0.04

Table 4.4: Experimental measurement Zernike coefficient comparison using the least-squares and the SSPCA approach with a 8-by-8 subblock size. When discarding the first four Zernike polynomial coefficients the largest differences found are in the 3rd order astigmatism $Z_4(\rho, \theta)$ and $Z_5(\rho, \theta)$ when using the least-squares PSI algorithm. This is not the case for the SSPCA algorithm. Please refer to Table 3.1 for aberration descriptions.

Chapter 5

Impact of frequency-dependent spherical aberrations in the focusing of ultrashort pulses

The focusing of ultrashort laser pulses is of great interest for applications like nonlinear microscopy [2–4], micromachining [5], medicine [6] and fundamental science [7–9].

When propagating an ultrashort laser pulse through refractive media, it will be subjected to *dispersion*. Dispersion is one of the phenomena that impacts the pulse duration the most. The use of pulse compressors and achromatic lenses reduce this phenomenon. These phenomena depends on pulse constituent frequencies.

A simulation technique based on raytracing and wave optical propagation was developed by Fuchs, et. al. [16], including dispersive effects such as *Group Velocity Dispersion* [13, 14] and *Propagation Time Difference* [10–14]. However, in a laboratory setting these effects can be pre-compensated with pulse compressors and achromatic doublets.

We simulate the focusing of ultrashort laser pulses with different initial pulse durations and calculate the spatial and temporal intensity distributions around the focal point of a given system. We will discuss the scalar diffraction theory and how to integrate the OPD calculations reviewed in Chapter 2.

We will analyse the calculated intensity profiles and simulate pulse characterization techniques used in the laboratory.

5.1 Theory

An imaging system transforms a diverging spherical wavefront that emanates from a point source in the entrance plane into a converging spherical wavefront with center in the Gaussian image point. All the geometrical rays converge in the optical system back focal point. The number of converging rays into the image point is infinite, thus, the focused intensity is infinite in said point while having zero intensity anywhere else, however this does not reflect reality, meaning that the geometrical optics theory is invalid to calculate fields in the vicinity of the focal region of the system [53]. Diffraction theory is used to calculate the energy distribution around the image point.

Although an optical system can be analysed by using diffraction theory only, it is not recommended to do so for complex systems since it would be an inefficient computation.

By combining raytracing and diffraction theories, the raytracing is used to calculate the wavefront that propagates from the object plane through the optical system up to the exit pupil of the optical system [53].

Raytracing and *OPD* calculations yield the deviation of the emerging wavefront from a spherical wavefront centered at the system's Gaussian image point, afterwards, the scalar diffraction theory can be used to calculate the field from the exit pupil to the desired observation plane.

5.1.1 Scalar diffraction theory

Scalar diffraction theory is used to study ultrashort pulse propagation in an optical system where the pulse frequency modulation and phase changes caused by dispersion, diffraction and aberrations are modelled. The aberration phase change is determined by calculating the optical path difference contributed by each optical surface in the system for each frequency component of the pulse. [16, 53]

To perform wave propagation in a dielectric medium under scalar diffraction theory the following conditions are required:

- Field quantities from different sources can be added, or linear;
- the electric field is described as a scalar function, i.e., it is neglected the vectorial nature of light.
- non-magnetic, i. e. the medium permeability is equal to the vacuum magnetic permeability μ_0 .

Rayleigh-Sommerfeld diffraction integral

Consider the propagation of monochromatic light from a two-dimensional source plane of coordinates (x_1, y_1) . An area A defines the extent of the source or illuminated aperture. The source field distribution is given by $U_1(x_1, y_1)$ and

the field distribution at a distant observation plane ($U_2(x_2, y_2)$) can be calculated by the first Rayleigh-Sommerfeld diffraction integral, which is displayed in Equation (5.1):

$$U_2(x_2, y_2) = \frac{z}{i\lambda} \iint_A U_1(x_1, y_1) \exp(ikr_{12}) dx_1 dy_1, \quad (5.1)$$

where

- λ is the light wavelength;
- k is the wavenumber, defined as $2\pi/\lambda$;
- z is the distance between the reference systems for the source and observation planes.
- r_{12} is the distance between the points (x_1, y_1) and (x_2, y_2) , as shown in Equation (5.2).

$$r_{12} = \sqrt{z^2 + (x_2 - x_1)^2 + (y_2 - y_1)^2} \quad (5.2)$$

The system described by Equation (5.1) is presented in Figure 5.1.

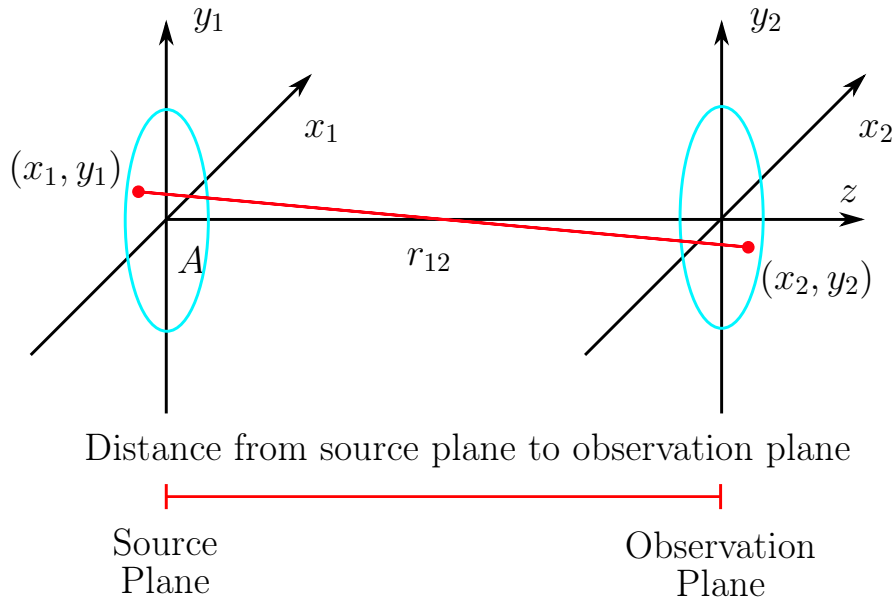


Figure 5.1: Monochromatic light propagation from the source plane of area A to the observation plane.

5.1. THEORY

Equation (5.1) is a representation of the Huygens-Fresnel principle. It is assumed that the source acts as an infinite collection of punctual sources, each one generating a spherical wavefront associated with the source field in the (x_1, y_2) position. Each spherical wavefront contribution is summed as seen from a (x_2, y_2) point in the observation plane allowing interference to occur.

Fresnel diffraction integral

The use of Equation (5.2) to calculate the field $U_2(x_2, y_2)$ will increase the computation time for the diffraction calculation. In order to improve the computation time consider the binomial expansion

$$\sqrt{1+b} = 1 + \frac{1}{2}b - \frac{1}{8}b^2 + \dots \quad (5.3)$$

where $b < 1$. Expanding Equation (5.2) using Equation (5.3) and preserving the first two terms only, we get

$$z \left[1 + \frac{1}{2} \left(\frac{x_2 - x_1}{z} \right)^2 + \frac{1}{2} \left(\frac{y_2 - y_1}{z} \right)^2 \right]. \quad (5.4)$$

Substituting Equation (5.4) in the exponential term in Equation (5.1) is akin to assume parabolic radiation, instead of spherical, emerges from the punctual sources [54]. If we consider that $r_{12} \approx z$, we arrive to the Fresnel diffraction integral, as presented in Equation 5.5:

$$U_2(x_2, y_2) = \iint_A U_1(x_1, y_1) \exp \left\{ -i \frac{k}{2z} \left[(x_2 - x_1)^2 + (y_2 - y_1)^2 \right] \right\} dx_1 dy_1 \quad (5.5)$$

5.1.2 Ultrashort pulse modelling

Ultrashort pulses are electromagnetic wave packets and they are described in its entirety by its spatial and temporal dependent electrical field. The difference between monochromatic light and pulsed light is that a pulse consists of a few optical cycles of a sine wave. The pulse field in the frequency domain of an ultrashort laser pulse can be described as [29]

$$\tilde{E}(\omega - \omega_0) = \sqrt{S(\omega - \omega_0)} \exp[-i\phi(\omega - \omega_0)], \quad (5.6)$$

where ω_0 is the carrier angular frequency of the pulse, $S(\omega - \omega_0)$ is the spectrum and $\phi(\omega - \omega_0)$ is the spectral phase.

We calculate the Inverse Fourier Transform of the pulse field in the frequency domain to obtain the complex field amplitude in time $e(t)$:

$$e(t) = \mathcal{F}^{-1}\{\tilde{E}(\omega - \omega_0)\}. \quad (5.7)$$

Finally, the pulse intensity distribution in the time domain $I(t)$ is given by

$$I(t) = |e(t)|^2. \quad (5.8)$$

The pulse duration τ_p is defined as the *Full Width at Half Maximum* (FWHM) of the pulse intensity $I(t)$, and the spectral width $\Delta\omega_p$ as the FWHM of the spectrum $S(\omega)$.

The bandwidth $\Delta\omega_p$ and pulse duration τ_p follow the minimum duration-bandwidth product shown in Equation (5.9) since the pulse temporal and spatial properties are related via the Fourier transform, where c_B is a constant that depends on the pulse shape [1].

$$\Delta\omega_p\tau_p \geq 2\pi c_B, \quad (5.9)$$

The equality in Equation (5.9) holds for pulses where its instantaneous frequency is not dependent on time [1, 55] and we will reference it as a *bandwidth limited pulse*. For a Gaussian modulated bandwidth limited pulse, the constant in Equation (5.9) is $c_B = 0.441$ [1].

Spectrum as a function of wavelength and frequency

Spectrometers measure the spectral intensity as a function of wavelength, $S(\lambda)$, so in order to calculate the pulse intensity in the time domain, $I(t)$, the spectral intensity $S(\lambda)$ has to be transformed into the spectrum in frequency, $S(\omega)$. This wavelength-frequency transform is given by [29]:

$$S(\lambda) = S(\omega) \frac{2\pi c}{\lambda^2}. \quad (5.10)$$

where c is the speed of light in vacuum, λ is the wavelength and its related to frequency via $\lambda = 2\pi c/\omega$.

Gaussian pulse frequency modulation

As previously stated, an ultrashort pulse is constituted of several frequencies around a carrier wavelength. A Gaussian-modulated, bandwidth limited pulse will have its electric field in the frequency domain defined as shown in Equation (5.11):

$$A(\omega) = \sqrt{S(\omega)} = \exp \left[- \left(\frac{\tau_0 \Delta\omega}{2\sqrt{2 \ln 2}} \right)^2 \right], \quad (5.11)$$

where

- τ_0 is the FWHM pulse duration and
- $\Delta\omega$ is the difference between the pulse frequencies and the carrier frequency, $\omega - \Delta\omega$.

5.1. THEORY

Equation (5.11) considers that the pulse instantaneous frequency is not dependent on time, in other words, it has no chirp at the moment it enters the optical system to be analysed. The spectral intensity for 100 [fs], 50 [fs] and 5 [fs] pulses following Equation 5.11 are shown in Figure 5.2.

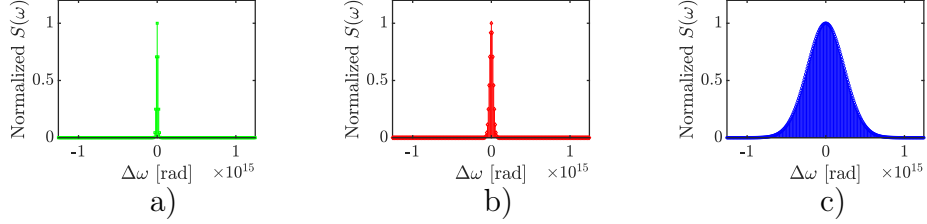


Figure 5.2: Spectral intensity $S(\omega)$ for a) 100 [fs], b) 50 [fs], and c) 5 [fs] pulses with a carrier wavelength $\lambda_0 = 810$ [nm].

Pulse frequencies in terms of carrier frequency

The different frequencies of a pulse, ω , can be written in terms of the carrier frequency ω_0 as follows:

$$\omega = \omega_0 + \Delta\omega. \quad (5.12a)$$

Dividing by the speed of light in vacuum c ,

$$\frac{\omega}{c} = \frac{\omega_0}{c} + \frac{\Delta\omega}{c}. \quad (5.12b)$$

Since the wavenumber k is defined as

$$k = \frac{\omega}{c}, \quad (5.12c)$$

then

$$k = k_0 + \frac{\Delta\omega}{c}, \quad (5.12d)$$

$$k = k_0 + \frac{\Delta\omega\omega_0}{c\omega_0}, \quad (5.12e)$$

$$k = k_0 + k_0 \frac{\Delta\omega}{\omega_0}, \quad (5.12f)$$

$$k = k_0 \left(1 + \frac{\Delta\omega}{\omega_0} \right). \quad (5.12g)$$

This notation will be helpful to calculate the electric field at the exit pupil and the resulting field at the observation plane according to Equation (5.5).

5.1.3 Propagation of a femtosecond pulse through a non-dispersive system.

Equation (5.13) describes the electric field in the frequency domain of an unchirped, Gaussian-modulated in frequency pulse around the focal plane of a non-dispersive, aberrated optical system [56]:

$$U(x_2, y_2, z, \Delta\omega) = \iint_{-\infty}^{\infty} dx_1 dy_1 U_0(x_1, y_1) P(x_1, y_1) A(\Delta\omega) \left(-\frac{i \exp(ikz)}{\lambda z}\right) \times \exp[-i\Theta(x_1, y_1, \Delta\omega)] \exp[-i\phi(x_1, y_1, \Delta\omega)] \exp\left\{-i\frac{k}{2z}[(x_2 - x_1)^2 + (y_2 - y_1)^2]\right\}, \quad (5.13)$$

where

- (x_1, y_1) represents the Cartesian coordinates of the exit pupil;
- (x_2, y_2) , the Cartesian coordinates of the observation plane as shown in Figure 5.3;
- z , the distance between the exit pupil and the observation plane;
- U_0 , the input electrical plane wave which is uniform over the input plane;
- $P(x_1, y_1)$ is the pupil function defined as one within the pupil radius and zero elsewhere;
- $A(\Delta\omega)$ is the pulse Gaussian-modulation frequency defined in Equation (5.11);
- $\Theta(x_1, y_1, \Delta\omega)$ is the phase change due to aberrations;
- $\phi(x_1, y_1, \Delta\omega)$ is the phase change due to the transformation of a plane wavefront into a converging spherical wave;
- k is the wavenumber of the pulse frequencies which can be expressed as $k = k_0(1 + \Delta\omega/\omega_0)$;
- $\Delta\omega$ is the difference between any of the pulse frequencies and the pulse carrier frequency; and
- λ are the wavelengths in vacuum corresponding to each pulse frequency.

To obtain the pulse electric field in the time domain we calculate the Fourier transform of Equation (5.13):

$$U(x_2, y_2, z, t) = \int_{-\infty}^{\infty} U(x_2, y_2, z, \Delta\omega) \exp(-i\Delta\omega t) d\Delta\omega. \quad (5.14)$$

Finally, the spatial and time intensity profiles are defined as:

$$I(x_2, y_2) \propto \int_{-\infty}^{\infty} |U(x_2, y_2, z, t)|^2 dt, \quad (5.15)$$

and

$$I(t) \propto \int_{-\infty}^{\infty} \int_{-\infty}^{\infty} |U(x_2, y_2, z, t)|^2 dx_2 dy_2. \quad (5.16)$$

The FFT method proposed by Anaya-Vera, et.al. [57] was used to compute Equation (5.13) numerically, allowing us to do a fast and accurate calculation of the pulse electric field.

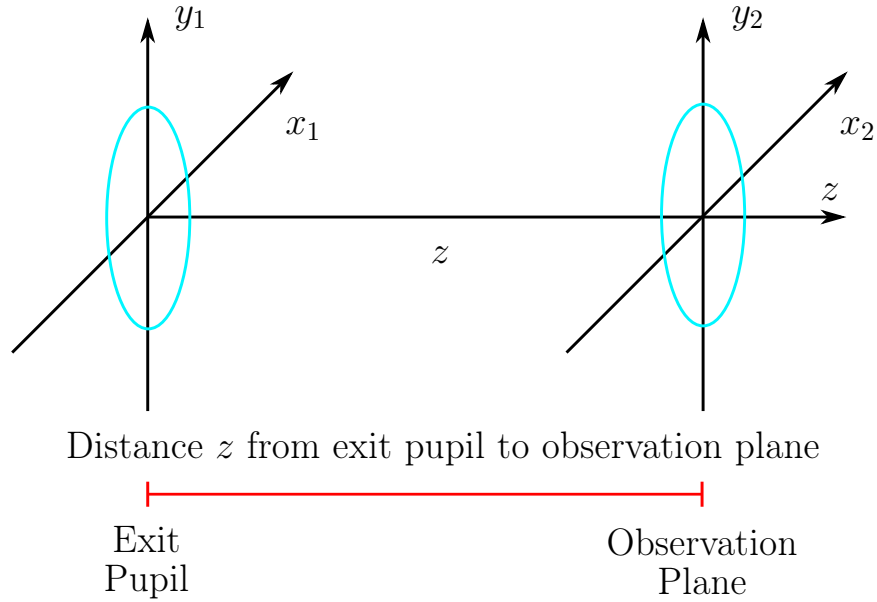


Figure 5.3: Optical system coordinates used for the exit pupil and the observation plane located around the system focal point.

Frequency-dependent aberration calculations

In order to compute $\Theta(x_1, y_1, \Delta\omega)$ for Equation (5.13), we require to perform a raytracing calculation for every pulse frequency.

The wavelengths λ that make up the pulse are calculated from the angular frequency vector $\Delta\omega$ as shown in Equation (5.17):

$$\lambda(\Delta\omega) = \frac{2\pi}{k_0 \left(1 + \frac{\Delta\omega}{\omega_0}\right)} \quad (5.17)$$

To calculate the refractive index we use Sellmeier's Equation shown in Equation (5.18) [58] for every wavelength that comprises the pulse:

$$n(\lambda) = \sqrt{1 + \frac{B_1\lambda^2}{\lambda^2 - C_1} + \frac{B_2\lambda^2}{\lambda^2 - C_2} + \frac{B_3\lambda^2}{\lambda^2 - C_3}} \quad (5.18)$$

Once we calculate the *OPD* for every frequency, we evaluate Equation (5.19),

$$\Theta(x_1, y_1, \Delta\omega) = k_0 \left(1 + \frac{\Delta\omega}{\omega_0}\right) \lambda(\Delta\omega) \text{OPD}[x_1, y_1, \lambda(\Delta\omega)], \quad (5.19)$$

and use this result into Equation (5.13).

5.1.4 Intensity profile measurement

To locate the position of the smallest spot size and the shortest pulse duration we require to measure width of the spatial and temporal intensity profiles. To this date, there is no single standard criterion to estimate pulse duration and spot sizes due the variability of the measured spatial and temporal intensity profiles. Another issue is that different widths can be achieved depending on the measurement criteria, they can be dependent on the beam shape and there is no universal conversion factors between these results [59].

In this work, we study two measurement criteria: the FWHM and the standard deviation of the intensity distributions. We measure the intensity profiles calculated by Equations (5.15) and (5.16) using these criteria. Also, we modelled two techniques used in the laboratory to perform pulse intensity distribution measurements: the knife-edge tests which measures the spot size and the intensity autocorrelation which estimates the pulse duration. The obtained space and time intensity profiles recovered from these techniques are measured using the FWHM and standard deviation criteria.

Standard deviation of a distribution

Since we consider that the optical system has rotational symmetry and the rays propagate parallel to the optical axis, we only present results for the x-axis.

To calculate the standard deviation of a given distribution, the square-root of the second order central moment is calculated [1]. The standard deviation definition σ_x of a distribution $f(x)$ along the x variable is presented in Eq. (5.20):

$$\sigma_x = \sqrt{\frac{\int_{-\infty}^{\infty} x^2 |f(x)|^2 dx}{\int_{-\infty}^{\infty} |f(x)|^2 dx}} \quad (5.20)$$

If the measured distribution is a Gaussian distribution, we can estimate its FWHM, τ_{σ_x} , from the standard deviation with the following relation [1]:

$$\tau_{\sigma_x} = 2\sqrt{2 \ln 2} \sigma_x \quad (5.21)$$

Knife-edge test

The knife-edge test is simulated to estimate the spot size of the focused pulse beam. By moving the knife-edge along the x_2 axis, the power received by the detector is given by Equation (5.22) [60]:

$$P(x_2) = \int_{-\infty}^{\infty} \int_{-\infty}^{x_2} I(x, y_2) dx dy_2, \quad (5.22)$$

where the opaque zone is in the semi-plane $x > x_2$. By taking the derivative of $P(x_2)$, we have a pulse spatial profile, $I_{KE}(x_2)$, in other words,

$$I_{KE}(x_2) = dP(x_2)/dx_2. \quad (5.23)$$

The width of the intensity distribution in space can be measured directly from the spatial intensity profile, $I(x_2, y_2)$, given by Equation (5.15) using the FWHM criterion or by calculating its standard deviation, σ_x . Alternatively, the width of the intensity distribution in space can also be measured from the intensity profile, $I_{KE}(x_2)$, given by Equation (5.23) and using the FWHM criterion or by calculating its standard deviation σ_{KE} .

Intensity autocorrelation

The intensity autocorrelation, $A^{(2)}(\tau)$, is defined as

$$A^{(2)}(\tau) \equiv \int_{-\infty}^{\infty} I(t)I(t - \tau)dt. \quad (5.24)$$

where $I(t)$ is the time intensity distribution given by Equation (5.16) and τ is the delay.

The width of the time intensity profile, $I(t)$, given by Equation (5.16) can be measured directly by calculating its standard deviation, σ_t . Alternatively, the width of the time intensity profile can also be estimated from the intensity autocorrelation, $A^{(2)}(\tau)$ including the $\sqrt{2}$ deconvolution factor, and then evaluating the standard deviation, σ_{A^2} , which already includes the $\sqrt{2}$ deconvolution factor. To fully characterize a pulse, its intensity and phase must be measured.

5.2 Simulations

We simulated the focusing of femtosecond pulses through a concave mirror, a commercial achromatic doublet and a commercial double-convex lens; the commercial components are from Edmund Optics. We present the parameters of these systems in Table 5.1. The three systems have the same diameter $D = 12.0$ [mm] and the same effective focal length $EFL = 30.0$ [mm], thus, all of them have the same numerical aperture $NA = 0.2$.

The simulated input pulse duration τ_0 ranges from 5 to 100 [fs] with a carrier wavelength $\lambda_0 = 810$ [nm], which corresponds to a Ti:Sapphire femtosecond

System	Material	CT_1 [mm]	CT_2 [mm]	R_1 [mm]	R_2 [mm]	R_3 [mm]
Concave mirror	-	-	-	-60.0	-	-
Achromatic doublet	N-LAK22 / N-SF6	4.5	2.5	17.77	-16.46	-136.8
single lens	N-BK7	3.7	-	30.36	-30.36	-

Table 5.1: Optical system parameters used in the simulations. All components have a diameter $D = 12.0$ [mm] and effective focal length $EFL = 30.0$ [mm]

laser. We will investigate the effect of aberrations, which are dependent on the frequencies that comprise the pulse.

To visualize the aberrations for each optical system presented in Table 5.1 we calculate the OPD at the exit pupil of the system for the carrier wavelength $\lambda_0 = 810$ [nm], and then convert it into a fringe pattern $I_f(x_1, y_1, \lambda_0)$ using Equation (5.25):

$$I_f(x_1, y_1, \lambda_0) = 1 + \cos [2\pi OPD(x_1, y_1, \lambda_0)]. \quad (5.25)$$

In Figure 5.4 the interference fringe patterns calculated with Equation (5.25) are presented for the three optical systems in Table 5.1. We can see more fringes in the interferogram for the single lens in Figure 5.4(c), fewer fringes for the spherical concave mirror in Figure 5.4(a), and even fewer fringes for the achromatic doublet in Figure 5.4(b). These results are expected since the achromatic doublet is the only system with primary spherical aberration correction.

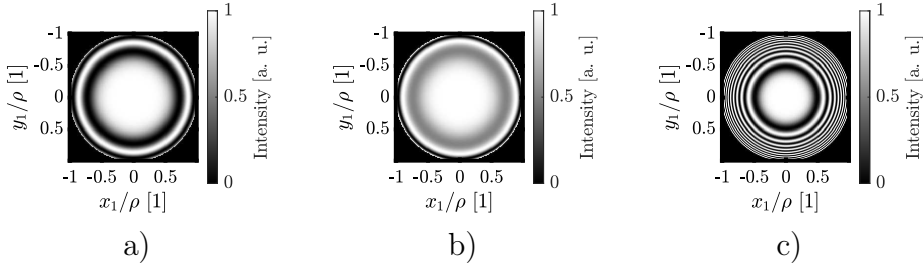


Figure 5.4: Fringe patterns calculated with Equation (5.25) for the systems presented in Table 5.1. a) concave spherical mirror; b) achromatic doublet; and c) single lens. All the systems have a numerical aperture of $NA=0.2$. The wavelength is $\lambda_0 = 810$ [nm] and a diameter $D = 12.0$ [mm]. The pupil was normalized against the system radius $\rho = D/2$.

In our simulation we considered the phase change due to aberrations $\Theta(x_1, y_1)$ under the following three cases:

- $\Theta(x_1, y_1, \omega) = 0$, which corresponds to the aberration-free case;
- $\Theta(x_1, y_1, \omega) = \frac{2\pi ck_0}{\omega_0} OPD(x_1, y_1, \omega_0)$, which evaluates the spherical aberration introduced by the carrier frequency and it will be referred as the

5.2. SIMULATIONS

carrier frequency case and;

- $\Theta(x_1, y_1, \omega) = \frac{2\pi ck}{\omega} OPD(x_1, y_1, \omega)$, where we evaluate the aberrations for every pulse constituent frequency, hence, it will be referred as the complete-aberration case.

5.2.1 Spatial and temporal intensity distributions for a 20 [fs] pulse

We generate spatial and temporal intensity distributions with Equations (5.15), (5.16), (5.23) and (5.24) for several positions around their corresponding *back focal length* (BFL) for a 20 [fs] pulse with a carrier wavelength $\lambda_0 = 810$ [nm]. The plots are presented in Figures 5.5, 5.6 and 5.7 for the concave spherical mirror, the achromatic doublet and the double-convex lens, respectively. We define the quantity $\Delta z = 0$ as the system BFL, for $\Delta z < 0$ we will be closer to the exit pupil of the system and if $\Delta z > 0$, we will be farther than the system's focal point.

In Figure 5.5, the spatial intensity distribution obtained by evaluating $I(x_2, 0)$ is different from the intensity distribution obtained by $I_{KE}(x_2)$. This demonstrates that variations in the quantities measured from these two intensity distributions are to be expected. When considering aberrations we find that the maximum value of the spatial intensity distribution is shifted from the BFL and is located closer to the mirror, while presenting a larger depth-of-focus. In addition to this the spatial intensity distributions for the carrier frequency and the complete-aberration cases are similar due to the fact that the phase due aberrations in a concave mirror is the same for all frequencies since there is no refraction during the raytracing. For the temporal intensity distribution under the aberration-free case we find that there is no symmetry around the time axis t , while having its maximum in the BFL region of the mirror. When considering aberrations, the maximum point of the temporal intensity distribution shifts closer to the mirror and presents a 'smear' in the region farther to the mirror. This maximum shift and smearing causes that the intensity autocorrelation $A^{(2)}(\tau)$ distribution to deviate from the aberration-free case.

For the achromatic doublet normalized plots, shown in Figure 5.6, we find that the spatial intensity distributions from $I(x_2, 0)$ are different from the ones recovered from the knife-edge test $I_{KE}(x_2)$ as seen in Figure 5.5. We also appreciate that the intensity maxima are not located in the focal point, slightly shifted towards the achromatic doublet and that there is a minor increase of the depth-of-focus like the one seen for the concave mirror, effect we attribute to the spherical aberration correction from the doublet. We show that there is no symmetry on the temporal intensity distribution around the time axis t in the aberration-free case while having its maximum in the BFL of the system; for the carrier frequency and complete-aberration cases, however, we find the maximum shifted beyond the doublet's focal point, and the smearing is found in the region closest to the doublet; the smearing being more pronounced in the carrier frequency case. The intensity autocorrelation map for the carrier

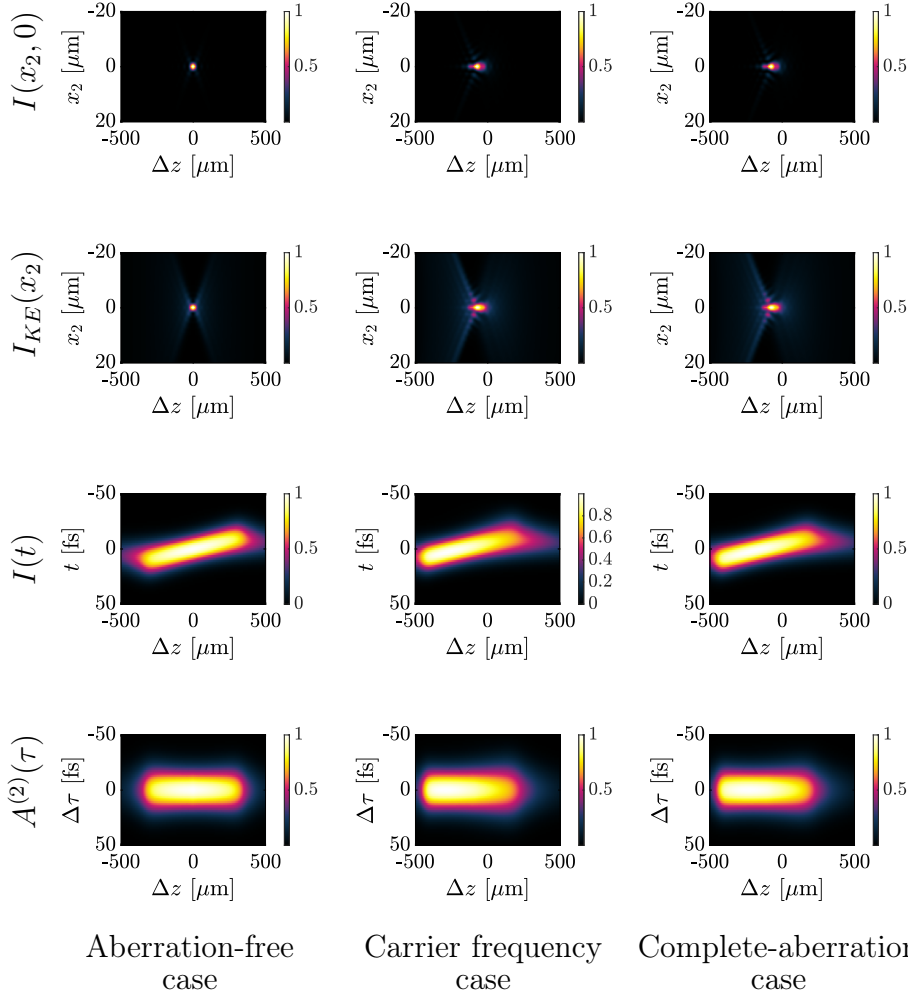


Figure 5.5: Normalized spatial and temporal intensity distributions with for several positions around the BFL of a concave mirror of $D = 12.0$ [mm] and $EFL = 30.0$ [mm] for a 20 [fs] pulse with a carrier wavelength $\lambda_0 = 810$ [nm].

frequency and the complete-aberration cases are different than the aberration-free case due the smearing effect.

For the double-convex lens, presented in Figure 5.7, we again find that the spatial intensity distribution $I(x_2, 0)$ is different from the knife-edge test $I_{KE}(x_2)$. We also note that there is a small difference between the recovered spatial intensity distributions for the carrier frequency and the complete-aberration cases. The optical aberrations found in the double-convex lens are greater than the ones found in the achromatic doublet and the concave mirror, hence, the

5.2. SIMULATIONS

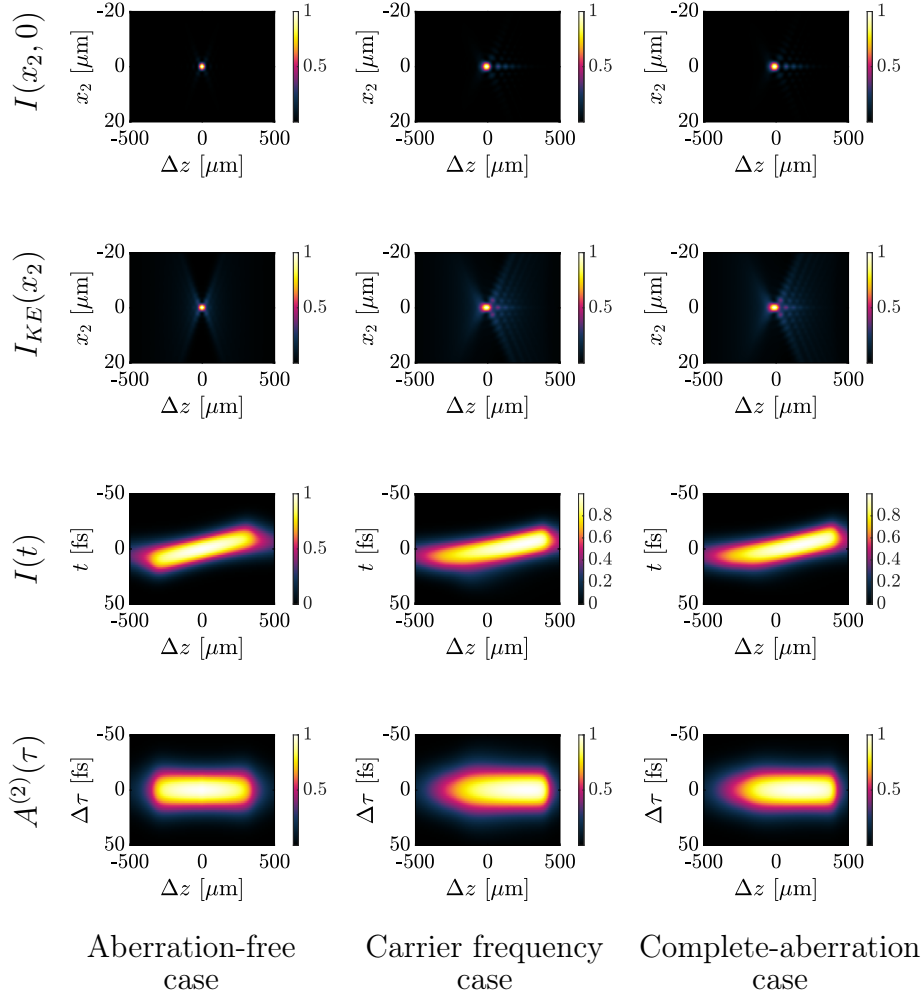


Figure 5.6: Normalized spatial and temporal intensity distributions with for several positions around the BFL of an achromatic doublet $D = 12.0$ [mm] and $EFL = 30.0$ [mm], described in Table 5.1 for a 20 [fs] pulse with a carrier wavelength $\lambda_0 = 810$ [nm].

spatial intensity distributions for the double-convex lens do not resemble the ones discussed in Figures 5.5 and 5.6. In this optical system there is a clear difference in the temporal intensity distribution for the aberration-free, carrier frequency and complete-aberration cases. When we consider aberrations we find that the maximum intensity is found closer to the lens, like in the concave mirror. However, the carrier frequency and complete-aberration cases are visually different from each other. These differences influence the intensity autocorrela-

tion distribution for this system.

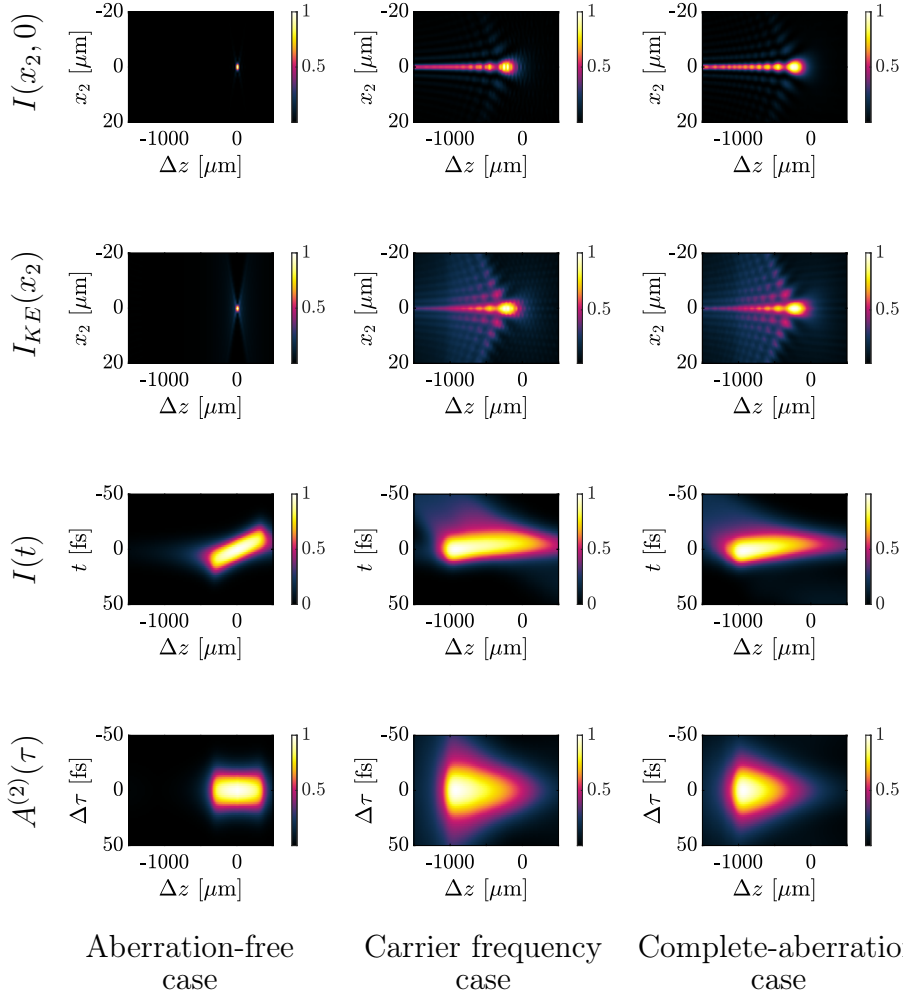


Figure 5.7: Normalized spatial and temporal intensity distributions with for several positions around the BFL of a double-convex lens with $D = 12.0$ [mm] and $EFL = 30.0$ [mm], described in Table 5.1 for a 20 [fs] pulse with a carrier wavelength $\lambda_0 = 810$ [nm].

From Figures 5.5, 5.6 and 5.7 we find that:

- The spatial intensity distributions obtained by Equation 5.15 are different from those obtained by Equation (5.23);
- the spatial intensity distributions calculated under the carrier frequency and the complete-aberration cases are similar;

5.2. SIMULATIONS

- there are differences on the temporal intensity distributions whenever we use the carrier frequency or the complete-aberration case in our calculation;
- frequency-dependent aberrations will affect the ability of the optical system to tightly focus a femtosecond pulse.

5.2.2 FWHM and standard deviation measurement comparison

We previously discussed the impact of frequency-dependent aberrations on the spatial and temporal intensity distributions and the experimental measurement simulations for a initial pulse duration of 20 [fs]. We proceed to estimate the FWHM of the distributions calculated with Equations (5.15), (5.16), (5.23) and (5.24), using the achromatic doublet, for different pulse durations τ_0 ranging from 5 [fs] to 100 [fs] around the focal point $\Delta z = 0$ under the complete-aberration case. The resulting 2D color maps are presented in Figure 5.8 We normalized the measured values against its corresponding minimum value found within the range between [-500, 500] [μm] for each pulse duration. We find that the measured FWHM from $I(x_2, 0)$ are different from the measured FWHM from $I_{KE}(x_2)$ as seen in Figures 5.8a) and 5.8b), results that can be explained by the differences found in $I(x_2, 0)$ and $I_{KE}(x_2)$ shown in Figure 5.6 for the complete-aberration case. The normalized FWHM measured from the intensity distributions in time, $I(t)$ and $A^{(2)}(\tau)$ are presented in Figures 5.8c) and 5.8d), respectively. The FWHM of $A^{(2)}(\tau)$ includes the $\sqrt{2}$ deconvolution factor. We note that the color maps of the normalized FWHM of the intensity distributions in time, $I(t)$ and $A^{(2)}(\tau)$, are different since they have a different scale in the color map. We conclude that the FWHM criterion is not a good metric since different results are obtained when measuring from the modelled theoretical intensity distributions or from the modelled experimental intensity distributions.

We measured the standard deviations in space σ_x and σ_{KE} from $I(x_2, 0)$ and $I_{KE}(x_2)$ respectively for the same input pulse durations and range along the optical axis. We normalized the standard deviation values against their corresponding minimum value found within the range for each pulse duration. The standard deviations σ_x and σ_{KE} are displayed in a 2D color map found in Figures 5.9a) and 5.9b). In a similar fashion, we measured and normalized the standard deviations σ_t and σ_{A^2} from $I(t)$ and $A^{(2)}(\tau)$, displaying them in Figures 5.9c) and 5.9d). We find that the standard deviations measured from $I(x_2, 0)$, σ_x , are the same than the standard deviations measured from $I_{KE}(x_2)$, σ_{KE} , the same result being obtained when comparing σ_t and σ_{A^2} . We conclude that the standard deviation is a better metric than the FWHM criterion to analyse the impact of frequency-dependent spherical aberrations on the focusing of femtosecond pulses. The presence of substructures or broad wings on the spatial and temporal intensity distributions may provide a unreliable FWHM measurement [1].

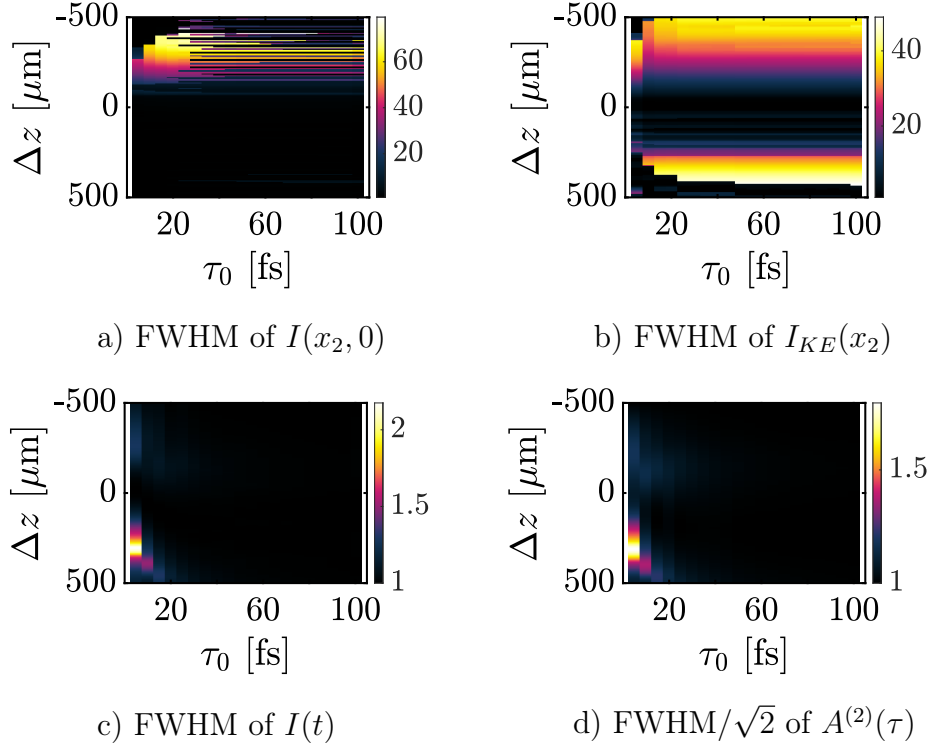


Figure 5.8: Normalized full-width at half-maximum measurements of intensity distributions for the achromatic doublet in Table 5.1 for the complete-aberration case for different input pulse durations ranging from 5 to 100 [fs] (horizontal axis) in the range between $[-500, 500]$ [μm] around the focal point $\Delta z = 0$ (vertical axis).

5.2.3 Normalized standard deviation of the spatial intensity distributions around the paraxial focal point

We present the normalized standard deviation $\sigma_x = \sigma_{KE}$ of the spatial intensity distributions obtained from Equations (5.15) and (5.23) for the different initial pulse durations τ_0 around the paraxial focal point in 2D color maps on Figure 5.10 for concave mirror, the achromatic doublet and the double-convex lens described in Table 5.1 under our three aberration cases: the aberration-free case in the first column, the carrier frequency case on the second column and the complete-aberration on the last. The darkest areas on the color maps represent the minima normalized standard deviation values, while the brightest areas represent the maxima.

On the aberration-free case, i. e. $\Theta = 0$, we find that the standard deviation map is the same for all three optical systems. This is an expected result given

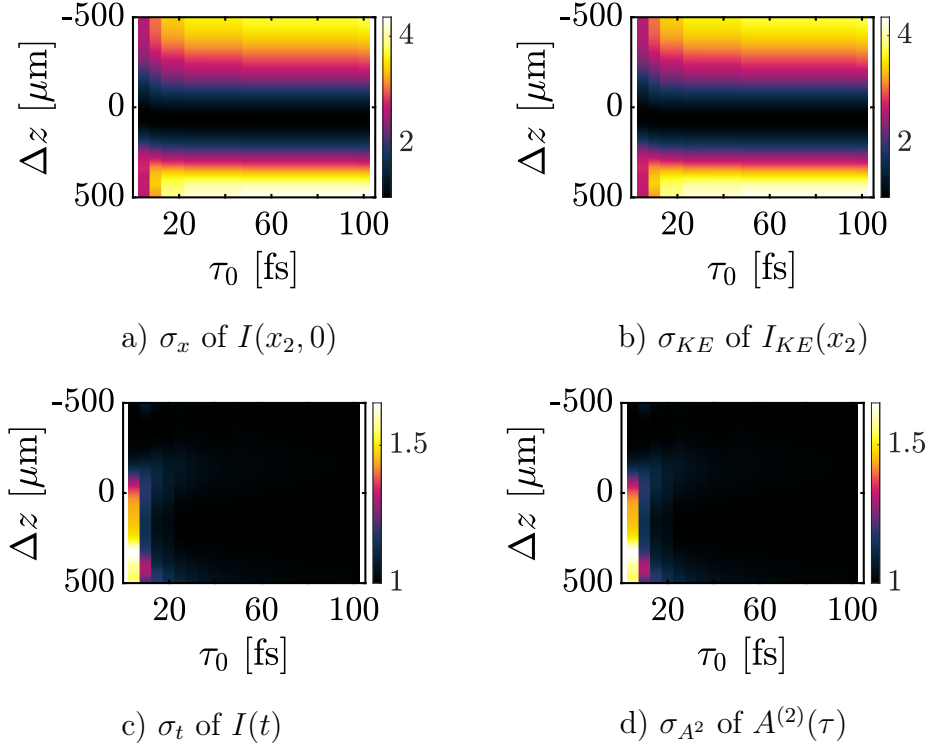


Figure 5.9: Normalized standard deviation measurements of intensity distributions for the achromatic doublet in Table 5.1 for the complete-aberration case for different input pulse durations ranging from 5 to 100 [fs] (horizontal axis) in the range between $[-500, 500]$ [μm] around the focal point $\Delta z = 0$ (vertical axis).

that they have the same diameter $D = 12.0$ [mm] and an $EFL = 30.0$ [mm]. The darkest areas on the color maps that represent the normalized standard deviation minima are located around the paraxial focal point $\Delta z = 0$ [μm] and the magnitude of the neighbouring points increases symmetrically around the paraxial focal point. We also appreciate that the depth-of-focus decreases for shorter initial pulse durations τ_0 .

The standard deviation maps for the carrier frequency and complete-aberration cases for the mirror and achromatic doublet are the same while for the double-convex lens they have slightly different peak values. The position of the minima region is located outside of the paraxial focal point and the standard deviation values increases non-symmetrically around the minima area. For the aberration-free case, the variation of the normalized standard deviation in space σ_x is larger than the normalized σ_x for the frequency carrier and complete-aberration cases, in particular for the double-convex lens which has the largest spherical aberration.

tion. The value of the largest normalized σ_x value for the double-convex lens in the complete-aberration case is 1.6 while the σ_x on the aberration-free case is over 10. The physical meaning of the reduction of the magnitude of normalized σ_x along the optical axis for the complete-aberration case is an increase in the focal depth.

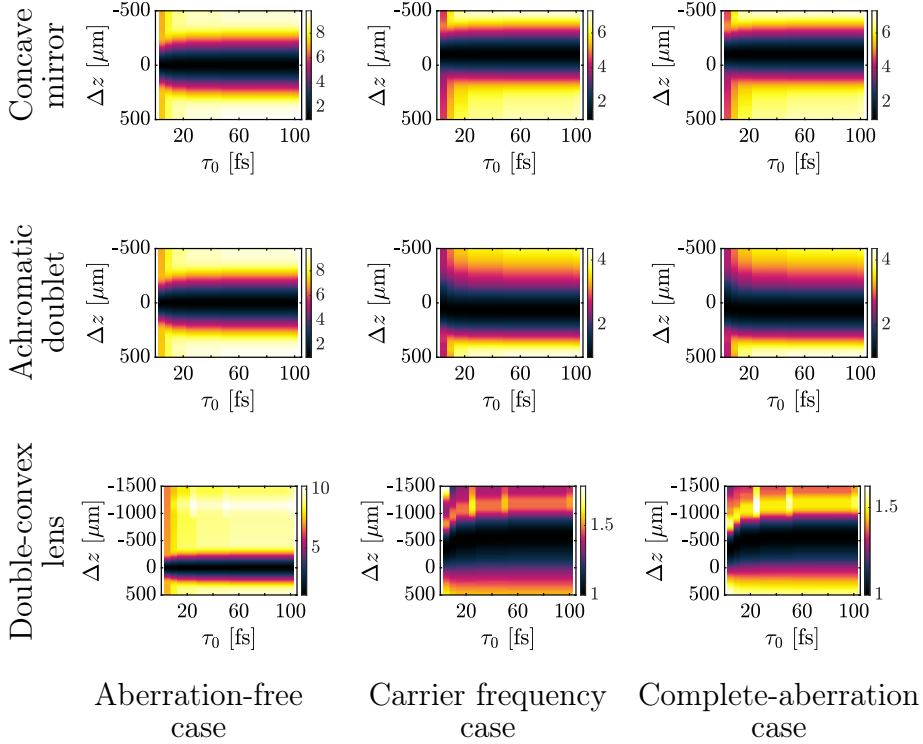


Figure 5.10: Normalized standard deviation $\sigma_x = \sigma_{KE}$ of the spatial intensity distributions obtained from Equations (5.15) and (5.23) for $\tau_0 = [5, 100]$ [fs] around the paraxial focal point for the concave mirror, the achromatic doublet and the double-convex lens described in Table 5.1 for $\Theta(x_1, y_1, \omega) = 0$, $\Theta(x_1, y_1, \omega) = 2\pi ck_0/\omega_0 OPD(x_1, y_1, \omega_0)$ and $\Theta(x_1, y_1, \omega) = 2\pi ck/\omega OPD(x_1, y_1, \omega)$.

5.2.4 Normalized standard deviation of the temporal intensity distributions around the paraxial focal point

Like we showed in Figure 5.10, we present the normalized standard deviation $\sigma_t = \sigma_{A^2}$ of the spatial intensity distributions obtained from Equations (5.16) and (5.24) for the different initial pulse durations τ_0 around the paraxial focal point in 2D color maps on Figure 5.11 for concave mirror, the achromatic doublet

and the double-convex lens described in Table 5.1 for our three aberration cases. The darkest areas, as in Figure 5.10, represent the minima normalized standard deviation values, while the brightest areas represent the maxima.

On the aberration-free case, i. e. $\Theta = 0$, we find that the time standard deviation map is the same for all three optical systems. The darkest areas on the color maps that represent the normalized standard deviation minima are located around the paraxial focal point $\Delta z = 0$ [μm] and the magnitude of the neighbouring points increases symmetrically around the paraxial focal point. We notice that in the $[-500, 500]$ [μm] range we find that there is a lower increment in the normalized standard deviation value for all initial pulse duration τ_0 , surpassing $\sigma_t = 1.3$ for $\tau_0 = 5$ [fs]. When studying a broader range, e. g.: $[-1500, 500]$ [μm] like we did for the double-convex lens, we find that the normalized σ_t value is over 8. We also appreciate that the depth-of-focus decreases for shorter initial pulse durations τ_0 .

The standard deviation maps for the carrier frequency and complete-aberration cases for the mirror and achromatic doublet present similar distributions with different upper values. We note for the mirror that the minimum values are located in a position different than the paraxial focal point, making the map non-symmetrical around the paraxial focal point, while the. For the achromatic doublet we find that there are two regions where minimum values are located: for pulse durations larger than 20 [fs] the minimum standard deviation values tend to be farther from the focal point while for shorter pulse durations the minima are located closer to the doublet. The standard deviation values measured at the double-convex lens are significantly different between the frequency carrier and the complete aberration cases, and the normalized standard deviation values are lower when compared to the aberration-free case. For the complete-aberration case, the maximum σ_t is greater than 2.2. while in the aberration-free the maximum σ_t is greater than 8.0. This reduction of magnitude of normalized σ_t along the optical axis, as it was shown with the reduction of magnitude of normalized σ_x is an increase in the focal length.

5.2.5 Normalized intensity autocorrelation magnitude distributions around the paraxial focal point

We calculated the intensity autocorrelations $A^{(2)}(\tau)$ from the temporal intensity distributions by Equation (5.24) and plotted the normalized amplitudes against their maximum value for a given input pulse duration τ_0 and the corresponding maps are shown in Figure 5.12..

Under the aberration-free case we find that the intensity autocorrelation magnitude maps have their maximum value located at the paraxial focal point and that the normalized values decrease in a symmetrical fashion. For shorter input pulse durations we appreciate that this value decreases at shorter distances; for longer pulse durations, the decrease occurs at farther distances from the paraxial focal point.

In all three components we find that the intensity autocorrelation maps for the carrier frequency and the complete-aberration cases are different from

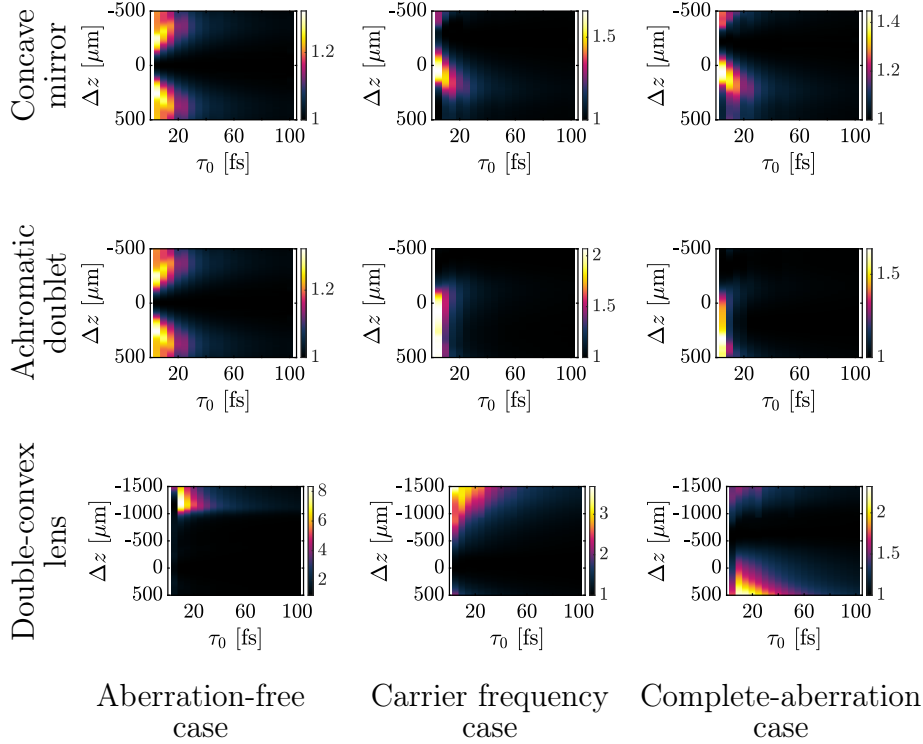


Figure 5.11: Normalized standard deviation $\sigma_x = \sigma_{A^2}$ of the temporal intensity distributions obtained from Equations (5.16) and (5.24) for $\tau_0 = [5, 100]$ [fs] around the paraxial focal point for the concave mirror, the achromatic doublet and the double-convex lens described in Table 5.1 for $\Theta(x_1, y_1, \omega) = 0$, $\Theta(x_1, y_1, \omega) = 2\pi ck_0/\omega_0 OPD(x_1, y_1, \omega_0)$ and $\Theta(x_1, y_1, \omega) = 2\pi ck/\omega OPD(x_1, y_1, \omega)$.

each other. We note that the maximum normalized intensity autocorrelation magnitude is no longer located at the paraxial focal point of the system and that its falloff is non-symmetrical. Also, there is a reduction on the area where there is a strong intensity autocorrelation magnitude, i. e. its relative value can be considered the same as the maximum for a given input pulse duration τ_0 if there is a large amount of aberrations.

5.3 Summary

We studied the theoretical basis for ultrashort pulse modelling and propagation using a combination of ray tracing and scalar diffraction theory and calculated the spatial and temporal intensity distributions of a focused collimated beam of

5.3. SUMMARY

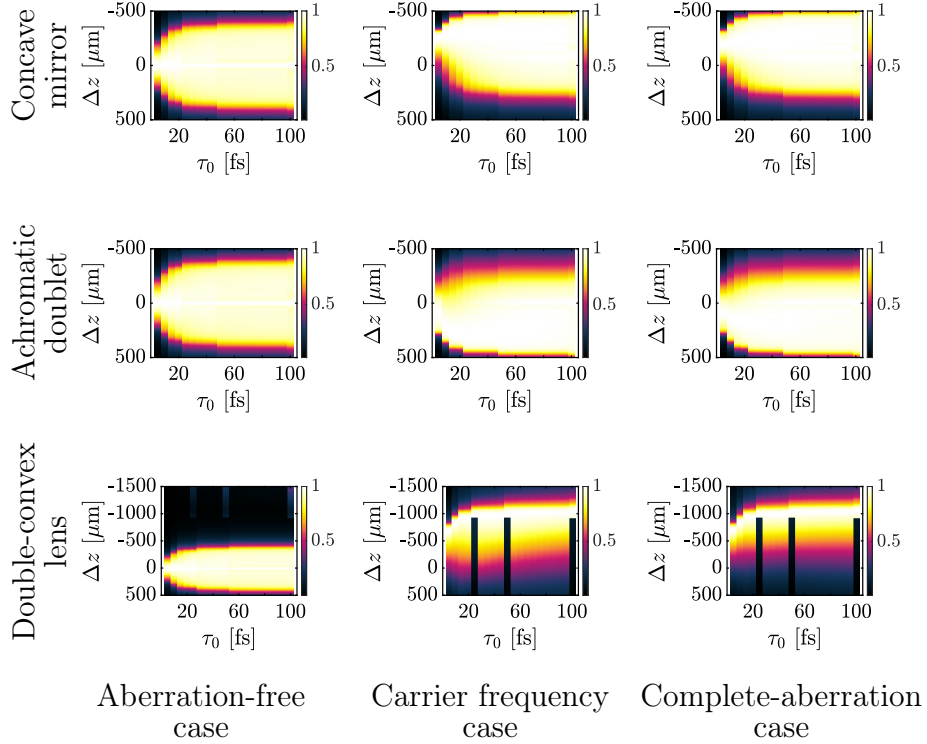


Figure 5.12: Normalized intensity autocorrelation $A^{(2)}(\tau)$ magnitudes $n \sigma_x = \sigma_{A^2}$ of the temporal intensity distributions obtained from Equations (5.16) and (5.24) for $\tau_0 = [5, 100]$ [fs] around the paraxial focal point for the concave mirror, the achromatic doublet and the double-convex lens described in Table 5.1 for $\Theta(x_1, y_1, \omega) = 0$, $\Theta(x_1, y_1, \omega) = 2\pi ck_0/\omega_0 OPD(x_1, y_1, \omega_0)$ and $\Theta(x_1, y_1, \omega) = 2\pi ck/\omega OPD(x_1, y_1, \omega)$.

ultrashort pulses, with a Gaussian spectral profile, propagating parallel to the optical axis. We calculated the spherical aberrations for different optical systems for every constituent frequency component of a given input femtosecond pulse. We neglected the dispersive effects introduced by the system, Group Velocity Dispersion and Propagation Time Difference, in order to study only the impact of the frequency-dependent spherical aberrations on the focused pulse intensity distributions.

Asides of the spatial and temporal intensity distributions obtained with Equations (5.15) and (5.16) we simulated two experimental techniques used in the laboratory to characterize the pulses in order to measure the pulse spot size and pulse duration, namely the knife-edge test as seen in Equation (5.23) and the intensity autocorrelation as seen in Equation (5.24), which are used to measure the spot size and pulse duration respectively.

To measure the width of the spatial and temporal intensity distributions from the calculated diffraction patterns and the simulated experiments we studied two measurement criteria: the FWHM and the standard deviation. We showed that the FWHM is not a good criterion since different conclusions are obtained when measuring from the direct intensity distributions and when measuring from the simulated experiments.

Figures 5.5 and 5.6 show that the spatial intensity profiles are the same when the system aberration content is calculated for the carrier frequency and the complete-aberration cases for the spherical concave mirror and the achromatic doublet; for the double-convex lens, as seen in Figure 5.7, there are slight differences between the spatial intensity profiles obtained for the carrier frequency and the complete-aberration cases. However, when comparing the temporal intensity profiles for all three components, we found that there are differences between the profiles calculated for the carrier frequency case and the complete-aberration case. This result will impact the standard deviation measurements.

We found that the magnitude and location for the minimum standard deviation in space is the same when the system aberration content is calculated for the carrier frequency and the complete-aberration cases for all three optical systems. However, we found a slight variation on the maximum standard deviation value between the carrier frequency and the complete-aberration cases when studying the double-convex lens. We conclude that the spatial intensity distribution around the focal point does not depend on the frequency-dependent spherical aberration. Nevertheless, since the frequency-dependent spherical aberration affects the temporal intensity distribution, it must be taken into account for a correct estimation of the pulse duration. Also, the location of the highest amplitude of the intensity autocorrelation changes when the frequency-dependent spherical aberration is included in the analysis due a space-time coupling.

Finally we showed that the focal depth of the system increases as the spherical aberration increases with a fixed pulse width, hence, the double-convex lens analysed in this chapter, which has the largest spherical aberration of the three systems, has a larger focal depth than the other two lenses, in agreement with published experimental results [61].

The research done in this Chapter yielded one peer-reviewed publication [30].

5.3. SUMMARY

Chapter 6

Algorithm to filter the noise in the spectral intensity of ultrashort laser pulses

Fringe-resolved auto-correlation (FRAC) technique allows to estimate pulse duration but not the spectral phase [1]. Techniques such as SPIDER [62] allow to retrieve the spectral phase and the temporal intensity profile by using spectral interferometry. Spectral interferometry, also known as Fourier-transform spectral interferometry (FTSI), consists on interfering light in the frequency domain, this allows the use of different light sources from white light, super-continuum and broad-bandwidth laser pulses. Because of this, spectral interferometry is applied in different areas ranging from ocular metrology [63], biomedical imaging [64], subsurface OCT [65], spectroscopy [66, 67], laser-plasma interactions [68], and well-known methods for measuring ultrashort laser pulses [69–72].

The effects of phase noise, spectral resolution, sampling issues and its accuracy, have been reported in the past [73–77]. These studies have considered the calibration of the spectrometer [78], the spectral resolution and the frequency sampling. Nevertheless, a careful manipulation of the experimental data and the intrinsic noise that comes with the amplitude of the electrical field in the spectral domain is required for a proper calibration. A proper measurement of spectral phase does not guarantee a reliable pulse reconstruction if the spectral intensity is not filtered correctly. The spectral intensity can also change during the manipulation of the pulses, so to measure the spectral intensity is important as a tool to improve the alignment process.

We developed an algorithm to filter the noise in the spectral intensity allowing to estimate the carrier wavelength from the recorded pulse spectrum and reconstruct the temporal intensity pulse profile from the noisy measured spectral intensity for a plane phase to test the filtering of the spectral intensity with limited user intervention.

We will describe how to model a noisy spectral intensity signal like the ones

that can be found in a laboratory setting, how to measure the carrier wavelength from a noisy spectral intensity signal and the implementation of our filtering algorithm.

6.1 Measured spectrum properties and processing

We will rely on the concepts studied in Chapter 5 to simulate bandwidth-limited, Gaussian-modulated in frequency, femtosecond pulses. On top of these, we will review some additional concepts required to implement our spectral intensity filtering algorithm.

6.1.1 Spectral intensity modelling and Signal-to-Noise Ratio

The measured spectral intensity $S_m(\lambda)$ can be defined as

$$S_m(\lambda) = S_d(\lambda) + \nu(\lambda) + b(\lambda), \quad (6.1)$$

where $S_d(\lambda)$ is the desired spectral intensity, $\nu(\lambda)$ is *additive white Gaussian noise* (AWGN) and $b(\lambda)$ is the baseline component found in the detected signal. These are typical measurement conditions at the laboratory. Equation (6.1) can be rewritten as

$$S_m(\lambda) = S_t(\lambda) + \nu(\lambda), \quad (6.2)$$

where we consider our target spectral intensity $S_t(\lambda) = S_d(\lambda) + b(\lambda)$.

To calculate the measured average signal power, we assume that [79]:

- The noise was provided by an ergodic source, which means that we can deduce its statistical properties by measuring the process for a long-enough period, having a statistical mean value of zero and a defined power spectrum.
- The noise signal $\nu(\lambda)$ is independent of $S_d(\lambda) + b(\lambda)$, in other words, there is no correlation between these quantities.

The measured spectral power is calculated by averaging $S_m(\lambda)^2 = S_t(\lambda)^2 + 2S_t(\lambda)\nu(\lambda) + \nu(\lambda)^2$, however, since the AWGN signal has a zero mean, that is, it oscillates around zero, and that we are assuming that the noise is independent from the spectral intensity, we can state that the average spectral power is [79]

$$\overline{S_m(\lambda)^2} = \overline{S_t(\lambda)^2} + \overline{\nu(\lambda)^2} \quad (6.3)$$

The *signal-to-noise ratio* (SNR) is defined as the ratio of signal power to noise power, and it is commonly expressed in decibels as shown in Equation (6.4) [79]:

$$SNR = 10 \log_{10} \left(\frac{\overline{S_t(\lambda)^2}}{\nu(\lambda)^2} \right). \quad (6.4)$$

6.1.2 Spectrum expressions in function of wavelength and frequency

The spectrometers used in experiments measure the spectral intensity as a function of wavelength, $S(\lambda)$, so it has to be transformed into the spectrum in frequency, $S(\omega)$. This wavelength-frequency transform is explained in reference [29] and it is given by Equation (6.5):

$$S_m(\lambda) = S_m(\omega) \frac{2\pi c}{\lambda^2}. \quad (6.5)$$

where c is the speed of light in vacuum and λ is the wavelength of the carrier frequency.

A theoretical spectral intensity, $S_m(\omega)$, is generated by assuming a *bandwidth limited* (BL) pulse with frequencies modulated by a Gaussian with a carrier wavelength $\lambda_0 = 810$ [nm] and a spectral phase equal to zero. For a Gaussian modulated BL pulse, the constant in Equation (5.9) is $c_B = 0.441$ [1]. The spectral intensity as a function of wavelength, $S_m(\lambda)$, is calculated by using Equation (6.5). Assuming that $S_m(\lambda)$ is now the measured spectral intensity, we will transform it to the frequency domain by using Equation (6.5).

In practice, however, the measured spectral intensity as a function of wavelength is transformed to frequency by assuming that the spectral intensity is the same, that is, by approximating Equation (6.5) to

$$S_a(\omega) = S(\lambda). \quad (6.6)$$

Tables 6.1 and 6.2 presents the comparison of using (6.5) or $S(\lambda) = S(\omega)$, while calculating the carrier wavelength via centroid from ideal pulse spectra $S(\omega)$ and $S(\lambda)$. The pulse intensity distribution was calculated by using Equations (6.11), (6.12) and (6.13) and the pulse duration at FWHM was measured.

The centroid \bar{x} of a set of n points weights w_i located at positions x_i is given by Equation (6.7):

$$\bar{x} = \frac{\sum_{i=1}^n x_i w_i}{\sum_{i=1}^n w_i} \quad (6.7)$$

From Table 6.1 we observe that the measured pulse duration estimated with both methods is the same for all cases, and the calculated carrier wavelength using the approximation $S(\lambda) = S(\omega)$ is close to the specified value except for the 5.0 [fs] pulse.

However, in Table 6.2, the recovered carrier wavelength deviates from the intended 810 [nm] value as the pulse duration is shorter. The recovered pulse duration in both cases is similar.

6.1. MEASURED SPECTRUM PROPERTIES AND PROCESSING

Initial pulse duration τ_0 [fs]	λ_0 [nm] from $S(\lambda) = S(\omega)(2\pi c)/\lambda^2$	λ_0 [nm] from $S(\lambda) = S(\omega)$	τ_p [fs] from $S(\lambda) = S(\omega)(2\pi c)/\lambda^2$	τ_p [fs] from $S(\lambda) = S(\omega)$
100.0	810.0	810.0	100.0	100.0
50.0	810.0	809.9	50.0	50.0
25.0	810.0	809.8	25.0	25.0
10.0	810.0	809.3	10.0	10.0
5.0	810.0	793.9	5.0	5.1

Table 6.1: Comparison of obtained carrier wavelength and pulse duration from $S(\omega)$ when using Equation (6.5) or $S(\lambda) = S(\omega)$ from ideal pulses with a carrier wavelength $\lambda_0 = 810$ [nm]. For shorter ideal pulses, the conversion equation does preserve the carrier wavelength.

An important difference between using the $S(\lambda) = S(\omega)$ approximation and Equation (6.5) arises when AWGN and offset are added to the spectrum as stated in $S_m(\lambda)$. In Figure 6.1a) we present the spectrum intensity in wavelength $S_t(\lambda) = S_d(\lambda) + b(\lambda)$ of a BL Gaussian-modulated in frequency 20 [fs] pulse with offset and free of noise; in Figure 6.1b), $S_m(\lambda) = S_d(\lambda) + b(\lambda) + \nu(\lambda)$ of a noisy spectrum with a SNR = 20 [dB] obtained by using MATLAB's *awgn*($S_t(\lambda)$, 20, *measured*) function; and finally in Figure 6.1c) we show the converted spectrum to the frequency domain using Equation (6.5).

We note that by applying Equation (6.5) on a noisy spectrum like the one seen in Figure 6.1b) we may amplify the noise found in the signal thanks to the conversion dependence on the wavelength. A proper wavelength range must be selected in order avoid this issue.

Initial pulse duration τ_0 [fs]	λ_0 [nm] from $S(\lambda) = S(\omega)(2\pi c)/\lambda^2$	λ_0 [nm] from $S(\lambda) = S(\omega)$	τ_p [fs] from $S(\lambda) = S(\omega)(2\pi c)/\lambda^2$	τ_p [fs] from $S(\lambda) = S(\omega)$
100.0	810.0	810.0	100.0	100.0
50.0	810.0	810.0	50.0	50.0
25.0	809.7	809.7	25.0	25.0
10.0	807.9	807.9	10.0	10.0
5.0	801.8	801.8	5.0	5.1

Table 6.2: Comparison of obtained carrier wavelength and pulse duration from $S(\lambda)$ when using Equation (6.5) or $S(\lambda) = S(\omega)$ from ideal pulses with a carrier wavelength $\lambda_0 = 810$ [nm]. For shorter ideal pulses, the conversion equation does preserve the carrier wavelength.

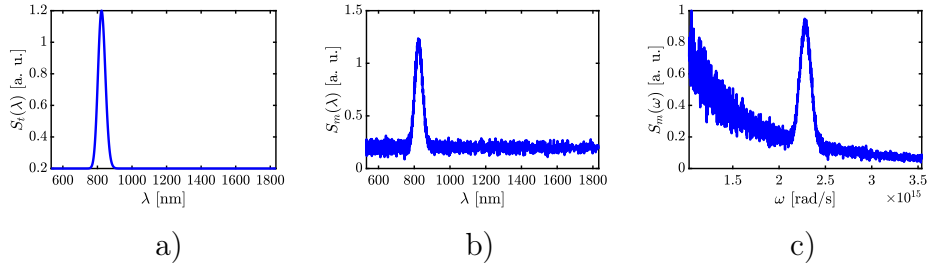


Figure 6.1: Spectral intensity of a BL Gaussian-modulated in frequency 20 [fs] pulse: a) represents $S_d(\lambda) + b(\lambda)$, b) is $S_m(\lambda) = S_d(\lambda) + b(\lambda) + \nu(\lambda)$ with a SNR = 20 [dB] and c) we show the converted spectrum to the frequency domain using Equation (6.5). Care must be taken when deciding the wavelength range for the spectrum conversion since an automatic FWHM measuring algorithm may provide an erroneous measurement.

6.2 Digital Signal Processing

In this section we will describe the core concepts for our proposed filtering algorithm.

We use a *Savitzky-Golay* filter to smooth the noise found in $S_m(\lambda)$, remove the offset $b(\lambda)$ from $S_m(\lambda)$, transform the spectrum to the frequency domain, and use a super-Gaussian window to truncate the frequencies of the spectrum.

The intensity spectrum, $S_m(\lambda)$, measured with a spectrometer always has noise and offset. Let $S_d(\omega)$ and $S_d(\lambda)$ be the intensity spectra in frequency and wavelength domains, respectively, with no offset and being noise free. $S_d(\omega)$ is generated for a pulse assuming a BL pulse with Gaussian-modulated frequencies. We transform $S_d(\omega)$ to $S_d(\lambda)$ using Equation (6.5). To model an intensity spectrum, $S_m(\lambda)$, offset and AWGN are added to $S_d(\lambda)$. This process was followed to generate Figure 6.1.

The digital signal processing techniques to filter the noise in the simulated and experimental spectral intensities are presented in the following subsections.

6.2.1 Savitzky-Golay smoothing

The *Savitzky-Golay* (SG) filter, also known as polynomial smoothing or least-squares smoothing [80,81], is a filter that takes a fixed number of points around a central abscissa, fits a polynomial that satisfies the least-squares criterion to the ordinates of the group, evaluates the obtained polynomial at the central abscissa, and substitutes the ordinate for that position. For the next abscissa, the point at one end of the group is dropped, and the neighbouring point of the other end is added to the group, taking a new central abscissa. This is repeated until all the data are processed. The SG filter preserves the sharp changes in the desired signal, at the expense of not removing as much noise as the finite

impulse response averaging filter [81].

6.2.2 Baseline removal

We implemented the automatic *iterative average* (IA) baseline removal algorithm provided by Shen [82] to remove the offset, $b(\lambda)$, from Equation (6.1). The advantage of using this particular algorithm lies in its robustness, requiring only one parameter from the user and no additional supervision. Its implementation is presented in Algorithm 1.

Algorithm 1: Automatic Iterative Averaging for baseline removal.

Result: Spectrum with baseline removed
Provide $S_m(\lambda)$, *threshold*.
Get the number of samples N from $S_m(\lambda)$.
Copy $S_m(\lambda)$ into $b'(\lambda)$.
Set *previous_s_abs* = 0.
while *True* **do**
 start_index = 1.
 end_index = $N - 2$.
 while *start_index* < $\text{floor}(N/2)$ **do**
 for *index* = [*start_index*, *end_index*] **do**
 $b'(\text{index} + 1) = \min(b'(\text{index} + 1), (b'(\text{index}) + b'(\text{index} + 2)) / 2)$.
 end
 start_index = *start_index* + 1.
 end_index = *end_index* - 1.
 end
 $s_abs = \sum_{\text{index}=1}^N |S_m(\text{index}) - b'(\text{index})|$.
 $\text{relative_error} = |\text{previous_s_abs} - s_abs| / s_abs$.
 if *relative_error* \leq *threshold* **then**
 return $b'(\lambda)$.
 else
 previous_s_abs = *s_abs*.
 $S_m = b'$.
 end
end

6.2.3 Super-Gauss as truncating window

A common digital signal processing technique to isolate the spectrum components of interest from $S_m(\omega)$ is to use a truncating window. We propose using a super-Gaussian window as described in Equation (6.8):

$$W(x, x_0, \alpha, \sigma, P) = \begin{cases} \exp \left\{ - \left[\frac{(x-x_0)^2}{2(\alpha\sigma)^2} \right]^P \right\}, & \text{if } |x - x_0| \leq \alpha/2; \\ 0, & \text{otherwise,} \end{cases} \quad (6.8)$$

where

- x is the abscissa for the window,
- x_0 is the central abscissa,
- α is the window width,
- σ is the base standard deviation for the exponential function, and
- P is the power that the content of the exponent will be raised to.

In Equation (6.8) there are three variables: α , σ and P . By setting an arbitrary window width given by $\alpha = 4$ (shown as the bottom black line in Figure 6.2) we analyze different combinations for P and σ that gives a value close to zero when evaluated at the edge of the window. In Figure 6.2 we present a comparison of different combinations for P and σ for the arbitrary window width $\alpha = 4$. It can be appreciated that by setting P equal to 6 or 8 and $\sigma = 0.3$ the amplitude reaches a value close to zero when evaluated at the edge of the window. On Table 6.3 we present the amplitude values when evaluating Equation (6.8) at the window edge with $\sigma = 0.3$, confirming the observations made in the Figure 6.2.

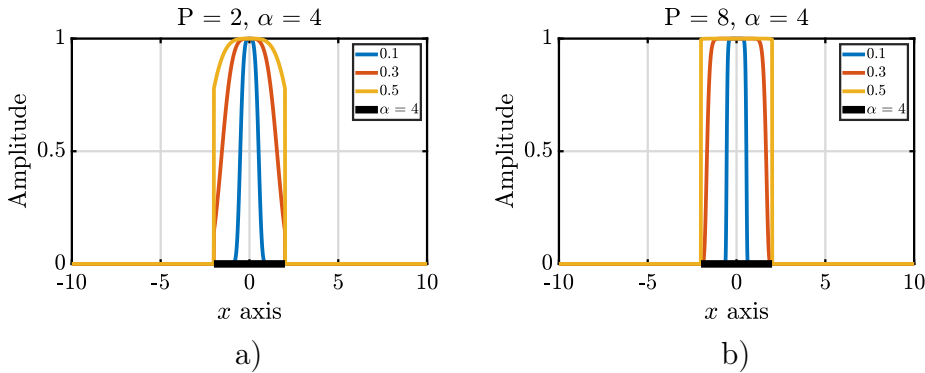


Figure 6.2: Comparison of different combinations for P and σ for a given α .

To truncate the spectrum $S(\omega)$, we multiply it by the window W :

$$S_W(\omega, \omega_0, \alpha, \sigma, P) = W(\omega, \omega_0, \alpha, \sigma, P)S(\omega) \quad (6.9)$$

P	$W(x, 0, \alpha/2, \sigma, P)$
2	0.1453
4	0.0242
6	$7.632 * 10^{-4}$
8	$9.695 * 10^{-7}$

Table 6.3: Evaluation of Equation (6.8) for different values of P for $\sigma = 0.3$ and $\alpha = 4$.

To determine a suitable window width to truncate the spectrum, we define the window width as

$$\alpha = M\Delta\omega_{FWHM}, \quad (6.10)$$

where $\Delta\omega_{FWHM}$ is the FWHM of the spectrum in frequency and M is a constant. After truncating the spectrum $S(\omega)$ we calculate the corresponding electric field in frequency $\tilde{E}(\omega)$ using Equation (6.11),

$$\tilde{E}(\omega) = \sqrt{S(\omega)}, \quad (6.11)$$

the electric field in time $e(t)$ is obtained by Fourier-transforming $\tilde{E}(\omega)$ as seen in Equation (6.12),

$$e(t) = \mathcal{F}^{-1}\{\tilde{E}(\omega - \omega_0)\}, \quad (6.12)$$

and the time intensity distribution $I(t)$ is calculated with Equation (6.13),

$$I(t) = |e(t)|^2, \quad (6.13)$$

from which the pulse duration τ_p is estimated.

We developed the Algorithm 2 to search the optimal M given σ , P , an initial value for M , step size μ , and an acceptable minimum error E_{min} as a stop condition, by estimating τ_p from the truncated spectrum $S_W(\omega)$ with Equation (5.9), and by measuring τ_p from $I(t)$ using Equations (6.11), (6.12), and (6.13).

Calculating the relative percentage error

$$E = \frac{\tau_{pI(t)} - \tau_{pS(\omega)}}{\tau_{pS(\omega)}} * 100[\%] \quad (6.14)$$

provides our stop criterion for the iterative search algorithm.

6.3 Proposed processing algorithm and testing

A combination of digital signal processing methods is required to successfully filter the spectrum $S_m(\omega)$ in a wide range of noise conditions. We propose an algorithm that first smooths $S_m(\omega)$ using the Savitzky-Golay filter, then removes the baseline using the IA baseline removal algorithm and searches for

Algorithm 2: Search for optimal window width parameter M .

Result: Window width parameter M to generate spectrum $S_W(\omega)$
that $\tau_{p_{S_m(\omega)}} \approx \tau_{p_{I(t)}}$.
Provide $S_m(\omega)$, σ , P , $M_{initial}$, μ , E_{min} , max_steps .
Measure ω_0 , $\Delta\omega_P$ from $S(\omega)$, calculate $\tau_{p_{S(\omega)}}$.
 $M = M_{initial}$.
 $step = 1$.
while $step \leq max_steps$ **do**
 Generate window $W(\omega, \omega_0, M\Delta\omega_{FWHM}, \sigma, P)$ with Equation (6.8).
 $S_W(\omega) = WS_m(\omega)$
 Calculate $I(t)$ and measure $\tau_{p_{I(t)}}$.
 Calculate relative percentual error E .
 if $|E| \leq E_{min}$ **then**
 | **return** M .
 else
 | **if** $E < 0$ **then**
 | $M = M - \mu$.
 | **else**
 | $M = M + \mu$.
 | **end**
 end
 $step = step + 1$.
end
return Could not find M that satisfies desired parameters.

an optimal window with Algorithm 2. The complete process is described by Algorithm 3.

We tested Algorithm 3 using several noisy, Gaussian-modulated in frequency pulses with offset, and comparing the results with those obtained by not filtering the spectra and by Algorithm 2. The offset in all presented cases was removed by Shen's IA algorithm. The carrier wavelength used was $\lambda_0 = 825$ [nm] with 2048 points in the frequency and wavelength vectors.

We performed the filtering by a Savitzky-Golay filter of frame length of 101 points and a order 2 polynomial with the optimal super-Gauss window search algorithm using an initial window parameter $M_{initial} = 4$, $\mu = 0.0005$, $E_{min} = 0.1$ [%] and $max_steps = 100000$, for $S(\lambda) = S(\omega)(2\pi c)/\lambda^2$ and $S(\lambda) = S(\omega)$. The carrier wavelength λ_0 was calculated from the centroid of $S(\omega)$ after filtering. We limited the wavelengths that compose the pulse from 2325 to 365 [nm], which is the transmission range for optical glass.

On Table 6.4 we generated 20 noisy spectra for a 100 [fs] pulse with offset and a SNR equal to infinity, i. e., free of noise, 30, 20 and 15 [dB], measuring the average carrier wavelength λ_0 , the recovered pulse duration from removing the offset and applying the optimal truncation window only τ_{TW} and the recovered pulse duration obtained from following Algorithm 3. We notice that for high

Algorithm 3: Proposed spectral filtering algorithm.

Result: Spectrum $S_p(\omega)$ that $\tau_{p_{SG,nobaseline}(\omega)} \approx \tau_{p_{I(t)}}$.

Provide $S_m(\lambda)$, *baseline_threshold*, *frame_length*, *poly_order*, σ , P , M_{init} , μ , E_{min} , *max_steps*.

Calculate $S_{SG}(\lambda)$ using a Savitzky-Golay filter of *frame_length* points and order *poly_order*.

Calculate $S_{SG,nobaseline}(\lambda)$ by removing the baseline with the IA algorithm using *baseline_threshold* as stop parameter.

Convert $S_{SG,nobaseline}(\lambda)$ to $S_{SG,nobaseline}(\omega)$ with Equation (5.10).

Measure ω_0 , $\Delta\omega_{FWHM}$ from $S_{SG,nobaseline}(\omega)$, calculate

$$\tau_{p_{SG,nobaseline}(\omega)}$$

$$M = M_{initial}.$$

step = 1.

while *step* ≤ *max_steps* **do**

 Generate window $W(\omega, \omega_0, M\Delta\omega_{FWHM}, \sigma, P)$ with Equation (6.8).

$$S_p(\omega) = WS_{SG,nobaseline}(\omega)$$

 Calculate $I(t)$ and measure its $\tau_{p_{I(t)}}$.

 Calculate relative percentage error E .

if $|E| \leq E_{min}$ **then**

 | **return** $S_p(\omega)$.

else

if $E < 0$ **then**

 | $M = M - \mu$

else

 | $M = M + \mu$

end

end

step = *step* + 1

end

return Could not get spectrum $S_p(\omega)$ that satisfies desired parameters.

SNR our proposed algorithm yields a similar result than just using a truncating window after removing the baseline component. However, for lower SNR, i.e., larger amount of noise, we find that our proposed algorithm provides a better measurement of the pulse duration.

We tested our algorithm for different initial pulse durations τ_P with a SNR = 20 [dB] obtaining the average results for 20 noisy spectra, which are shown in Table 6.5. There is a considerable error when not using the SG filter to smooth the input spectrum $S_m(\lambda)$ for the 20, 10 and 5 [fs] pulses. This discrepancy is due that the baseline removal algorithm fails to remove the offset when the signal has a large amount of noise.

We plotted the noisy spectrum $S_m(\lambda)$, the temporal intensity distribution for when we use the truncating window and the one for the complete algorithm in Figures 6.3a), 6.3b) and 6.3c), respectively.

SNR [dB]	λ_0 [nm]	τ_{TW} [fs]	τ_C [fs]	Error $\frac{ \tau_p - \tau_C * 100}{\tau_p}$ [%]
∞	825.0	100.2	101.9	1.9
30	825.3	98.9	98.2	1.8
20	825.7	92.2	97.9	2.1
15	826.4	85.6	97.5	2.5

Table 6.4: Average measurement results for 20 noisy 100 [fs] pulses spectra degraded with different SNR. τ_{TW} is the FWHM pulse duration measured from $I(t)$ obtained from removing the offset and applying a truncating window. τ_C is the FWHM pulse duration measured from $I(t)$ obtained from filtering the spectrum with Algorithm 3. This analysis considers that our bandwidth is comprised from 365 to 2325 [nm].

τ_P [fs]	λ_0 [nm]	τ_{TW} [fs]	τ_C [fs]	Error $\frac{ \tau_p - \tau_C * 100}{\tau_p}$ [%]
100	825.7	96.1	97.9	2.1
50	827.8	46.9	49.0	2.1
20	854.9	2.5	19.6	1.9
10	842.6	1.7	9.8	2.0
5	834.4	1.6	4.9	1.7

Table 6.5: Average measurement results for 20 noisy pulses with offset and a SNR = 20 [dB]. The initial pulse durations τ_P are 100, 50, 20, 10 and 5 [fs]. τ_{TW} is the FWHM pulse duration measured from $I(t)$ obtained from removing the offset and applying a truncating window. τ_C is the FWHM pulse duration measured from $I(t)$ obtained from filtering the spectrum with Algorithm 3. This analysis considers that our bandwidth is comprised from 365 to 2325 [nm].

6.4. SUMMARY

τ_P [fs]	λ_0 [nm]	τ_{TW} [fs]	τ_C [fs]	Error $\frac{ \tau_P - \tau_C * 100}{\tau_P}$ [%]
100	825.7	97.1	97.7	2.3
50	828.8	48.8	48.9	2.2
20	827.8	19.3	19.5	2.4
10	816.3	9.8	9.8	1.7
5	816.4	4.7	5.0	0.1

Table 6.6: Average measurement results for 20 noisy pulses with offset and a SNR = 20 [dB]. The initial pulse durations τ_P are 100, 50, 20, 10 and 5 [fs]. τ_{TW} is the FWHM pulse duration measured from $I(t)$ obtained from removing the offset and applying a truncating window. τ_C is the FWHM pulse duration measured from $I(t)$ obtained from filtering the spectrum with Algorithm 3. This analysis considers that our bandwidth is comprised from 365 to 1300 [nm].

On Table 6.6 we performed a similar analysis like the one we did for Table 6.5, however, we decided to restrict the bandwidth to [365, 1300] [nm]. We found that by limiting the bandwidth the performance of removing the offset and using a truncating window improves greatly for shorter pulses. Nevertheless, by smoothing the input spectra $S_m(\lambda)$ we achieve better results overall. We present the plots for the noisy spectra $S_m(\lambda)$ and the corresponding $I(t)$ for using the truncating window and complete algorithms on Figures 6.4a), 6.4b) and 6.4c).

6.4 Summary

A spectrum filtering algorithm comprising an offset removal, a SG filter, and a truncating super-Gaussian window has been developed to process the noisy spectral intensity of ultrashort pulses measured by a spectrometer.

By assuming that the spectral phase is known, we analyse the effect that noise in the measured intensity spectrum has on the reconstructed pulse intensity distribution, and on the estimation of the carrier wavelength and pulse duration. The algorithm was tested with simulated data with an error in the estimated pulse duration below 2.5% for pulses between 5 [fs] and 100 [fs] at $\lambda_0 = 825$ [nm] and a SNR between 30 [dB] and 15 [dB]

We have proved that the use of the SG filter to smooth the noise in the measured spectral intensity $S_m(\lambda)$ allows for a correct measurement of the carrier wavelength after the offset removal, and for the selection of a proper truncating window.

This algorithm was published in a peer-reviewed journal [31].

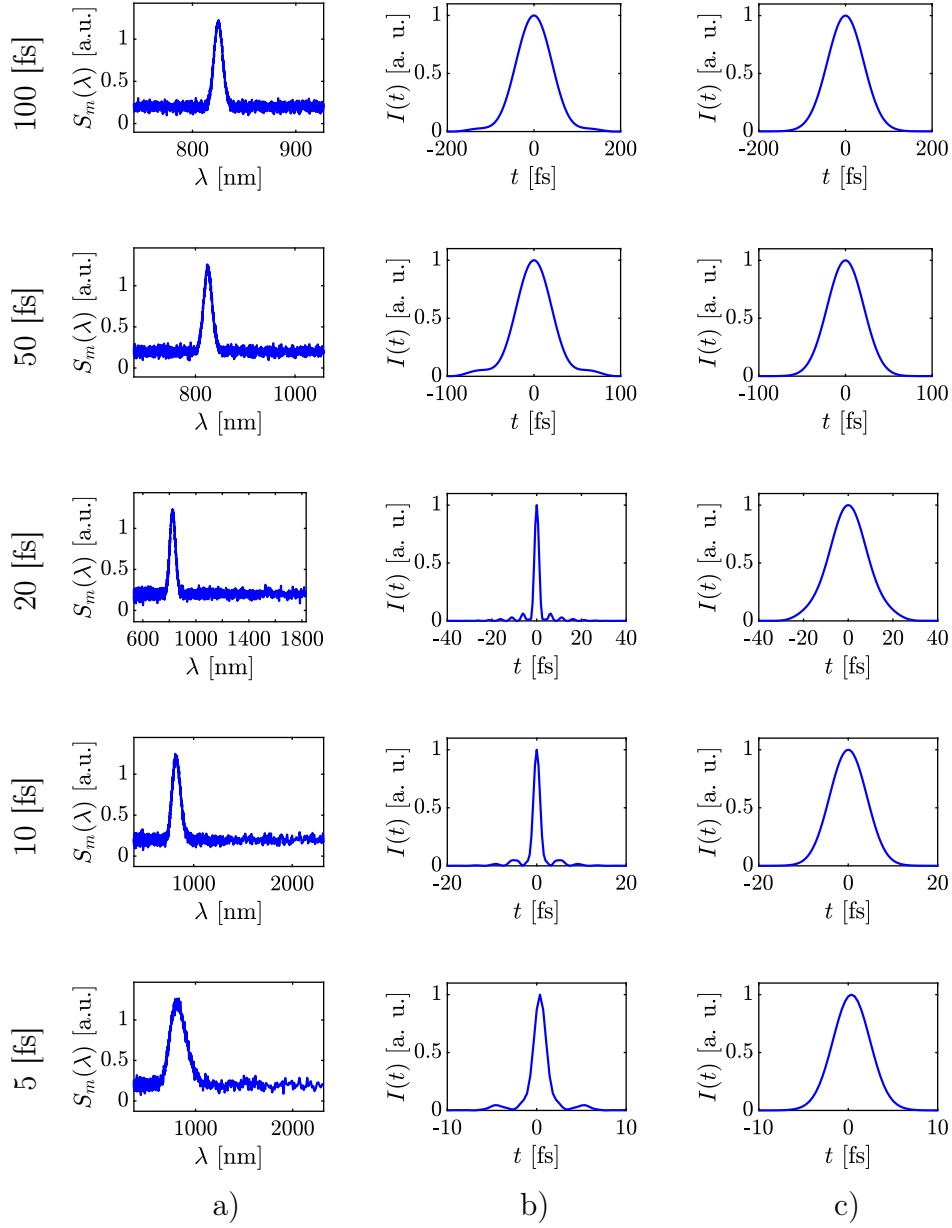


Figure 6.3: Spectra with offset and SNR = 20 [dB] and the recovered $I(t)$ for the discussed filtering techniques after the offset removal. Initial pulse durations are 100, 50, 20, 10 and 5 [fs]. Column a) shows the noisy spectra $S_m(\lambda)$; column b), the recovered $I(t)$ after removing the offset and applying a truncating window; column c), the recovered $I(t)$ after applying Algorithm 3. The spectral bandwidth is comprised from 365 to 2325 [nm].

6.4. SUMMARY

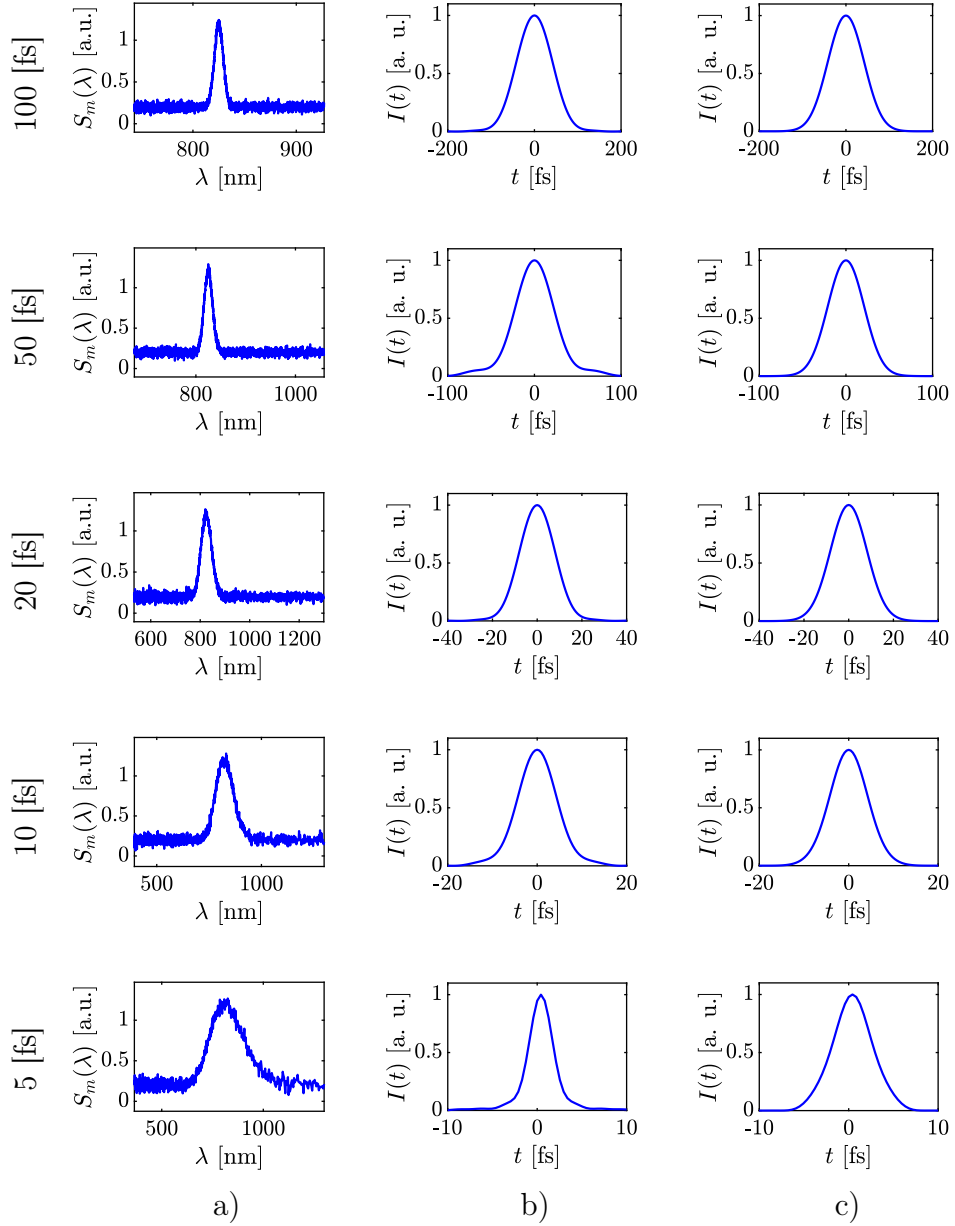


Figure 6.4: Spectra with offset and SNR = 20 [dB] and the recovered $I(t)$ for the different filtering techniques, while restricting the spectral bandwidth to [365, 1300] [nm]. Initial pulse durations are 100, 50, 20, 10 and 5 [fs]. Column a) shows the noisy spectra $S_m(\lambda)$; column b), the recovered $I(t)$ after removing the offset and applying a truncating window; column c), the recovered $I(t)$ after applying Algorithm 3.

Chapter 7

Conclusions

In this work we modelled wavefront aberrations, study their impact on the focusing of femtosecond laser pulses, and performed wavefront measurements that will assist in the fabrication of optical components at the Institute of Applied Sciences and Technology of UNAM.

On Chapter 1 we studied the fundamentals of finite raytracing: how to describe light and optical surfaces in terms of analytic geometry, the reference system used and the equations for translation and refraction or reflection.

We discussed the *Optical Path Difference* concept on Chapter 2, and how it can help us determine, for an optical system, how the emerging wavefront deviates from a ideal spherical wavefront. We presented the equations required for the OPD calculation and developed a simulator whose performance was validated against a professional optical design software.

On Chapter 3 we studied the Zernike polynomials, which are used in the optical industry to assess the aberrations of a given optical system. We explain how to fit an OPD surface to a Zernike polynomial expansion using a linear least-squares fit and compared our results against a professional optical design software.

We applied this knowledge to implement an interferometric wavefront measurement technique based on *Phase Shifting Interferometry*. We simulated interferograms using a OPD surface generated by the Zernike polynomials previously discussed and tested the least-squares and the SSPCA algorithms. We also studied their performance with experimental interferograms. We conclude that the SSPCA algorithm is best suited for experimental measurements given its ability to provide repeatable results for the current experimental setup.

On Chapter 5 we studied the theoretical basis for ultrashort pulse modelling and propagation using a combination of ray tracing and scalar diffraction theory and calculated the spatial and temporal intensity distributions of a focused collimated beam of ultrashort pulses, with a Gaussian spectral profile, propagating parallel to the optical axis. We calculated the spherical aberrations for different optical systems for every constituent frequency component of a sequence of pulses $\tau_0 = [5, 10, 15, \dots, 95, 100]$ [fs]. We neglected the dispersive effects

introduced by the system, Group Velocity Dispersion and Propagation Time Difference, in order to study only the impact of the frequency-dependent spherical aberrations on the focused pulse intensity distributions. We calculated the spatial and temporal intensity distributions and simulated experimental techniques used in the laboratory to characterize pulse properties like spot size and pulse duration. We studied two measurement criteria: the FWHM and standard deviation, finding the standard deviation method to be a superior metric since it yields similar conclusions when performing the measurement directly from the intensity distributions and the simulated experiments as well. The standard deviation is used as our metric of choice for this work. We showed that, for well corrected systems, the spatial intensity profiles are the same when the system aberration content is calculated for the carrier frequency and the complete-aberration cases; and for the time intensity profiles there are differences between disregarding the pulse bandwidth or not. We found that the magnitude and location for the minimum standard deviation in space is the same when the system aberration content is calculated for the carrier frequency and the complete-aberration cases for all three optical systems, while it is different when evaluating the standard deviation in the time intensity distributions. The spatial intensity distribution around the focal point does not depend on the frequency-dependent spherical aberration, although the whole aberration content must be considered since it affects the resulting temporal intensity distribution. This impacts the location of the highest amplitude of the intensity autocorrelation changes when the frequency-dependent spherical aberration is included in the analysis due a space-time coupling. We showed that the focal depth of the system increases as the spherical aberration increases with a fixed pulse width, hence, the double-convex lens analysed in this chapter, which has the largest spherical aberration of the three systems, has a larger focal depth than the other two lenses, in agreement with published experimental results.

On Chapter 6 we present an spectrum filtering algorithm comprised of an offset removal algorithm, a SG filter, and a truncating super-Gaussian window; developed to process the noisy spectral intensity of ultrashort pulses measured by a spectrometer in a reliable fashion. By assuming that the spectral phase is known, we analysed the effect that noise in the measured intensity spectrum has on the reconstructed pulse intensity distribution, and on the estimation of the carrier wavelength and pulse duration. The algorithm was tested with simulated data with an error in the estimated pulse duration below 2.5% for pulses between 5 [fs] and 100 [fs] at $\lambda_0 = 825$ [nm] and a SNR between 30 [dB] and 15 [dB]. We have proved that the use of the SG filter to smooth large noise in the measured spectral intensity $S_m(\lambda)$ improves the measurement of the carrier wavelength after the offset removal, and allows for the selection of a proper truncating window.

The research presented in this thesis was published in two peer-reviewed publications [30, 31] and the collaboration in a third peer-reviewed publication [83] where the spectrum filtering algorithm was implemented on another algorithm for spectral interferometry filtering.

Bibliography

- [1] Jean-Claude Diels. *Ultrashort Laser Phenomena*. Academic Press, 2 edition, 2006.
- [2] E. Ramsay, N. Pleyne, D. Xiao, R. J. Warburton, and D. T. Reid. Two-photon optical-beam-induced current solid-immersion imaging of a silicon flip chip with a resolution of 325 nm. *Opt. Lett.*, 30(1):26–28, Jan 2005.
- [3] M. Rutkauskas, D. T. Reid, J. Garduño-Mejía, and M. Rosete-Aguilar. Time-domain measurements reveal spatial aberrations in a sub-surface two-photon microscope. *Appl. Opt.*, 56(17):5047–5053, Jun 2017.
- [4] Chi Yan and Jean Claude Diels. Imaging with femtosecond pulses. *Appl. Opt.*, 31(32):6869–6873, Nov 1992.
- [5] Peng Wang, Jia Qi, Zhengming Liu, Yang Liao, Wei Chu, and Ya Cheng. Fabrication of polarization-independent waveguides deeply buried in lithium niobate crystal using aberration-corrected femtosecond laser direct writing. *Scientific Reports*, 7(1):41211, 2017.
- [6] Zoltan Z. Nagy and Colm McAlinden. Femtosecond laser cataract surgery. *Eye Vis (Lond)*, 2(1):11, 2015.
- [7] H.E. Kondakci and A.F. Abouraddy. Diffraction-free space-time light sheets. *Nature Photon*, 11:733–740, Nov 2017.
- [8] H.E. Kondakci and A.F. Abouraddy. Optical space-time wave packets having arbitrary group velocities in free space. *Nat Commun*, 10:929–936, 2019.
- [9] A. Sainte-Marie, O. Gobert, and F. Quéré. Controlling the velocity of ultrashort light pulses in vacuum through spatio-temporal couplings. *Optica*, 4(10):1298–1304, Oct 2017.
- [10] Z. Bor. Distortion of femtosecond laser pulse in lenses and lens systems. *J. Mod. Opt.*, 35(12):1907–1918, Dec 1988.
- [11] Z. Bor. Distortion of femtosecond laser pulses in lenses. *Opt. Lett.*, 14(2):119–121, Jan 1989.

BIBLIOGRAPHY

- [12] Z. Bor. Distortion of femtosecond pulses in lenses. wave optical description. *Opt. Communications*, 94(4):249–258, Nov 1992.
- [13] M. Kempe, U. Stamm, B. Wilhelmi, and W. Rudolph. Spatial and temporal transformation of femtosecond laser pulses by lenses and lens systems. *J. Opt. Soc. Am. B*, 9(7):1158–1165, Jul 1992.
- [14] M. Kempe and W. Rudolph. Femtosecond pulses in the focal region of lenses. *Physical Review A*, 48(6):4721–4729, Dec 1993.
- [15] M. Kempe and W. Rudolph. Impact of chromatic and spherical aberration on the focusing of ultrashort light pulses by lenses. *Opt. Lett.*, 18:137–139, 1993.
- [16] Ulrike Fuchs, Uwe D. Zeitner, , and Andreas Tünnermann. Ultra-short pulse propagation in complex optical systems. *Opt. Exp.*, 13:3852–3861, 2005.
- [17] Z. L. Horváth, A. P. Kovács, and Z. Bor. Distortion of ultrashort pulses caused by aberrations. *Springer Ser. Chem. Phys.*, 88:220–222, 2007.
- [18] Miguel A. González-Galicia, Martha Rosete-Aguilar, Jesus Garduño-Mejía, N.C. Bruce, and R. Ortega-Martínez. Effects of primary spherical aberration, coma, astigmatism and field curvature on the focusing of ultrashort pulses: homogeneous illumination. *J. Opt. Soc. Am. A*, 28(10):1979–1989, Oct 2011.
- [19] Miguel A. González-Galicia, Jesus Garduño-Mejía, Martha Rosete-Aguilar, N.C. Bruce, and R. Ortega-Martínez. Effects of primary spherical aberration, coma, astigmatism and field curvature on the focusing of ultrashort pulses: Gaussian illumination and experiment. *J. Opt. Soc. Am. A*, 28(10):1990–1994, Oct 2011.
- [20] Z. L. Horváth, B. Major, A. P. Kovács, and Z. Bor. Pulse front distortions caused by primary aberrations. *J. Opt. Soc. Am. B*, 30:1853–1863, 2013.
- [21] Bangshan Sun, Patrick S. Salter, and Martin J. Booth. Effects of aberrations in spatiotemporal focusing of ultrashort laser pulses. *J. Opt. Soc. Am. A*, 31(4):765–772, April 2014.
- [22] Balázs Major, Zoltán L Horváth, and Miguel A Porras. Phase and group velocity of focused, pulsed gaussian beams in the presence and absence of primary aberrations. *Journal of Optics*, 17(6):065612, may 2015.
- [23] Pamela Bowlan, Pablo Gabolde, and Rick Trebino. Directly measuring the spatio-temporal electric field of focusing ultrashort pulses. *Opt. Express*, 15(16):10219–10230, Aug 2007.

- [24] Pamela Bowlan, Ulrike Fuchs, Rick Trebino, and Uwe D. Zeitner. Measuring the spatiotemporal electric field of tightly focused ultrashort pulses with sub-micron spatial resolution. *Opt. Express*, 16(18):13663–13675, Sep 2008.
- [25] Pamela Bowlan, Pablo Gabolde, Matthew A. Coughlan, Rick Trebino, and Robert J. Levis. Measuring the spatiotemporal electric field of ultrashort pulses with high spatial and spectral resolution. *J. Opt. Soc. Am. B*, 25(6):A81–A92, Jun 2008.
- [26] Selcuk Akturk, Xun Gu, Pamela Bowlan, and Rick Trebino. Spatio-temporal couplings in ultrashort laser pulses. *Journal of Optics*, 12(9):093001, aug 2010.
- [27] Pamela Bowlan and Rick Trebino. Using phase diversity for the measurement of the complete spatiotemporal electric field of ultrashort laser pulses. *J. Opt. Soc. Am. B*, 29(2):244–248, Feb 2012.
- [28] Antonin Borot and Fabien Quéré. Spatio-spectral metrology at focus of ultrashort lasers: a phase-retrieval approach. *Opt. Express*, 26(20):26444–26461, Oct 2018.
- [29] Rick Trebino. *Frequency-Resolved Optical Grating: The Measurement of Ultrashort Laser Pulses*. Kluwer Academic Publishers, 1 edition, 2000.
- [30] José Agustín Moreno-Larios, Martha Rosete-Aguilar, Oscar G. Rodríguez-Herrera, and Jesús Garduño-Mejía. Impact of frequency-dependent spherical aberration in the focusing of ultrashort pulses. *Appl. Opt.*, 59(24):7247–7257, Aug 2020.
- [31] José Agustín Moreno-Larios, Catalina Ramírez-Guerra, Ramiro Contreras-Martínez, Martha Rosete-Aguilar, and Jesús Garduño-Mejía. Algorithm to filter the noise in the spectral intensity of ultrashort laser pulses. *Appl. Opt.*, 59(24):7233–7241, Aug 2020.
- [32] W. T. Welford. *Aberrations of optical systems*. IOP Publishing, 1 edition, 1991.
- [33] Juan Rayces. personal communication.
- [34] Juan Rayces. Parametric equations of a line or ray, 1995.
- [35] Virendra N. Mahajan. *Optical Imaging and Aberrations, part III: Wavefront Analysis*. SPIE, 1 edition, 2013.
- [36] H. H. Hopkins. *Wave Theory of Aberrations*. Oxford at the Clarendon Press, 1 edition, 1950.
- [37] H. H. Hopkins. The wave aberration associated with skey rays. *Proceedings of the Physical Society. Section B*, 65(12), 12 1952.

BIBLIOGRAPHY

- [38] Berge Tatian. A comment on the wave aberration formula of h. h. hopkins. *Optica Acta: International Journal of Optics*, 19(1), 09 1972.
- [39] Juan Rayces. Hopkins' opd and tatian's opd caboose equations. Private communication, 2009.
- [40] Juan Rayces. Eikonal: An aberration coefficient oriented lens design code.
- [41] Juan Rayces. Synthesis and analysis of wavefront errors with zernike coefficients using square grids, 1999.
- [42] Juan Rayces. Least squares computation of polynomial coefficients, 1999.
- [43] G. Golub. Numerical methods for solving linear least squares problems. *Numerische Mathematik*, 7(3), 6 1965.
- [44] Alston S. Householder. Unitary triangularization of a nonsymmetric matrix. *Journal for the Association for Computing Machinery*, 5(4), 10 1958.
- [45] Katherine Creath. Phase-measurement interferometry techniques. In Emil Wolf, editor, *Progress in Optics*, chapter 5, pages 349–393. Elsevier, 1998.
- [46] Horst Schreiber and John H. Bruning. *Phase Shifting Interferometry*, chapter 14, pages 547–666. John Wiley & Sons, Ltd, 2006.
- [47] J. E. Greivenkamp. Generalized Data Reduction For Heterodyne Interferometry. *Optical Engineering*, 23(4):350 – 352, 1984.
- [48] Mathworks. Four-quadrant inverse tangent - matlab atan2.
- [49] Deniss C. Ghiglia and Mark D. Pritt. *Two-Dimensional Phase Unwrapping: Theory, Algorithms and Software*. Wiley, 1 edition, 1998.
- [50] Shuai Yang, Weiqian Zhao, Lirong Qiu, Yun Wang, and Songmei Tian. Fast and accurate tilt-shift-immune phase-shifting algorithm based on self-adaptive selection of interferogram subblocks and principal component analysis. *Appl. Opt.*, 59(9):2906–2913, Mar 2020.
- [51] I. T. Jolliffe. *Principal Component Analysis*. Springer Series in Statistics. Springer-Verlag New York, second edition, 2002.
- [52] J. Vargas, J. Antonio Quiroga, and T. Belenguer. Phase-shifting interferometry based on principal component analysis. *Opt. Lett.*, 36(8):1326–1328, Apr 2020.
- [53] J. J. Stamnes. *Waves in focal regions. Propagation, diffraction and focusing of light, sound and water waves*. CRC Press, 1 edition, 1986.
- [54] David George Voelz. *Computational Fourier Optics: a MATLAB tutorial*. Oxford at the Clarendon Press, 1 edition, 2011.

- [55] Rüdger Paschotta. *Field Guide to Laser Pulse Generation*, volume FG14. SPIE, 1 edition, 2008.
- [56] S. Anaya-Vera, L. Garcí Martínez, M. Rosete-Aguilar, N. C. Bruce, and J. Garduño-Mejía. Temporal spreading generated by diffraction in the focusing of ultrashort light pulses with perfectly conducting spherical mirrors. *Appl. Opt.*, 30(8):1620–1626, Aug 2013.
- [57] S. Anaya-Vera, O. G. Rodríguez-Herrera, M. Rosete-Aguilar, N. C. Bruce, and J. Garduño-Mejía. Comparison of methods for the calculation of focused ultra-short pulses. *Appl. Opt.*, 56(5):1417–1421, Feb 2017.
- [58] Schott AG. *Optical Glass Data Sheets*, 1 2017.
- [59] A. E. Siegman. How to (maybe) measure laser beam quality. In *DPSS (Diode Pumped Solid State) Lasers: Applications and Issues*, page MQ1. Optical Society of America, 1998.
- [60] Rufino Díaz-Uribe, Martha Rosete-Aguilar, and Roberto Ortega-Martínez. Position sensing of a gaussian beam with a power meter and a knife edge. *Rev. Mex. Fís.*, 39(3):484–492, 1993.
- [61] P. Castro-Marín, G. Castro-Olvera, J. Garduño-Mejía, M. Rosete-Aguilar, N. C. Bruce, D. T. Reid, and O. G. Rodríguez-Herrera. Autocorrelation z-scan technique for measuring the spatial and temporal distribution of femtosecond pulses in the focal region of lenses. *Optics Express*, 25(13):14473–14482, Jun 2017.
- [62] C. Iaconis and I. A. Walmsley. Spectral phase interferometry for direct electric-field reconstruction of ultrashort optical pulses. *Optics Letters*, 23(10):792–794, 1998.
- [63] A.F. Fercher, C.K. Hitzenberger, G. Kamp, and S.Y. El-Zaiat. Measurement of intraocular distances by backscattering spectral interferometry. *Optics Communications*, (117):43–48, 1995.
- [64] A. Vakhtin, K. Peterson, W. Wood, and D. Kane. Differential spectral interferometry: an imaging technique for biomedical applications. *Optics Letters*, 28(15):1332–1334, 2003.
- [65] Andrés F. Zuluaga and Rebecca Richards-Kortum. Spatially resolved spectral interferometry for determination of subsurface structure. *Optics Letters*, 24(8):519–521, 1999.
- [66] L. Lepetit and M. Joffre. Two-dimensional nonlinear optics using fourier-transform spectral interferometry. *Optics Letters*, 21(8):564–566, 1996.
- [67] L. Lepetit, G. Cheriaux, and M. Joffre. Linear techniques of phase measurement by femtosecond spectral interferometry for applications in spectroscopy. *Journal of the Optical Society of America B*, 12(12):2467–2474, 1995.

BIBLIOGRAPHY

- [68] J.-P. Geindre, P. Audebert, S. Rebibo, and J.-C. Gauthier. Single-shot spectral interferometry with chirped pulses. *Optics Letters*, 26(20):1612–1614, 2001.
- [69] Masayuki Kakehata, Hideyuki Takada, Yohei Kobayashi, Kenji Torizuka, Yoshihiko Fujihira, Tetsuya Homma, and Hideo Takahashi. Single-shot measurement of carrier-envelope phase changes by spectral interferometry. *Optics Letters*, 26(18):1436–1438, 2001.
- [70] T. Oksenhendler, S. Coudreau, N. Forget, V. Crozatier, S. Grabielle, R. Herzog, O. Gobert, and D. Kaplan. Self-referenced spectral interferometry. *Applied Physics B*, 99(1-2):7–12, 2010.
- [71] Omel Mendoza-Yero, Benjamin Alonso, Oscar Varela, Gladys Minguez-Vega, Ínigo Juan Sola, Jesus Lancis, Vicent Climent, and Luis Roso. Spatio-temporal characterization of ultrashort pulses diffracted by circularly symmetric hard-edge apertures: theory and experiment. *Optics Express*, 18(20):20900–20911, 2010.
- [72] Jun Liu, Yongliang Jiang, Takayoshi Kobayashi, Ruxin Li, and Zhizan Xu. Self-referenced spectral interferometry based on self-diffraction effect. *Journal of the Optical Society of America B*, 29(1):29–34, 2012.
- [73] Christophe Dorrer, Nadia Belabas, Jean-Pierre Likforman, and Manuel Joffre. Spectral resolution and sampling issues in fourier-transform spectral interferometry. *Journal of the Optical Society of America B*, 17(10):1795–1802, 2000.
- [74] Michelle Rhodes, Günter Steinmeyer, and Rick Trebino. Standards for ultrashort-laser-pulse-measurement techniques and their consideration for self-referenced spectral interferometry. *Applied Optics*, 53(16):D1–D11, 2014.
- [75] M.E. Anderson, L.E.E. De Araujo, E.M. Kosik, and I.A. Walsmley. The effects of noise on ultrashort-optical-pulse measurement using spider. *Applied Physics B*, 70(1):S85–S93, 2000.
- [76] Christophe Dorrer and Ian A. Walsmley. Accuracy criterion for ultrashort pulse characterization techniques: application to spectral phase interferometry for direct electric field reconstruction. *Journal of the Optical Society of America B*, 19(5):1019–1029, 2002.
- [77] Steven Jensen and Matthew E. Anderson. Measuring ultrashort optical pulses in the presence of noise: anempirical study of the performance of spectral phase interferometry for directelectric field reconstruction. *Appl. Opt.*, 43(4):883–893, Feb 2004.
- [78] Christophe Dorrer. Influence of the calibration of the detector on spectral interferometry. *Journal of the Optical Society of America B*, 16(7):1160–1168, 1999.

- [79] A. B. Carlson, P. C Crilly, and J. C. Rutledge. *Communication Systems: an Introduction to Signals and Noise in Electrical Communication*. McGraw-Hill Higher Education, 4 edition, 2002.
- [80] Abraham. Savitzky and M. J. E. Golay. Smoothing and differentiation of data by simplified least squares procedures. *Analytical Chemistry*, 36(8):1627–1639, 1964.
- [81] Sophocles Orfanidis. *Introduction to Signal Processing*. Sophocles J. Orfanidis, 2 edition, 2010.
- [82] Xianchun Shen, Liang Xu, Shubin Ye, Rong Hu, Ling Jin, Hanyang Xu, and Wenqing Liu. Automatic baseline correction method for the open-path fourier transform infrared spectra by using simple iterative averaging. *Opt. Express*, 26(10):A609–A614, May 2018.
- [83] Ramiro Contreras-Martínez, Adrian Aupart-Acosta, Martha Rosete-Aguilar, José Agustín Moreno-Larios, and Jesús Garduño-Mejía. Wavelet-based method for spectral interferometry filtering. *Appl. Opt.*, 2020.

BIBLIOGRAPHY

Articles & certificates

Here we present the first pages of the published articles and the participation certificates for conferences, outreach activities and expositions where José Agustín Moreno Larios was involved.

Standard Deviation Positions of Intensity Profiles of a Focused Femtosecond Pulse

José Agustín Moreno-Larios^{1,*}, Martha Rosete-Aguilar¹, Oscar Gabriel Rodríguez-Herrera¹, Sergio Anaya-Vera², Jesús Garduño-Mejía¹, Neil Charles Bruce¹

¹ Instituto de Ciencias Aplicadas y Tecnología - Universidad Nacional Autónoma de México Circuito Exterior S/N, Ciudad Universitaria, Coyoacán, Ciudad de México, México. Postal Code: 04510

² Laboratorio de Pruebas Ópticas, Facultad de Ciencias Física Matemáticas, Benemérita Universidad Autónoma de Puebla (BUAP), Apdo. Postal 1152, 72000 Puebla, Puebla, México.

*agustin.moreno@icat.unam.mx

Abstract: Standard deviation of spatial and time intensity profiles from direct and experimental simulations when propagating a femtosecond pulse through an achromatic doublet were calculated. The position of minimum values in the optical axis coincides.

OCIS codes: 110.0110, 320.0320, 200.0200.

1. Introduction

We propagate a plane wavefront into an optical system and calculate the spatial and temporal intensities at a given observation plane, while simulating time-domain and spatial-domain measurements of ultrashort pulses, the former based on intensity autocorrelation and the latter by the knife-edge technique. We propose estimating the standard deviation of time and spatial intensity profiles and search for the position in the optical axis where these amounts are minimal.

2. Theory

The electric field of a pulse focused by a non-dispersive imaging system, assuming a plane wavefront with a propagation vector parallel to the optical axis is given by Equation (1) [1, 2],

$$U(x_2, y_2, z, t) = -\frac{ie^{ikz}}{\lambda z} \iint\limits_{-\infty}^{\infty} dx_1 dy_1 U_0(x_1, y_1) P(x_1, y_1) A(\Delta\omega) \times \\ \times \exp[-i\Theta(x_1, y_1, \Delta\omega)] \exp[-i\phi(x_1, y_1, \Delta\omega)] \exp\left\{-i\frac{k}{2z}[(x_2 - x_1)^2 + (y_2 - y_1)^2]\right\} \exp(-i\Delta\omega t) d(\Delta\omega). \quad (1)$$

where (x_1, y_1) are the rectangular coordinates in the exit pupil plane; (x_2, y_2) are the rectangular coordinates in the observation plane; z is the position in the optical axis; U_0 is the input electric field; $P(x_1, y_1)$ is the pupil function and it is defined as one inside the pupil radius and zero otherwise; $A(\Delta\omega)$ is the Gaussian frequency modulation of the input field; $\Theta(x_1, y_1, \Delta\omega)$ is the phase due to the optical system aberrations; $\phi(x_1, y_1, \Delta\omega)$ is the phase associated with the transformation of a plane wavefront into a converging spherical wavefront; k is the wavenumber of the pulse frequencies. It can be expressed as $k = k_0(1 + \Delta\omega/\omega_0)$ being k_0 and ω_0 the carrier wavenumber and frequency, respectively; $\Delta\omega = \omega - \omega_0$; and λ is the wavelength for each frequency that forms the pulse, $\lambda = 2\pi c/\omega$, c being the speed of light in the vacuum.

Spatial and temporal intensity profiles are defined as

$$I(t, z) \propto \int\limits_{-\infty}^{\infty} \int\limits_{-\infty}^{\infty} |U(x_2, y_2, z, t)|^2 dx_2 dy_2 \quad (2)$$

and

$$I(x_2, y_2, z) \propto \int\limits_{-\infty}^{\infty} |U(x_2, y_2, z, t)|^2 dt, \quad (3)$$

respectively.

To recreate the measuring methods that may be used at our laboratory, we implemented the knife-edge test [3] and the intensity autocorrelation [4], and estimating the squared root of their second order central moments, or standard deviation [5].



Impact of frequency-dependent spherical aberration in the focusing of ultrashort pulses

JOSÉ AGUSTÍN MORENO-LARIOS,  MARTHA ROSETE-AGUILAR, * 
OSCAR G. RODRÍGUEZ-HERRERA,  AND JESÚS GARDUÑO-MEJÍA 

Instituto de Ciencias Aplicadas y Tecnología, Universidad Nacional Autónoma de México, Circuito Exterior S/N, Cd. Universitaria, 04510, Mexico City, Mexico

*Corresponding author: martha.rosete@icat.unam.mx

Received 2 April 2020; revised 6 July 2020; accepted 7 July 2020; posted 10 July 2020 (Doc. ID 394300); published 18 August 2020

In this paper, the temporal and spatial intensity pulse distributions are calculated around the focal region of an optical system using a combination of ray tracing and a wave propagation method. We analyze how to measure the width of the intensity pulse distributions to estimate pulse duration and spot size in order to study the impact of the variation of spherical aberration with frequency in a pulse on the intensity distributions. Two experimental techniques used in the laboratory are also modeled: the knife-edge test to measure spatial distribution and the intensity autocorrelation technique to measure the temporal distribution. We use two measuring criteria, the full-width half-maximum (FWHM) and standard deviation (σ), to compare the spatial and temporal intensity distributions of the calculated diffraction patterns and those obtained from the simulated experimental techniques. We show that the FWHM is not a good criterion, since it gives different results in the measured intensity distributions in time and space when they are measured directly from the theoretical modeling and when they are measured from the modeled experimental techniques used in the laboratory. The standard deviation, however, is a consistent criterion, giving the same results for the calculated intensity distributions and the modeled experiments. © 2020 Optical Society of America

<https://doi.org/10.1364/AO.394300>


1. INTRODUCTION

The focusing of femtosecond pulses has been studied extensively theoretically and experimentally [1–13]. Techniques have been developed to measure the spatiotemporal coupling of ultrashort pulses around the focal region of optical systems [14–21]. The understanding of the spatiotemporal coupling of ultrashort pulses and its metrology is important in applications such as nonlinear microscopy [22–24], micromachining [25], medicine [26], and fundamental science [27–29]. The effect of aberrations in the spatiotemporal coupling of femtosecond pulses around the focal plane has also been studied by calculating the aberration for the carrier frequency and neglecting its variation with the frequencies of the pulse [4–6,8–11]. A tool for the simulation of ultrashort pulse propagation through an optical system based on a combination of ray tracing and wave optical propagation methods, including the variation of the aberration with pulse frequencies, was published by Fuchs, *et al.* [7]. In the simulation in Ref. [7], the dispersive effects, namely, group velocity dispersion (GVD) [4,5] and propagation time difference (PTD) [1–5], were also added to calculate the pulse front distortion in the focal region of different lenses.

It is well known that the dispersion of the lens material introduces the largest temporal spreading of the focusing pulses, which is a main concern if the shortest pulse duration should be achieved at the focus of the optical system. In the laboratory, GVD can be pre-compensated for by using a pulse compressor, and PTD (propagation time difference) can be reduced by using achromatic optics. PTD, is a delay in the arrival time of pulses propagating at different heights on the aperture of the system. PTD depends not only on the longitudinal chromatic aberration but also on the numerical aperture of the lens, and its effect on the spatial and temporal intensity distributions increases for large apertures [30,31]. In this paper, we neglect GVD and PTD; however, we consider the frequency-dependent spherical aberration, which means that the variation of spherical aberration with frequency is taken into account. In this paper, instead of analyzing the pulse front distortion as in Ref. [7], we focus our attention on how to measure the width of the temporal and spatial intensity pulse distributions to estimate pulse duration and spot size, to study only the impact of the frequency-dependent spherical aberration on the spatial and temporal intensity distributions around the focal plane. To the best of our knowledge, this is the first time that this study has been performed.



Algorithm to filter the noise in the spectral intensity of ultrashort laser pulses

JOSÉ AGUSTÍN MORENO-LARIOS,  CATALINA RAMÍREZ-GUERRA, RAMIRO CONTRERAS-MARTÍNEZ,  MARTHA ROSETE-AGUILAR,*  AND JESÚS GARDUÑO-MEJÍA 

Instituto de Ciencias Aplicadas y Tecnología, Universidad Nacional Autónoma de México, Circuito Exterior S/N, Cd. Universitaria, 04510 Mexico City, Mexico

*Corresponding author: martha.rosete@icat.unam.mx

Received 27 April 2020; revised 12 July 2020; accepted 15 July 2020; posted 16 July 2020 (Doc. ID 396247); published 17 August 2020

We have developed an algorithm to filter the noise in the spectral intensity of ultrashort laser pulses. The filtering procedure consists of smoothing the noise by using the Savitzky–Golay filter, removing the offset, and using a super-Gaussian window to truncate the frequencies of the spectrum. We have modeled bandwidth-limited ultrashort pulses with Gaussian modulated frequencies to show the estimation of the carrier wavelength, reconstruction of the intensity pulse profile, and pulse duration after applying the algorithm. Theoretical results are presented for pulse durations between 5 fs and 100 fs with a carrier wavelength of 825 nm and three different amounts of signal-to-noise ratio (SNR): 30 dB, 20 dB, and 15 dB, normally found in experiments. The algorithm is also applied to an experimental spectral intensity from a homemade Ti:sapphire laser that produces pulses of about 20 fs at 825 nm at 100 MHz. We will show that using only a low-pass Fourier filter and removing offset is not enough to recover the spectral intensity when a large SNR is present, which may be the case when the ultrashort laser beam has been manipulated to compensate for the group velocity dispersion of an external optical system. In cases like this, the use of the Savitzky–Golay filter prior to the super-Gaussian filter improves the recovery of the carrier wavelength and the spectral intensity. We will also show that the algorithm presented in this paper is suitable for experimental analysis and requires limited user intervention. © 2020 Optical Society of America

<https://doi.org/10.1364/AO.396247>

1. INTRODUCTION

The fringe-resolved autocorrelation (FRAC) technique allows the estimation of pulse duration but not the spectral phase [1]. Techniques such as spectral phase interferometry for direct electric-field reconstruction (SPIDER) [2] allow retrieval of the spectral phase and the temporal intensity profile by using spectral interferometry. Spectral interferometry, also known as Fourier transform spectral interferometry (FTSI), consists of interfering light in the frequency domain, which allows the use of different light sources such as white light, supercontinuum, and broad-bandwidth laser pulses. Because of this, spectral interferometry is applied in different areas ranging from ocular metrology [3], biomedical imaging [4], subsurface optical coherence tomography (OCT) [5], spectroscopy [6,7], laser-plasma interactions [8], and well-known methods for measuring ultrashort laser pulses [9–12]. The effects of phase noise, spectral resolution, and sampling issues and their accuracy have been reported in the past [13–17]. These studies have considered the calibration of the spectrometer [18], the spectral resolution, and the frequency sampling. Nevertheless, a careful manipulation

of the experimental data and the intrinsic noise that comes with the amplitude of the electrical field in the spectral domain is required for a proper calibration. A proper measurement of spectral phase does not guarantee a reliable pulse reconstruction if the spectral intensity is not filtered correctly. The spectral intensity can also change during the manipulation of the pulses, so to measure the spectral intensity is important as a tool to improve the alignment process. In this paper, an algorithm to filter the noise in the spectral intensity is presented allowing to estimate the carrier wavelength from the recorded pulse spectrum and reconstruct the temporal intensity pulse profile from the noisy measured spectral intensity for a plane phase to test the filtering of the spectral intensity. We have modeled ultrashort pulses with durations of 100 fs, 50 fs, 20 fs, 10 fs, and 5 fs at 825 nm using four different levels of signal-to-noise ratio (SNR) in the intensity spectrum: $\text{SNR} = \infty$ (i.e., noise free), $\text{SNR} = 30$ dB, $\text{SNR} = 20$ dB, and $\text{SNR} = 15$ dB. We will show that for the noisy intensity spectra, only removing offset and using a low-pass Fourier-filter, such as a super-Gaussian filter, is not enough to recover the temporal intensity pulse profile properly for pulses shorter than 50 fs at 825 nm and SNRs below 30 dB. However,



SPIE. STUDENT CHAPTER
UNIVERSIDAD
NACIONAL
AUTÓNOMA DE MÉXICO



The UNAM and the USAL in collaboration with the SPIE UNAM Chapter are pleased to present this

Certificate of attendance

awarded to

José Agustín Moreno Larios

for attending the



held in Universidad Nacional Autónoma de México, Ciudad Universitaria, CDMX, August 3, 2017.

Dr. Rufino Díaz Uribe
Advisor of SPIE UNAM Chapter

Ms. Itzel Reyna Morales
President of SPIE UNAM Chapter



CULTURA
SECRETARÍA DE CULTURA



B|V|O BIBLIOTECA
VASCONCELOS



La Secretaría de Cultura, a través
de la Biblioteca Vasconcelos,
otorga el presente

29
abril
2018

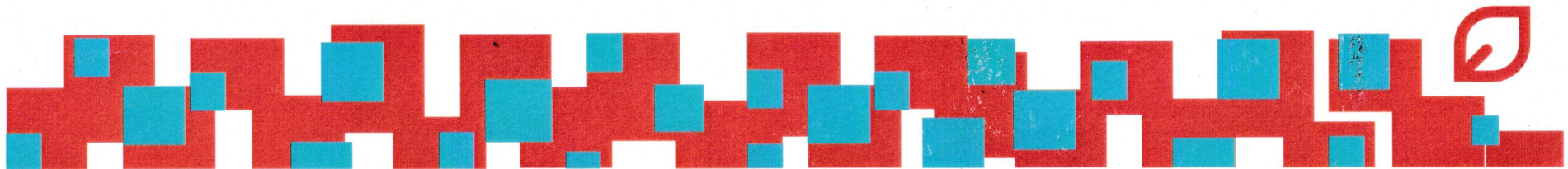
Reconocimiento a

Jose Agustín Moreno Larios

Por su participación como regalador el día 29 de abril en el
Día del Niño en la Vasconcelos:
un regalo íntimo compartido en el espacio público.



Daniel Goldin Halfon
Director de la
Biblioteca Vasconcelos





SPIE. STUDENT CHAPTER
UNIVERSIDAD NACIONAL AUTÓNOMA DE MÉXICO



El Capítulo Estudiantil SPIE Universidad Nacional Autónoma de México y el Departamento de Óptica y Microondas del ICAT otorga la presente

CONSTANCIA

a *M. en I. José Agustín Moreno Larios*

por su participación con la plática intitulada:

“Modelado de pulsos ultracortos en la región focal de dobletes acromáticos usando polinomios de Zernike”

en el Seminario “Roberto Ortega / SPIE” celebrado en el Auditorio del Instituto de Ciencias Aplicadas y Tecnología de la UNAM.

“POR MI RAZA HABLARÁ EL ESPÍRITU”
Ciudad Universitaria, CDMX, a 17 de agosto del 2018

Dr. Jesús Garduño Mejía
Coordinador del Grupo Óptica no lineal

Fís. Mitzi Ordóñez Pérez
Presidente SPIE UNAM Chapter



UNIVERSIDAD NACIONAL
AUTÓNOMA DE
MÉXICO

Universidad Nacional Autónoma de México
Dirección General de Divulgación de la Ciencia

otorgan la presente constancia a

José Agustín
Moreno Larios

por su valiosa participación en el equipo del *staff*,
en la 6ª. edición de la Fiesta de las Ciencias y las Humanidades 2018

“POR MI RAZA HABLARÁ EL ESPÍRITU”
Ciudad, Universitaria, octubre de 2018

Dr. César Augusto Domínguez Pérez Tejada
Director General de Divulgación de la Ciencia



UnAm
La Universidad
de la Nación



DGDCUNAM
Divulgación de la Ciencia



OSA
Foundation

**Siegman International
School on Lasers**

Co-founded by IPG Photonics

HOST FOR 2018:



Technical University
of Denmark

Certificate of Completion

OSA Foundation is pleased to present

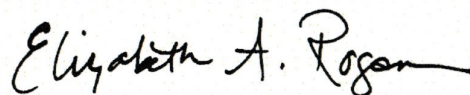
José Agustín Moreno-Larios

this certificate for successfully completing

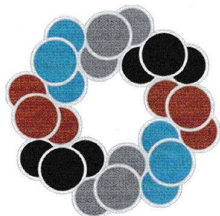
Siegman International School on Lasers

Issued 3 August 2018

Spirit of Hven Backafallsbyn, Sweden



Elizabeth A. Rogan
Chief Executive Officer



CONACYT

IBERO
PUEBLA

U
UPAEP



Tecnológico
de Monterrey



BUAP



PUEBLA
ES MI DESTINO



CONSEJO DE CIENCIA Y TECNOLOGÍA
DEL ESTADO DE PUEBLA
GOBIERNO DE PROGRESO

SPIE. STUDENT
CHAPTER
BENEMÉRITA UNIVERSIDAD
AUTÓNOMA DE PUEBLA

UDLAP

SEP
SECRETARÍA DE
EDUCACIÓN PÚBLICA



LA SOCIEDAD MEXICANA DE FÍSICA

Agradece la asistencia y participación de:

José Agustín Moreno Larios
Instituto de Ciencias Aplicadas y Tecnología, U

en el **LXI Congreso Nacional de Física**

Centro Cultural Universitario
Benemérita Universidad Autónoma de Puebla
del 7 al 12 de octubre de 2018


Dr. Darío Núñez Zúñiga
Presidente de la SMF

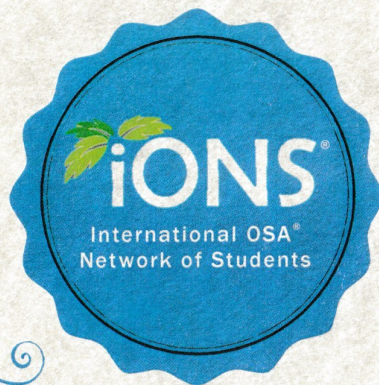
2019 COMPETITION WINNER

THIS CERTIFICATE ACKNOWLEDGES

José Agustín Moreno-Larios
UNAM Student Chapter

IN RECOGNITION OF PRESENTING PROFESSIONAL DEVELOPMENT OPPORTUNITIES FOR MEMBERS

Presented at IONS® Orlando 2019
Orlando, Florida, USA



David Guacaneme

IONS® Chapter Management Chair

OSA[®]
The Optical Society

JOSÉ AGUSTÍN MORENO LARIOS
Universidad Nacional Autónoma de México



N
2019

Escuela de Nano-Espectroscopia

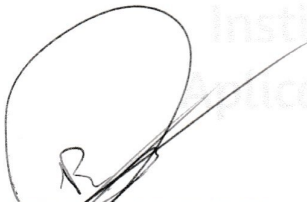
25 – 28 Noviembre 2019
CDMX, México


CONSTANCIA N°: N079

Constancia de participación

Se otorga la presente constancia a JOSÉ AGUSTÍN MORENO LARIOS por haber participado como expositor en la modalidad CARTEL en la **Escuela de Nano-Espectroscopia (ENE-2019)**. Realizado en el Instituto de Ciencias Aplicadas y Tecnología de la Universidad Nacional Autónoma de México, CDMX, México el 26 de noviembre del 2019.

Agradecemos a Ud. su participación en la Escuela.

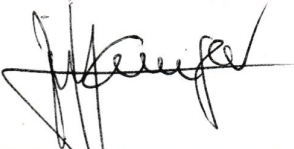

Dr. Rodolfo Zanella Specia
Director del ICAT
ICAT – UNAM


Dra. Elsi Violeta Mejía Uriarte
Responsable de la ENE 2019
ICAT – UNAM

U.N.A.M.



INSTITUTO DE CIENCIAS
APLICADAS Y TECNOLOGÍA
I.C.A.T.


Dr. José Manuel Saniger Blesa
Presidente de la ENE 2019
ICAT – UNAM

UNAM
La Universidad
de la Nación

Certificate of Attendance

José Agustín Moreno-Larios

Attended the

2019 FiO + LS Conference

15 - 19 September 2019

Washington Marriott Wardman Park

Washington, DC, USA

OSA
The Optical Society

100
Since 1916



OSA Registration Specialist



OSA Universidad Nacional
Autónoma de México
Student Chapter

CEOF
COMUNIDAD ESTUDIANTIL DE ÓPTICA Y FOTÓNICA

SPIE. STUDENT CHAPTER
UNIVERSIDAD NACIONAL AUTÓNOMA DE MÉXICO

OSA SPIE.
The Optical Society
Student Chapter
Universidad Nacional de Tucumán

STUDENT CHAPTER
INAOE

OSA
Student Chapter
UNI

STUDENT CHAPTERS
OSA SPIE - UNAM



THORLABS



Certificate of Attendance to the IONS OPUMA 2020
June 8th - 12th, 2020

Moreno Larios, José Agustín

Jonathan A. Urrutia Anguiano
Academic Committee Chair

Guillermo A. Pérez Lobato
Collaboration Chair

Daniela K. Calvo Ramos
Local Committee Chair

Dr. Karen Volke-Sepúlveda
OSA - UNAM Student
Chapter Advisor



CAPÍTULO ESTUDIANTIL CFATA UNAM DE LA SOCIEDAD MEXICANA DE MATERIALES

otorga el presente reconocimiento a

M. EN I. AGUSTÍN MORENO

por su participación con el curso

**ÓPTICA Y COMPUTACIÓN: ALGORITMOS ÚTILES
PARA TODA OCASIÓN**

Realizado del 29 de junio al 3 de julio de 2020. Con un total de 15 horas
CAPÍTULO VERANO, CURSO VIRTUAL.

DANIELA K. CALVO RAMOS

PRESIDENTA DEL CAPÍTULO
ESTUDIANTIL CFATA UNAM

The OSA Foundation

CERTIFICATE OF COMPLETION

PRESENTED TO

José Agustín Moreno-Larios

THIS CERTIFIES THAT YOU HAVE COMPLETED
THE 2020 VIRTUAL INNOVATION SCHOOL

NOW GO FORTH AND INNOVATE!

Chad Stark

CHAD STARK
OSA FOUNDATION EXECUTIVE DIRECTOR

OSA
Foundation